FABRICATION, SENSATION AND CONTROL OF FLUIDIC ELASTOMER ACTUATORS AND THEIR APPLICATION TOWARDS HAND ORTHOTICS AND PROSTHETICS

A Dissertation

Presented to the Faculty of the Graduate School

of Cornell University

In Partial Fulfillment of the Requirements for the Degree of

Doctor of Philosophy

by

Huichan Zhao

January 2017

FABRICATION, SENSATION AND CONTROL OF FLUIDIC ELASTOMER ACTUATORS AND THEIR APPLICATION TOWARDS HAND ORTHOTICS AND PROSTHETICS

Huichan Zhao, Ph. D.

Cornell University 2017

Due to their continuous and natural motion, fluidic elastomer actuators (FEAs) have shown potential in a range of robotic applications including prosthetics and orthotics. Despite their advantages and rapid developments, robots using these actuators still have several challenging issues to be addressed. First, the reliable production of low cost and complex actuators that can apply high forces is necessary, yet none of existing fabrication methods are both easy to implement and of high force output. Next, compliant or stretchable sensors that can be embedded into their bodies for sophisticated functions are required, however, many of these sensors suffer from hysteresis, fabrication complexity, chemical safety and environmental instability, and material incompatibility with soft actuators. Finally, feedback control for FEAs is necessary to achieve better performance, but most soft robots are still "open-loop". In this dissertation, I intend to help solve the above issues and drive the applications of soft robotics towards hand orthotics and prosthetics.

First, I adapt rotational casting as a new manufacturing method for soft actuators. I present a cuboid soft actuator that can generate a force of >25 N at its tip, a near ten-fold increase over similar actuators previously reported. Next, I propose a soft orthotic finger with position control enabled via embedded optical fiber. I monitor both the static and dynamic states via the optical sensor and achieve the prescribed curvatures accurately and with stability by a gain-scheduled proportional-integral-derivative controller. Then I develop the soft orthotic fingers into a low-cost, closed-loop controlled, soft orthotic glove that can be worn by a typical human hand and helpful for grasping light objects, while also providing finger position control. I achieve motion control with inexpensive, binary pneumatic switches controlled by a simple finite-state-machine. Finally, I report the first use of stretchable optical waveguides for strain sensing in a soft prosthetic hand. These optoelectronic strain sensors are easy to fabricate, chemically inert, and demonstrate low hysteresis and high precision in their output signals. I use the optoelectronically innervated prosthetic hand to conduct various active sensation experiments inspired by the capabilities of a real hand.

BIOGRAPHICAL SKETCH

Huichan Zhao was born in China on September 22nd, 1989. Her father, Yuzhong Zhao, is a civil engineer and her mother, Yuxia Tian, is a middle-school teacher teaching Chinese. She spent her childhood life in her hometown city—Zibo in Shandong province—until she was 16 years old. Then she attended her high school in Jinan, the provincial capital of Shandong.

In 2008, she went to Beijing, the capital of China, and started to pursue her bachelor's degree at Tsinghua University. In July 2012, she completed her bachelor's degree in Mechanical Engineering and a second bachelor's degree in Economics.

In August 2012, she came to the United States and started to pursue her PhD degree from Cornell University in Ithaca, NY, still in Mechanical Engineering. In January 2013, she became the first PhD student of Dr. Robert Shepherd, who was a new Assistant Professor at Sibley School of Mechanical Engineering and Aerospace.

She worked on Soft Robotics under the advisement of Dr. Shepherd. Her research goal during her PhD pursuit was to improve the design of soft-bodied robots and relevant sensors, controllers to make them stronger, more accurate and smarter. She had two other committee members, Dr. Andy Ruina as an expert in robotic locomotion and Dr. Eve Donnelly as a material scientist devoted to biomaterials.

During her PhD pursuits, she gained a strong understanding of additive fabrication, soft materials and robotics and she determined to enter academia after graduation.

ACKNOWLEDGMENTS

I would like to thank my advisor, Professor Robert Shepherd, for all the encouragement, guidance, recognition, freedom and support he gave me during my entire PhD life; I would not have been able to complete my dissertation without him. I feel lucky to be his first PhD student.

I would like to thank Professor Andy Ruina, for him being such a great committee member by expressing so much interest in my research, giving me inspiring ideas and helping me editing my paper. I learnt a lot from this prestigious professor.

I would like to thank my third committee member, Professor Eve Donnelly, for showing a lot of patience and understanding during my degree pursuit.

I would like to thank my collaborators: Bratislav and Zoltan from ETH, Nic from Germany, Ross and Jon from Computer Science at Cornell.

I would like to show my sincere appreciation and respect for Joe, Craig and Marcia, our staffs in MAE, for all the help on the administrative aspect of my research.

I would like to thank my lab mates, Shuo, Sanlin, Ilse, Chris, Bryan, Ben, TJ, Kevin, James and Rukang. Without them, I would not have been able to experience such an interesting and coorperative journey of research.

I would like to thank my friends at Cornell, Qi, Fangxin, Yuan, Lin, Tian, Tianshu, Naigeng, Yi and Zhe, for all the good and fun time we spent together. I will never forget those memories with them at Cornell.

I would like to thank my boyfriend Ruihao at Colchester, UK, for being so supportive and considerate on my life and research during all these years. His encouragement made me keep on going when difficulties happened.

Finally, I would like to thank my amazing mom and dad for their selfless love. I thank them for bringing me up to the kind of person I am and supporting me no matter what decision I have made.

TABLE OF CONTENTS

LIST OF FIGURES

LIST OF TABLES

CHAPTER 1

INTRODUCTION

1.1 Soft robotics

Soft robots, defined as systems that are capable of autonomous behavior, and that are primarily composed of materials with moduli in the range of that of soft biological materials [1], provide a new paradigm for designing robots. Different from traditional robotic design, where the body, actuators, sensors, controllers and power sources are perfectly separated and are made of rigid materials [2], soft robotic systems have inseparable components [3] that are, most times, made of soft materials [4]. For example, the body of a typical fluidically powered soft robot is formed by soft actuators made from elastomers, which exhibit inherent compliance that enables the robotic body to achieve adaptive response to the environment. This mixture of functions and the new material selections boosted a new research area—soft robotics [1-2, 4-5].

Soft robotic systems have several advantages that are impossible or difficult to achieve using traditional robotic systems. First, soft robots usually have inherent compliance coming from the low elastic modulus of the body or actuators as well as the compressibility of the gas used to power them. This compliance enables the robots to deal with unpredictable and irregular environments in a simple manner [6], without sensors or controllers incorporated. For example, soft robots achieved grasping fragile and irregular objects [4] and crawling on unknown terrains [7] with just open-loop

control. Next, soft robotic systems are usually safe when interacting with humans [8] and comfortable to wear if used as exoskeletons. Traditional industrial robots work in places without humans and without considering safety issues and soft robots are safe to interact with because of their low stiffness and high adaptivity. Finally, the fabrication process for soft robots is usually simpler and are more likely to achieve mass-production [4]. Because of the above reasons, as well as recent technology development on materials and manufacturing techniques, soft robotics achieved fast development. In the next section, I will review the development history of soft robotics.

1.2 Literature review

Early-stage soft robotics research includes McKibben Artificial Muscle developed in the 1950s. McKibben muscle is actuated by compressed gas and has only one mode of motion—contraction. By using a pair of these muscles antagonistically, they could actuate a joint bidirectionally like human's muscle. Because of the compressibility of the actuating medium and the softness of the bladder, McKibben muscle shows compliant behavior and researchers have been utilizing this property to ease its control [9].

Started from the 1990s, along with the fast development of robotics where robots became more and more accurate, fast and could hold more payloads, researchers around the world started to look for alternative methods of designing robotic systems. Some of them approaches the problem by analyzing current rigid systems and reached the conclusion that elasticity or compliance will increase safety and introduce

intelligence to the original completely stiff system. Pratt et al. (1995) proposed incorporating series elasticity could increase shock tolerance, increase force accuracy and provide energy storage [10]. Suzumori et al. (1996) used soft materials to produce compliant robot in order to generate soft motions and gentle touch for a multifinger robotic hand [11]. Tsagarakis et al. (2003) proposed the need for and the use of soft actuators in an anthropomorphic robot [12]. Bicchi et al. (2004) proved that intentionally introducing compliance in the design would increase the safety level of robotic arms interacting with humans [8].

While the above researchers and scientists proposed and proved theoretically or experimentally incorporating compliance would improve the performance of existing robotic systems, especially in the safety aspect, other researchers approached this problem from bio-inspired views. They observed real-life animals and humans, and found that invertebrate animals achieved almost all their functions from soft tissues and even vertebrate animals achieved many functions from their soft organs. They mimic the mechanism of animals and humans and made soft-bodied robots from bioinspiration and biomimetics. Menciassi et al. (2004) proposed a shape memory alloy actuated artificial earthworm by mimicking the structure and locomotion of its natural counterpart [13]. Cutkosky et al. (2009) designed a gecko-inspired climbing robot that utilized multimaterial and compliant structure [14]. After reviewing various bio-inspired robots, Pfeifer et al. (2009) proposed the concept of morphological computation to design intelligent, adaptive robots [6]. Trimmer et al. (2011) designed a caterpillar-inspired soft-bodied rolling robot, which mimicked caterpillar's

locomotion mechanism [15]. Laschi et al. (2011) designed an octopus-inspired soft robotic arm that was made of soft materials [16] .

Started from 2010, soft robotics enters into a fast-growing period, largely due the development of soft materials and rapid prototyping techniques. In 2011, Ilievski et al. in Whitesides group of Harvard University published their work on soft robotics for chemists, where soft lithography was proposed for the first time to be used to make purely elastomeric robots [4]. Since then, the same fabrication techniques were conducted to prove more concepts and assumptions of fluidic elastomer actuators (FEAs): Shepherd et al. (2011) proposed a quadrupedal multigait soft robot, which proved soft robots could produce complex motion via simple design and control [17]. Tolley et al. (2014) proposed an untethered quadrupedal soft robot and proved the possibility of self-containing for soft robots and their ability to endure extreme environment [18]. Stokes et al. (2014) proved the combination of soft and hard robots by proposing a hybrid system [19]. Besides soft lithography, other rapid prototyping techniques have also been applied in soft robotics, like three-dimensional (3D) printing. Peele et al. (2015) used digital mask projection stereolithgraphy (another 3D printing technique) and printed multi degree of freedom soft tentacles [20]. MacCurdy et al. (2015) developed a 3D printing technique to print hydraulically actuated soft actuators [21]. Bartlett et al. (2015) used multimaterial 3D printing to print a functional soft robot that could jump [22].

Sensor incorporation and controller design for soft robots also gained rapid advances along with fabrication techniques. Ramuz et al. (2012) developed transparent, optical,

pressure sensitive artificial skin that could be used for soft robots [23]. Roberts et al. (2013) developed soft capacitive sensor to measure shear strain and elastic pressure for soft matters [24]. Kramer et al. (2013) has used masked deposition to fabricate Ga-In based elastomer conductive sensors [25]. Menguc et al. (2014) achieved large strain sensing by embedding liquid metal into the microfluidic channels of elastomers [26]. Muth et al. (2014) 3D printed stretchable strain sensor using conductive ink [27]. Most functional soft robots used open-loop control and utilized the inherent compliance to finish complex tasks. Duriez (2013) proposed using real-time finite element analysis to assist the nonlinear control of soft robots [28]. Marchese et al. (2014) has been working on the feedback control of a hydraulic, planar, soft robotic system based on computer vision and the low-level control used PID controller [29]. Morrow et al. (2016) achieved force and position control of a gripper via liquid-metal pressure sensor and strain sensor, also using PID controller [30].

Based on so many new technique developments and fundamental researches, soft robotics has achieved many applications in different areas. Current applications of soft robots include the following:

(i) Bioinspired robots with new functions. Marchese et al. (2014) developed a robotic fish based on FEAs that was capable of not only forward swimming but also rapid maneuvers [31]. Recent work of Wehner et al. (2016) combined several most advanced technologies, including actuator fabrication and power source fabrication for soft robots, and they developed a fully self-contained, autonomous octopus-inspired

robot [32]. Also, the possibility of developing bio-inspired robots provides chances for biologists to better understand the mechanism of natural animals as well.

(ii) Surgery robots. Cianchetti et al. (2014) investigated the feasibility of using stiffness-controllable soft actuators into minimally invasive surgery [33]. Sareh et al. (2014) further created miniaturized sensing elements for the compliant actuators to acquire tactile data during surgery [34].

(iii) Exoskeleton and prosthetics. Orthotics and prosthetics are robotic areas that are closest to humans being, thus safety and comfort outweigh other factors like accuracy and speed and soft robotics provide more chances of success than traditional robotics. Polygerinos et al. (2015) built up a soft glove that assisted in both rehabilitation training and activities of daily life for people with hand disabilities [35]. Yap et al. (2015) developed an fMRI-compatible soft glove for hand rehabilitation [36]. Deimel and Brock (2015) developed a fiber-reinforced soft hand that can achieve dexterous grasping of various objects [37].

(iv) Other areas. Other applications of soft robotics include architecture [38], education [39], agriculture, neuroscience, etc.

1.3 Challenges

Despite rapid and prosperous development in almost every aspect of soft robotics, there are still several challenging issues that need to be addressed to carry this area forward into more practical applications.

First issue lays in the fabrication method. The McKibben muscle is capable of generating large forces; this actuator, however, is limited in that it has only one mode of powered actuation: contraction. Other fluid powered soft actuators that are under development have many modes of actuation (bending, extending, and contracting) but are fabricated laboriously, usually by soft lithography, investment casting, or fiber winding. The useful actuator designs from these processes are limited as soft lithography is essentially a layup process, investment casting is costly, and fiber winding is practical in only very simple architectures. Additionally, actuators fabricated from soft lithography function by the expansion of thin elastomer membranes that burst at low pressures for the current choices of materials, and relies on adhesive layers that easily delaminate. For many future applications of soft robotics (e.g., prosthetics or therapeutic and surgical tools), mass production of complex actuator designs that apply high forces will be necessary.

Next issue is the sensing and control of soft robots. Despite soft robots possess intrinsic compliance, incorporation of sensing and control is still necessary to increase the accuracy and rapidity of motions, respond to environment change and interact with human beings. Most existing sensors are incompatible with these large strains. Commercially available flexible sensors usually suffer from low sensitivity, low repeatability and signal drift. Liquid-metal based resistive and soft capacitive sensors can be sensitive, but rely on expensive material or require a multi-step construction process. Computer vision can provide high quality position sensing, but the camera systems, besides being costly and complex, can interfere with the user's motion. Due

to these sensor limitations, most soft robots are still “open-loop”. Compared with other aspects of soft robotics, the effort going into the control of soft robots is very rare.

Last issue is in the power source of soft robots. Current power source for soft robots include: compressed air tank, air/liquid pump, and combustion. Compressed air tank is bulky and heavy and can hardly be untethered; pump is of low efficiency and speed; combustion is fast and simple to build up, but is only limited to momentum actuation. More suitable power systems for soft robots are highly required.

1.4 Dissertation scope and organization

Due to their continuous and natural motion, fluidically powered soft actuators have shown potential in a range of robotic applications including prosthetics and orthotics. In my dissertation, I focus on two issues for soft robotics: (i) fabrication, and (ii) sensing and control towards the application of hand prosthetics and orthotics. The application of my results is not limited to this space and can be expanded into other applications.

In Chapter 2, I adapted rotational casting as a new manufacturing method for soft actuators. The criteria for both mold design and material properties of the elastomeric precursors to produce networks of pneumatic channels are described. I present a cuboid soft actuator that can generate a force of >25 N at its tip, a near ten-fold increase over similar actuators previously reported. Additionally, I used this manufacturing technique and fabricated a wearable assistive device for increasing the force a user can apply at their fingertips.

In chapter 3, I proposed a soft orthotic with position control enabled via an embedded optical fiber based strain sensor. The design, manufacture, and integration of both the pneumatically powered actuators and optical sensors are described. This orthotic actuator-sensor pair is self-contained and worn on a human finger. When un-powered, the elastomeric actuator allows facile movement and, when pneumatically actuated, the orthotic causes bending of the wearer's finger. Position control is achieved by measurement of signal intensity from a light-emitting diode (LED) input traveling through an embedded optical fiber—greater curvature results in increased light intensity. Both the static and dynamic states are monitored via the optical sensor and the prescribed curvatures are achieved accurately and with stability by a gain-scheduled proportional-integral-derivative (PID) controller implemented by applying pulse-width-modulation (PWM) signals to a solenoid valve to adjust the internal pressure of the actuator.

In Chapter 4, I developed the soft orthotic fingers in Chapter 3 into a closed-loop controlled soft orthotic with integrated curvature sensors. My goal is a low cost soft orthotic that can be worn by a typical human hand and provide enough tip force at each finger to be helpful for grasping light objects (e.g., fruits), while also providing finger position (defined as average curvature) control. I have achieved reasonable functionality at these goals by using three advances described in this chapter: (i) a new rotational-casting technique as described in Chapter 2, followed by an over-molding process for making the glove; (ii) measuring finger motion through optical losses in a molded-into-place etched plastic fiber-optic cable as described in Chapter 3; and (iii) controlling motion with inexpensive, binary pneumatic switches controlled by a

simple finite-state-machine. The composite glove is purely polymeric, highly compliant, and provides little resistance to natural motion when not pressurized. When inflated, the fingers of the glove curve and stiffen.

In Chapter 5, I report the first use of stretchable optical waveguides for strain sensing in a prosthetic hand. These optoelectronic strain sensors are easy to fabricate, chemically inert, and demonstrate low hysteresis and high precision in their output signals. As a demonstration of their potential, the photonic strain sensors are used as curvature, elongation, and force sensors integrated into a fiber reinforced soft prosthetic hand. The optoelectronically innervated prosthetic hand is used to conduct various active sensation experiments inspired by the capabilities of a real hand. My final demonstration uses the prosthesis to feel the shape and softness of three tomatoes and select the ripe one.

REFERENCES

[1] D. Rus and M. T. Tolley, Design, fabrication and control of soft robots, *Nature* **521**, 467–475 (2015).

[2] D. Trivedi, C. D. Rahn, W. M. Kier, and I. D. Walker, Soft robotics: Biological inspiration, state of the art, and future research. *Appl. Bionics Biomech.* **5**, 99–117 (2008).

[3] M. A. McEvoy and N. Correll, Materials that couple sensing, actuation, computation, and communication, *Science* **347**, 126168 (2015).

[4] F. Ilievski, A. D. Mazzeo, R. F. Shepherd, X. Chen, and G. M. Whitesides, Soft robotics for chemists. *Angew. Chemie - Int. Ed.* **50**, 1890–1895 (2011).

[5] A. Albu-Schaffer, O. Eiberger, M. Grebenstein, S. Haddadin, C. Ott, T. Wimböck, S. Wolf, and G. Hirzinger, Soft robotics. *IEEE Robot. Autom. Mag.* **15**, 20–30 (2008).

[6] R. Pfeifer, M. Lungarella, and F. Iida, Self-organization, embodiment, and biologically inspired robotics. *Science* **318**, 1088–93 (2007).

[7] R. F. Shepherd, F. Ilievski, W. Choi, S. a. Morin, A. A. Stokes, A. D. Mazzeo, X. Chen, M. Wang, and G. M. Whitesides, Multigait soft robot. *Proc. Natl. Acad. Sci.* **108**, 20400–20403 (2011).

[8] A. Bicchi and G. Tonietti, Fast and 'soft-arm' tactics. *IEEE Robot. Autom. Mag.* **11**, 22–33 (2004).

[9] B. Tondu, V. Boitier, and P. Lopez, Naturally compliant robot-arms actuated by McKibben artificial muscles, in *Proceedings of 1994 IEEE International Conference on Systems, Man, and Cybernetics*, 2 to 5 Octorber 1994, pp. 2635–2640.

[10] G. A. Pratt and M. M. Williamson, Series elastic actuators. *in Proceedings of 1995 IEEE/RSJ International Conference on Intelligent Robots and Systems*, 5 to 9 August 1995, pp. 399–406.

[11] K. Suzumori, Elastic materials producing compliant robots. *Rob. Auton. Syst.* **18**, 135–140 (1996).

[12] N. G. Tsagarakis and D. G. Caldwell, Development and control of a 'soft-actuated' exoskeleton for use in physiotherapy and training. *Auton. Robots*. **15**, 21–33 (2003).

[13] A. Menciassi, S. Gorini, G. Pernorio, L. Weiting, F. Valvo, and P. Dario, Design, Fabrication and Performances of a Biomimetic Robotic Earthworm. in *Proceedings of 2004 IEEE International Conference of Robotics and Biomimetics*, 22 to 26 August 2004, pp. 274–278.

[14] M. R. Cutkosky and S. Kim, Design and fabrication of multi-material structures for bioinspired robots, *Philos. Trans. A. Math. Phys. Eng. Sci.* **367**,1799-1813 (2009).

[15] H. T. Lin, G. G. Leisk, and B. Trimmer, GoQBot: a caterpillar-inspired soft-bodied rolling robot. *Bioinspir. Biomim.* **6**, 26007 (2011).

[16] C. Laschi, M. Cianchetti, B. Mazzolai, L. Margheri, M. Follador, and P. Dario, Soft Robot Arm Inspired by the Octopus. *Adv. Robot.* **26**, 709–727 (2012).

[17] R. F. Shepherd, F. Ilievski, W. Choi, S. a. Morin, A. A. Stokes, A. D. Mazzeo, X. Chen, M. Wang, and G. M. Whitesides, Multigait soft robot. *Proc. Natl. Acad. Sci. U. S. A.* **108**, 20400–20403 (2011).

[18] M. T. Tolley, R. F. Shepherd, B. Mosadegh, K. C. Galloway, M. Wehner, M. Karpelson, R. J. Wood, and G. M. Whitesides, A Resilient, Untethered Soft Robot. *Soft Robot.* **1**, 213–223 (2014).

[19] A. A. Stokes, R. F. Shepherd, S. a Morin, F. Ilievski, and G. M. Whitesides, A Hybrid Combining Hard and Soft Robots. *Soft Robot.* **1**, 70–74 (2014).

[20] B. N. Peele, T. J. Wallin, H. Zhao, and R. F. Shepherd, 3D printing antagonistic systems of artificial muscle using projection stereolithography. *Bioinspir. Biomim.* **10**, 55003 (2015).

[21] R. Maccurdy, R. Katzschmann, Y. Kim, and D. Rus, Printable Hydraulics: A Method for Fabricating Robots by 3D Co-Printing Solids and Liquids. in *Proceedings of the 2016 IEEE International Conference on Robotics and Automation*, 16 to 21 May 2016, Stockholm, Sweden, pp. 3878–3885.

[22] N. W. Bartlett, M. T. Tolley, J. T. B. Overvelde, J. C. Weaver, B. Mosadegh, K. Bertoldi, G. M. Whitesides, and R. J. Wood, Robot Powered By Combustion. *Science* **349**, 161–165 (2015).

[23] M. Ramuz, B. C. K. Tee, J. B. H. Tok, and Z. Bao, Transparent, optical, pressure-sensitive artificial skin for large-area stretchable electronics. *Adv. Mater.* **243**, 223–3227 (2012).

[24] P. Roberts, D. D. Damian, W. Shan, T. Lu, and C. Majidi, Soft-matter capacitive sensor for measuring shear and pressure deformation. in *Proceedings of the 2013 IEEE International Conference on Robotics and Automation*, 6 to 10 May 2013, Karlsruhe, Germany, pp. 3529–3534.

[25] R. K. Kramer, C. Majidi, and R. J. Wood, Masked deposition of gallium-indium alloys for liquid-embedded elastomer conductors. *Adv. Funct. Mater.* **23**, 5292–5296 (2013).

[26] Y. Menguc, Y. L. Park, H. Pei, D. Vogt, P. M. Aubin, E. Winchell, L. Fluke, L. Stirling, R. J. Wood, and C. J. Walsh, Wearable soft sensing suit for human gait measurement. *Int. J. Rob. Res.* **33**, 1748–1764 (2014).

[27] J. T. Muth, D. M. Vogt, R. L. Truby, Y. Mengüç, D. B. Kolesky, R. J. Wood, and J. A. Lewis, Embedded 3D printing of strain sensors within highly stretchable elastomers. *Adv. Mater.* **26**, 6307–6312 (2014).

[28] C. Duriez, Control of elastic soft robots based on real-time finite element method. in *Proceedings of the 2013 IEEE International Conference on Robotics and Automation*, 6 to 10 May 2013, Karlsruhe, Germany, pp. 3982–3987.

[29] A. D. Marchese, K. Komorowski, C. D. Onal, and D. Rus, Design and Control of a Soft and Continuously Deformable 2D Robotic Manipulation System. in *Proceedings of the 2014 IEEE International Conference on Robotics and Automation*, 31 May to 7 June 2014, Hong Kong, China, pp. 2189–2196.

[30] J. Morrow, H. S. Shin, C. Phillips-Grafflin, S. H. Jang, J. Torrey, R. Larkins, S. Dang, Y. L. Park, and D. Berenson, Improving Soft Pneumatic Actuator fingers through integration of soft sensors, position and force control, and rigid fingernails. in *Proceedings of the 2016 IEEE International Conference on Robotics and Automation*, 16 to 21 May 2016, Stockholm, Sweden, pp. 5024–5031.

[31] A. D. Marchese, C. D. Onal, and D. Rus, Autonomous Soft Robotic Fish Capable of Escape Maneuvers Using Fluidic Elastomer Actuators. *Soft Robot.* **1**, 75–87 (2014).

[32] M. Wehner, R. L. Truby, D. J. Fitzgerald, B. Mosadegh, G. M. Whitesides, J. A. Lewis, and R. J. Wood, An integrated design and fabrication strategy for entirely soft, autonomous robots. *Nature* **536**, 451–455 (2016).

[33] M. Cianchetti, T. Ranzani, G. Gerboni, T. Nanayakkara, K. Althoefer, P. Dasgupta, and A. Menciassi, Soft Robotics Technologies to Address Shortcomings in Today's Minimally Invasive Surgery: The STIFF-FLOP Approach. *Soft Robot.* **1**, 122–131 (2014).

[34] S. Sareh, A. Jiang, A. Faragasso, Y. Noh, T. Nanayakkara, P. Dasgupta, L. D. Seneviratne, H. A. Wurdemann, and K. Althoefer, Bio-inspired tactile sensor sleeve for surgical soft manipulators. in *Proceedings of the 2014 IEEE International Conference on Robotics and Automation*, 31 May to 7 June 2014, Hong Kong, China, pp. 1454–1459.

[35] P. Polygerinos, K. C. Galloway, E. Savage, M. Herman, K. O'Donnell, and C. J. Walsh, Soft robotic glove for hand rehabilitation and task specific training. in *Proceedings of the 2015 IEEE International Conference on Robotics and Automation*, 26 to 30 May 2015, Seattle, USA, pp. 2913–2919.

[36] H. K. Yap, J. H. Lim, F. Nasrallah, F. Z. Low, J. C. H. Goh, and R. C. H. Yeow, MRC-glove: A fMRI compatible soft robotic glove for hand rehabilitation application. in *Proceedings of the 2015 IEEE International Conference on Rehabilitation Robotics*, 11 to 14 August 2015, Singapore, Singapore, pp. 735–740.

[37] R. Deimel and O. Brock, A novel type of compliant and underactuated robotic hand for dexterous grasping. *Int. J. Rob. Res.* **35**, 161–185 (2016).

[38] B. Svetozarevic, J. Hofer, D. Jacob, M. Begle, and E. Chatzi, "SoRo-Track : A Two-Axis Soft Robotic Platform for Solar Tracking and Building-Integrated Photovoltaic Applications," in *Proceedings of the 2016 IEEE International Conference on Robotics and Automation*, 16 to 21 May 2016, Stockholm, Sweden, pp. 4945–4950.

[39] B. Finio, R. Shepherd, and H. Lipson, Air-powered soft robots for K-12 classrooms. in *Proceedings of the 2013 IEEE Integrated STEM Education Conference*, 9 March 2013, pp. 1–6.

CHAPTER 2

SCALABLE MANUFACTURING OF HIGH FORCE WEARABLE SOFT ACTUATORS*

2.1 Introduction

Soft machines are emerging as a new component in robotics that allow for simpler operation of complex functions (e.g., robotic manipulators) [1-3], more natural motions [4-7], and new functions (e.g., climbing walls) [8]. In many cases, these machines are actuated by pneumatically powered balloons composed of elastomers [1-3, 9, 10]: increasing their inflated pressure results in greater stiffness and shape change. At low or zero inflation pressures, these actuators exhibit low stiffness and cause limited resistance to movement as wearable devices and human interfaces. As a result, there is a growing effort to use soft actuators for exoskeletons and prosthetics that can augment the force of, or altogether replace, human grasping and locomotion, as well as perform physical therapy tasks [11-13].

The McKibben muscle (a fiber-reinforced soft actuator) was developed over six decades ago and is capable of large ranges of stiffness as a function of pressure [14]; for example, Fluidic Muscle DMSPTM (Festo, Inc.) can be inflated from 0 to ~800 kPa (~120 psi) [15]. This actuator, however, is limited in that it has only one mode of powered actuation: contraction. Other fluid powered soft actuators that are under

* H. Zhao, Y. Li, A. Elsamadisi, and R. F. Shepherd, Scalable manufacturing of high force wearable soft actuators. *Extreme. Mech. Lett.* **3**, 89-104 (2015).

development have many modes of actuation (bending, extending, and contracting) [16-18] but are fabricated laboriously, usually by replica molding [1, 3], investment casting [19], or fiber winding [20]. The useful actuator designs from these processes are limited as replica molding is essentially a layup process, investment casting is costly, and fiber winding is practical in only very simple architectures. Additionally, replica molded actuators function by the expansion of thin elastomer membranes that burst at low pressures for the current choices of materials [21], and relies on adhesive layers that easily delaminate. For many future applications of soft robotics (e.g., prosthetics or therapeutic and surgical tools), mass production of complex actuator designs that apply high forces will be necessary.

In this chapter, I describe the manufacturing process of soft actuators using rotational casting, a reliable and high throughput production method. I present criteria for both the mold designs and required material parameters of the elastomeric precursors. To demonstrate this method's utility, we rotationally casted a soft actuator that can generate a force of >25 N at its tip, a near ten-fold increase over similar actuators previously reported [12]. Additionally, we fabricated and tested a wearable, assistive device for increasing the force a user can apply at their fingertips.

2.2 Experimental Design

We chose to rotationally cast our actuators (Figure 2.1(a)) because it is an established process for high volume fabrication of hollow, monolithic structures (e.g., boat hulls and chocolate eggs). We used a 3D printer (Scholar 30, Objet, Inc.) to fabricate both the rotational casting machine and to rapidly iterate molds for the actuators. To

compare our rotational casted actuators to existing ones, we used a similar design to elastomeric, pneumatic network (Pneu-Nets) [1] and characterized them by testing their applied tip force at varying internal pressures at a fixed curvature. To fabricate force augmentation devices for a human hand, we designed soft actuators based on the shape of a finger.

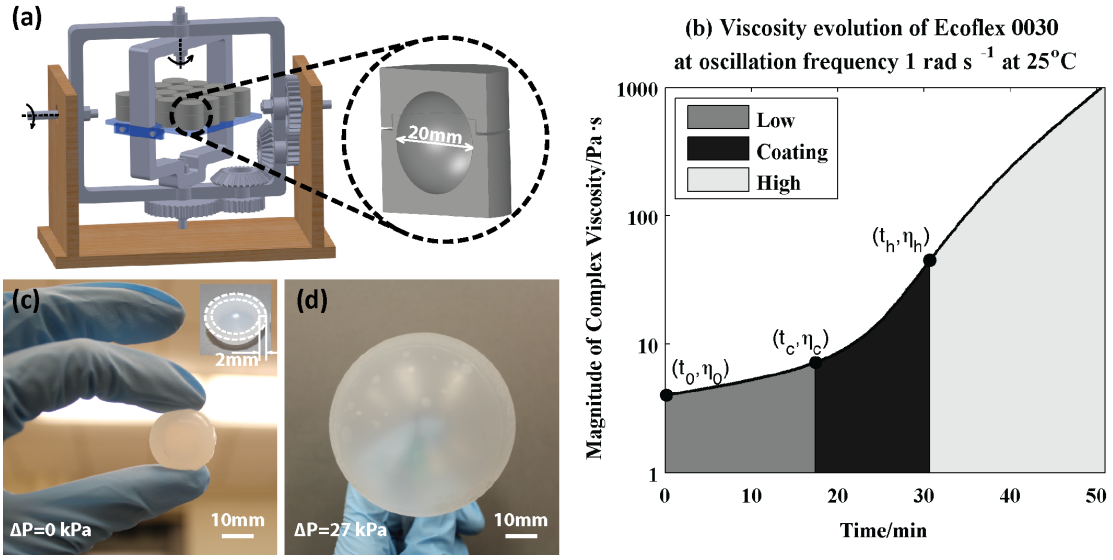

Figure 2.1 Biaxial rotational casting system and a sperical actuator. (a) Biaxial rotational casting system with multiple spherical molds, (b) complex viscosity evolution of Ecoflex 0030 at oscillation frequency of 1 rad/s at 25 °C, (c) rotational cast spherical actuator with inset of cross-section, and (d) inflated spherical actuator at ΔP=27 kPa.

To intuitively actuate the force augmentation device, we attached electromyography (EMG) sensors (Muscle Sensor v3, Advancer Technologies) to muscles in the forearm to trigger the finger actuators because they are low in cost and easy to implement. The electrical impulses detected by the EMG sensors open and close solenoid valves (Solenoid Air Directional Control Valve, McMaster) in line with the compressed air for powering the actuator. We chose a pneumatic power source because air is inviscid,

thus can be delivered rapidly, and it can have an energy density similar to lithium polymer batteries for use in untethered operation [22].

Due to the complexity of the rotational flow fields of our viscoelastic precursors, I determined the dependence of machine and material parameters for fabricating a soft actuator using a simplified analytical model for Newtonian fluids and observing, experimentally, the flow conditions through transparent molds. I used Matlab® to simulate the trajectories of mold elements during rotation and used the results to determine the gear ratios in our machine to uniformly coat the interior of the molds. The rheological properties of the viscoelastic pre-elastomers we used were measured at an oscillatory frequency comparable to the strain rate of flows in our system using the Cox-Merz rule [23].

2.3 Experimental Methods

Table 2.1 describes the material properties of the elastomers we used for rotational casting. We measured the rheological properties using a Discovery Hybrid Rheometer from TA Instruments. The initial viscosities were tested at oscillation frequency of 1 rad/s at 25 °C, and the same oscillation frequency and temperature were used for all viscometry. We conducted tensile tests (ASTM D412) using Zwick/Roell Z010 to measure all the elastomers' mechanical properties. We used Silicone Thinner (a non-reactive silicone fluid from Smooth-On, Inc.) to lower the viscosities of the materials for compatibility with rotational casting.

We chose the axial speed ratio to be 47/36. The input rotational speed was a constant 6 revolutions/min for all actuator designs. We rotated the molds filled with Ecoflex 0030 for 45 minutes and cured them in a 60 °C oven for 15 minutes. We chose ELASTOSIL M4601 a/b and added 15% of ST to rotational cast cuboid actuators for characterization and finger exos. We encapsulated the cuboid actuator using ELASTOSIL M4601 a/b without ST. We rotated the molds filled with pre-elastomers for 3 hours and placed them in an oven at 60 °C for 1 hour to fully cure.

Table 2.1 Rheological and mechanical properties of materials used

Material name	Initial viscosity [Pa·s][a])	100% elastic moduli [MPa][b])	Ultimate strength [MPa][b])	Ultimate elongation [%][b])
Ecoflex 0030 (from Smooth-On, Inc.)	4.0	0.04	0.8	670
Ecoflex 0050 (from Smooth-On, Inc.)	7.9	0.06	1.2	800
ELASTOSIL M4601 a/b (from Wacker Chemical Corp.)	16.2	0.46	4.4	760
ELASTOSIL M4600 a/b (from Wacker Chemical Corp.)	39.2	0.54	4.0	620

[a)] Tested at oscillatory angular velocity 1 rad/s, oscillatory strain amplitude 10% at 25 °C;
[b)] Tested under ASTM D412.

2.4 Results and Discussions

2.4.1 Parameters of the rotational casting system

The majority of rotational casting processes use a frame with two axes of rotation to coat the interior of a heated, hollow mold. During rotation, a molten thermoplastic resin coats the mold surface, then the system is cooled until the material falls below its glass transition temperature and becomes stiff [24]. Though some thermoplastic

elastomers may be compatible with rotational casting of soft actuators (e.g. Elastollan from BASF), the elastomers currently used in soft robots are cured using radical or condensation polymerization [1-5, 7, 9, 12,13, 16-22].

The rotational casting system we developed for fabricating soft actuators uses materials that are liquid at room temperature and polymerize into soft elastomers during the casting process. This system has four parameters that must be tuned: (i) viscosity evolution during casting; (ii) rotational speed of the primary axis, ω_x; (iii) axial speed ratio of the machine, r; and (iv) the internal surface geometry of the two-part molds.

As the elastomeric material gels, the viscosity increases towards infinity [25], and there is an increasing resistance to flow from external forces such as gravity, normal force and drag from the mold during rotational casting. Using rheometery, we have identified three important viscosity regimes for the rotational casting of thermosetting elastomers (Figure 2.1(b)): low, when the initial viscosity, η_0, allows the material to flow too fast to rotate with the mold; coating, where the polymer has reached a threshold viscosity, η_c, large enough to spread along the interior surface; and high, when the gelling elastomer has exceeded another threshold viscosity, η_h, and no longer flows fast enough to uniformly coat regardless of the number of rotational cycles.

The lower threshold of low regime flow rate is entirely dependent on η_0; however, the coating and high regimes are also dependent on the characteristics of the rotational casting machine and the mold geometry. To determine the dependence of the threshold viscosities (η_c and η_h) on rotational casting parameters we used a slowly rotating

hollow spherical mold, the slow rotation ensures gravity is the primary driving force for flow and the sphere geometry simplifies analysis. Assuming a steady state, no-slip, laminar flow of incompressible Newtonian fluid (see Section 2.6.2 for derivation and assumption validation) we found the dependence of η_c and η_h on the machine and mold parameters:

$$\eta_c = \frac{\pi}{6}\frac{\rho g}{\omega_x R \cdot f(r)}\bar{h}^2 \qquad \text{(Equation 2.1)}$$

$$\eta_h = \frac{\eta_c}{\alpha} \qquad \text{(Equation 2.2)}$$

with elastomer density, ρ, gravitational constant, g, rotational velocity of the primary axis, ω_x, mold radius, R, average coating thickness, $\bar{h}$, speed ratio of the secondary to the primary axis, r, and $f(r) = \frac{\int_0^{2\pi}\sqrt{1+r^2cos^2\varphi}d\varphi}{2\pi}$, which is an increasing function of r describing how r affects mold speed in biaxial rotation. α is an empirically determined value (ideally, α = 0, which indicates pre-elastomers are still relative to the mold; in our experiment, α = 0.05, which indicates the speed of pre-elastomers only achieve 5% of the mold speed). Using the typical material and machine parameters used in our experiments ($\rho \sim 10^3$ kg/m^3, ω_x = 6 rev/min, R = 10 mm, $\bar{h}$ = 2 mm, $r \sim 1.25$) we find the threshold viscosities for coating are $\eta_c \sim 2.6$ Pa·s, $\eta_h \sim 52$ Pa·s.

To verify our analytical model, we used transparent molds to observe the ability of silicone pre-elastomers to form coatings at increasing viscosities (Figure 2.12). Using the same parameters for our analytical model, we found good agreement with η_c^{exp}=7.1 Pa·s and η_h^{exp}=42 Pa·s. We believe our underprediction of η_c is due to our steady state

analysis not accounting for the initial pool of material at the bottom of the mold. The resulting spherical actuator, fabricated from Ecoflex 0030, is capable of changing volume by 2200 % at an internal pressure, ΔP ~27 kPa (ΔP ~4 psi; Figure 2.1(c, d)).

Other materials that have different viscosity evolutions of their pre-elastomers can be modified for use in this process via the addition of Silicone Thinners (ST; Smooth-On, Inc.). Adding ST to Elastosil M4601 a/b (Wacker Chemical Corp.; Figure 2.12), allows a similar η_0 to Ecoflex 0030. We found that high concentrations of ST affects the cured properties of the elastomer (Figure 2.13), and thus we kept these concentrations below 20% by volume. Though it is also possible to tune a material's viscosity evolution profile using temperature (Figure 2.14; increasing the material available for rotationally casting elastomers), we did not use that feature to fabricate devices in this paper.

Simulated trajectories of a mold element (Figure 2.2) indicate that its initial position determines the coverage area, while speed ratio, r, determines the coverage density. Elements on the pole (Figure 2.2(a)) always cover a circle independent of r, elements on the equator (Figure 2.2(d)) cover the entire sphere surface, and elements between them (Figure 2.2(b, c)) partially cover the sphere surface area. By choosing r=46/37, we achieved the greatest coverage density, which resulted in a more homogenous material distribution. Though these gear ratios appear similar in value (1.25, 1.27, 1.24), the least common multiple of the numerator and denominator (20, 154, 1702) are dramatically different and result in different coating abilities (see Secion 2.6.1 for a detailed explanation).

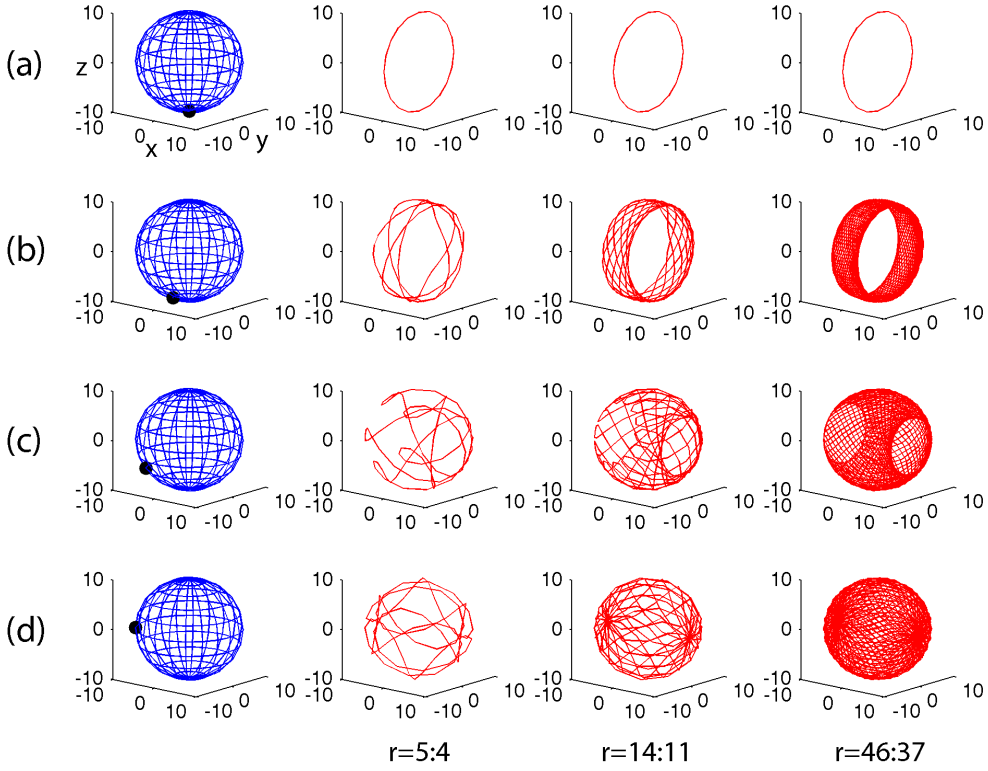

Figure 2.2 Simulated element trajectories of four different positions on the mold under three axial speed ratios: 5:4, 14:11 and 46:37. The simulations were run for one biaxial rotational cycle for each speed ratio in Matlab®. The first column shows the initial position of the element simulated in black marker: row (a) shows the simulations of an element on the pole; row (b) shows the simulations of an element between the pole and the equator; row (c) shows another element between the pole and equator but closer to the equator; row (d) shows an element on the equator.

For more complex actuators, the mold design is critical. Figure 2.3(a, b) shows the functional design of a bending actuator. The profile of the mold's interior structure shows a flat side and a wavy array of channels that form the pneumatic network. Before rotational casting, we place a layer of nylon fiber mesh on the flat side of the mold to limit the strain in this location while actuated. During rotational casting, the material distributes along the interior structures and polymerizes into a monolithic part

as shown in Figure 2.3(c). When pressurized, the wavy portion stretches and the strain-limiting area does not, causing bending (Figure 2.3(e)).

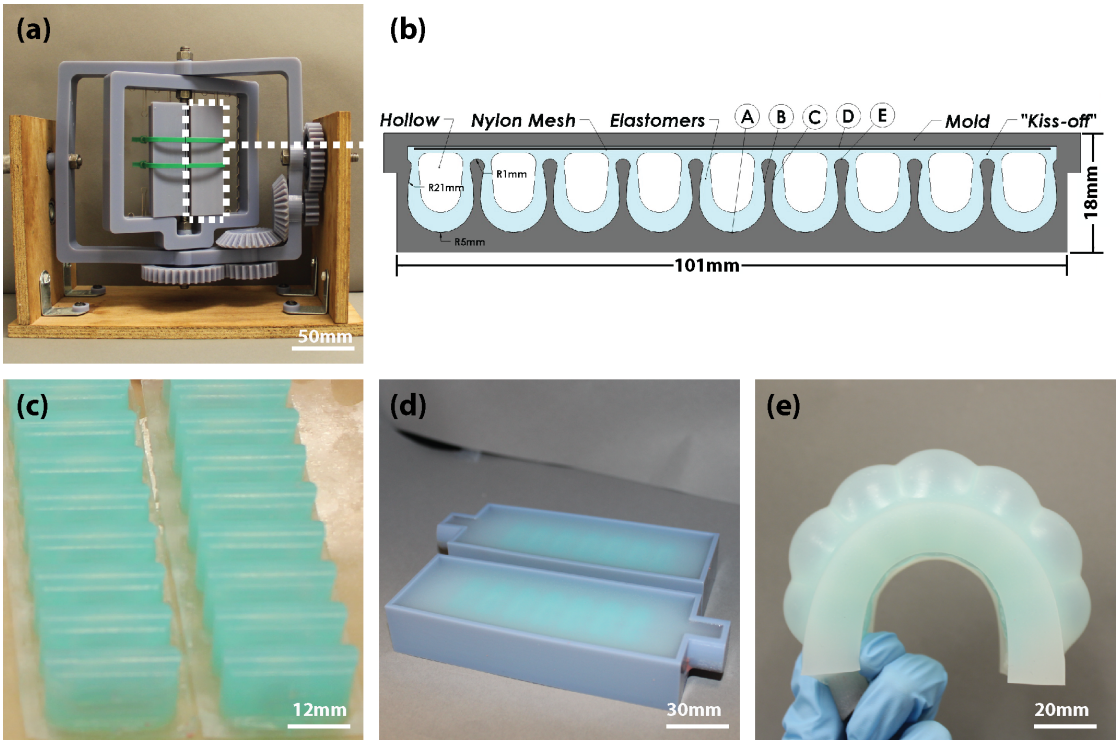

Figure 2.3 Rotational casting process. (a) Rotational casting machine with multiple molds, (b) profile of interior structure of a cuboid soft actuator mold and elastomer coating, (c) rotationally cast monoliths, (d) encapsulation and (e) inflation the cuboid actuator.

Concave mold geometries (Figure 2.3(b), points A-C) accumulate more material than flat or convex features, and the larger the curvature the thicker the coating (e.g., wall thickness at point A is greater than points B and C). On the contrary, convex points (Figure 2.3(b), point E) tend to have vanishingly thin walls. In order to overcome this problem, we designed the distance between the strain limiting layer (D) and the convex portion (E) to be smaller than twice the average thickness of the coating, so the material on both sides build up and “kiss off” each other. This “kiss-off” feature is widely used in industrial rotational molding to increase the stiffness of plastic parts

[24]. By using this feature, the rotational cast part is monolithic and composed of a series of separate units connected by a common flat layer (Figure 2.3(c)).

To apply compressed air to each unit of the actuator, we inserted a steel wire through each chamber and encapsulated it using the same elastomer (Figure 2.3(d)). After encapsulation, we removed the wire and applied pressure; Figure 2.3(e) shows the curvature at 40 kPa (6 psi). We also use the encapsulating layer for two other functions—providing a human to machine interface and adding the desired amount of structural stiffness.

As this method relies on gravity to coat the mold interiors, the same downward force is exerted at all points in the machine; therefore, multiple actuators can be cast simultaneously. To demonstrate the scalability of this manufacturing method, we fixed multiple molds on the machine and cast them in one set (see Figure 2.3(a, c)).

2.4.2 Force tests of cuboid actuators

ELASTOSIL M4601 (a tougher silicone than Ecoflex 0030, Table 2.1) with 15% ST has an appropriate viscosity profile for rotational casting actuators (Figure 2.14). Using this material, we were able to cast cuboid actuators that generated high forces when pressurized Figure 2.4(a)). At inflation pressure of 167 kPa (~25 psi), we were able to place a 0.5 kg weight on it with no obvious deformation. As many applications for actuators depend on the force applied at the end of the effector, we measured the tip force exerted over increasing pressures at two different curvatures, κ, using a blocking force measurement (Figure 2.4(b, c); Section 2.6.5). We used curvature as a metric as

it is an important parameter for exoskeletons design; for example, actuators for fingers were measured to be $\kappa \sim 20$ m^{-1} and elbows, $\kappa \sim 10$ m^{-1}. Figure 2.4(c) shows the tip force is zero until the actuator contacts the block, and then increases approximately linearly with inflated pressure, with larger rate for smaller curvature constraint. The maximum pressure and maximum force we tested for these rotational cast actuators are 234 kPa (34 psi) and 27.4 N, which exceeds pneumatic bending actuators of similar dimensions and purely elastomeric material made from replica molding [12].

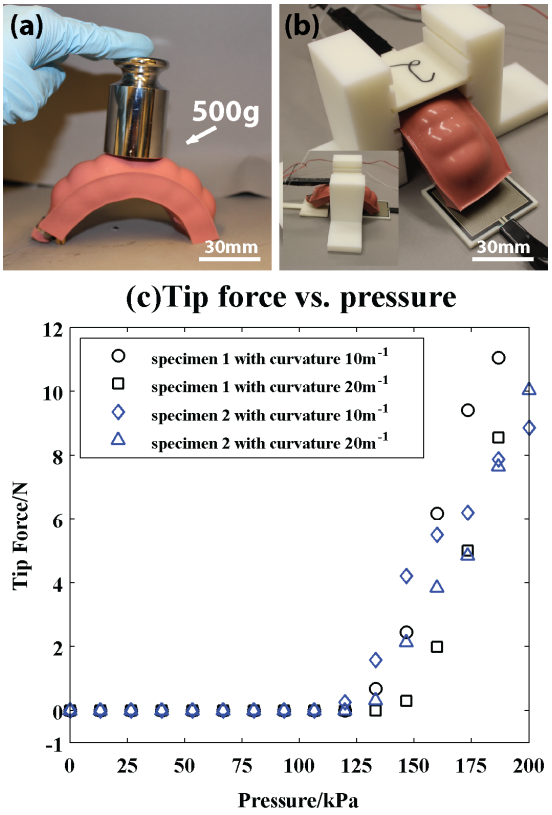

Figure 2.4 Force tests for rotational casted actuators. (a) Inflated cuboid actuator with a 0.5 kg weight on its top, (b) force test set up and (c) tip force vs. pressure of three specimens with two different curvatures.

2.4.3 EMG triggered finger actuator

We designed a wearable actuator (exo) for a human finger where the only constraint in natural movement, when unpowered, comes from the resilience of the stretched, low elastic modulus silicone (Table 2.1). To further reduce constraint during movement, we used thin actuators (thickness ~ 6 mm; Figure 2.5(a)), which we then coated (Figure 2.5(b)) in a thin encapsulating layer. This layer also formed three circular bands to secure it to human hand, and a protrusion we used to clamp the pneumatic tether (see Section 2.6.4 for mold details). This actuator demonstrates limited resistance to the free movement of a finger as shown in Figure 2.5(c) and generates a force of 4.0 N when pressurized at 140 kPa (~21 psi) and $\kappa \sim 20$ m^{-1} (Figure 2.5(d)).

A large programmable range of stiffness when pressurized makes these actuator great candidates for both exoskeletons and prosthetics. To demonstrate their utility, we prototyped a simple human-controlled finger exo. This system uses an electromyographic (EMG) sensor and microcontroller that opens and closes a solenoid valve in line with compressed air to power the finger actuator in Figure 2.5 (Video 2.1; see Section 2.6.5 for more details). The EMG is attached to the forearm where the muscles control finger movements (i.e., flexor digitorum profundus muscle) are located, and by reading the electrical activity of the muscles, we were able to sense their contraction. Upon sensing this action, the microcontroller opens the valve and pressurizes the finger actuator. Figure 2.5(e) demonstrates the EMG signal change over time, the corresponding valve state, and the finger actuator movement. When the user's finger is at rest, the EMG signal is low and the finger actuator is uninflated;

when they begin to pick up a 2 kg weight, the EMG signal increases until it reaches a threshold and the finger actuator is rapidly inflated. To deflate the actuator, the user then squeezes to trigger another impulse of the EMG signal, which closes the valve and deflates the finger actuator.

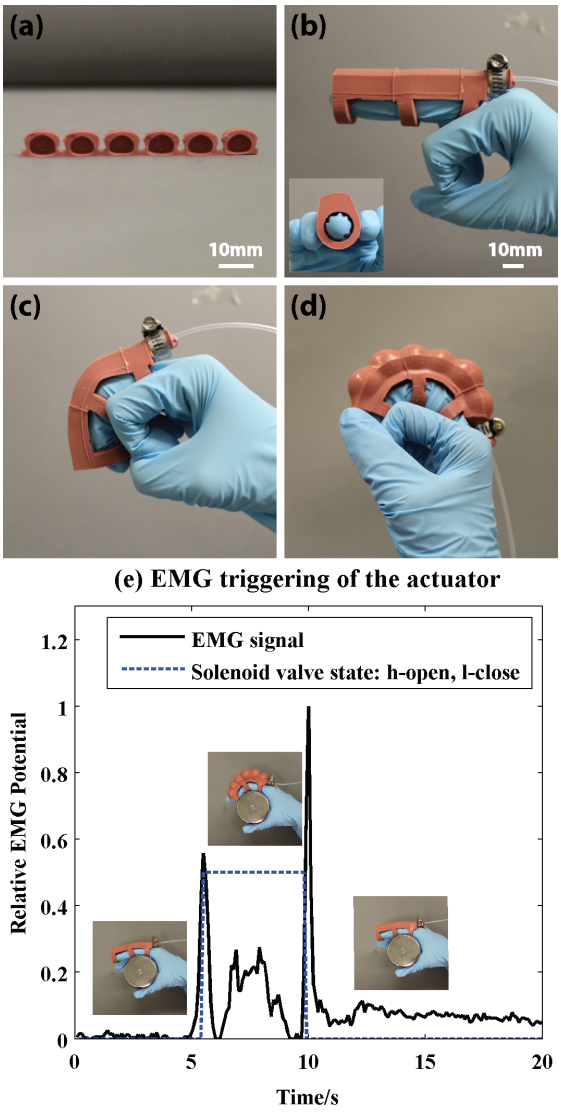

Figure 2.5 EMG controlled soft finger worn by a hand. (a) Rotationally casted, pneumatic network monolith, (b) encapsulted into exoskeleton form and placed on a finger, (c) uninflated finger actuator bends with finger, (d) inflated finger actuator and (e) EMG signal while sensing muscle activation. [b-d scale is identical]

2.5 Conclusions

I have developed a design and manufacturing method for fabricating monolithic soft machines via rotational casting. As the resulting actuators have no seams, they fail only due to the ultimate strength of the materials (or flaws therein) and not due to assembly errors; as a result, they can attain high pressure and apply relatively large forces. In this chapter, I have shown three different actuators: spherical, bending, and a finger exo that has the potential for augmenting the force of users with reduced musculature or enhancing the applied force beyond normal human abilities. The fabrication technique can be extended to a large variety of complex internal architectures.

Compared with traditional fabrication methods, our process has three advantages: (i) it uses thermosetting elastomers (e.g., silicones, urethanes, acrylates, styrene-butadiene rubbers) which are common materials currently in use and desirable for soft robotics [1]; (ii) it simplifies the soft machine fabrication process; (iii) many actuators can be fabricated simultaneously (Figure 5.4(a), Section 2.6.1). Presently, the generated force by the finger actuator (~4.0 N) is still insufficient to replace human limbs to manipulate heavy objects. By using an integrative mold design, a glove and sleeve assist device could be fabricated in one step, and using tougher materials (e.g. polyurethanes) will allow significant augmenting force for the movement of appendages.

Our machine and molds (see Section 2.6 or web link to digital CAD files) are currently limited in scale by the build area of available 3D printers. In principle, however, much

larger rotational casting machines are already in use and could be adapted for full exoskeletons or fabricating thousands of actuators simultaneously. Additionally, using the same design principles and thermoplastic elastomers, we could produce large soft robots using industrial equipment. Finally, it is common in industry to co-mold and over-mold objects with the rotationally casted form; therefore, it should be straightforward to incorporate sensors, motors, and power sources directly into exoskeleton systems and prosthetics.

2.6 Supplementary Materials

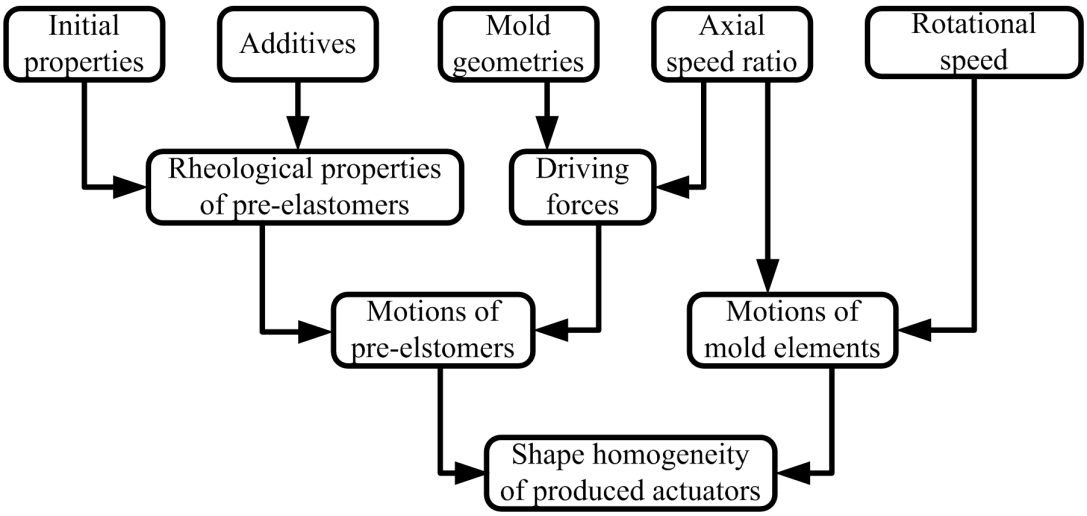

Figure 2.6 Relationships of different parameters in rotational casting system

Producing consistent and strong actuators using rotational casting requires specific calibration of several tuning parameters. As shown in Figure 2.6, in our system, the final shape of the actuator is determined by the distribution of pre-elastomers along internal surface of the mold. Gravitational force, drag and normal force from the mold wall, as well as the rheological properties of materials determine motion of pre-elastomers. For each volume element of the pre-elasotmers, the above three forces

change over time with the rotation of the molds about two axes. Thus, besides the noticeable effect from the internal geometry, axial speed ratio is another important factor in affecting the final actuator homogeneity as it determines the spatial location of mold elements.

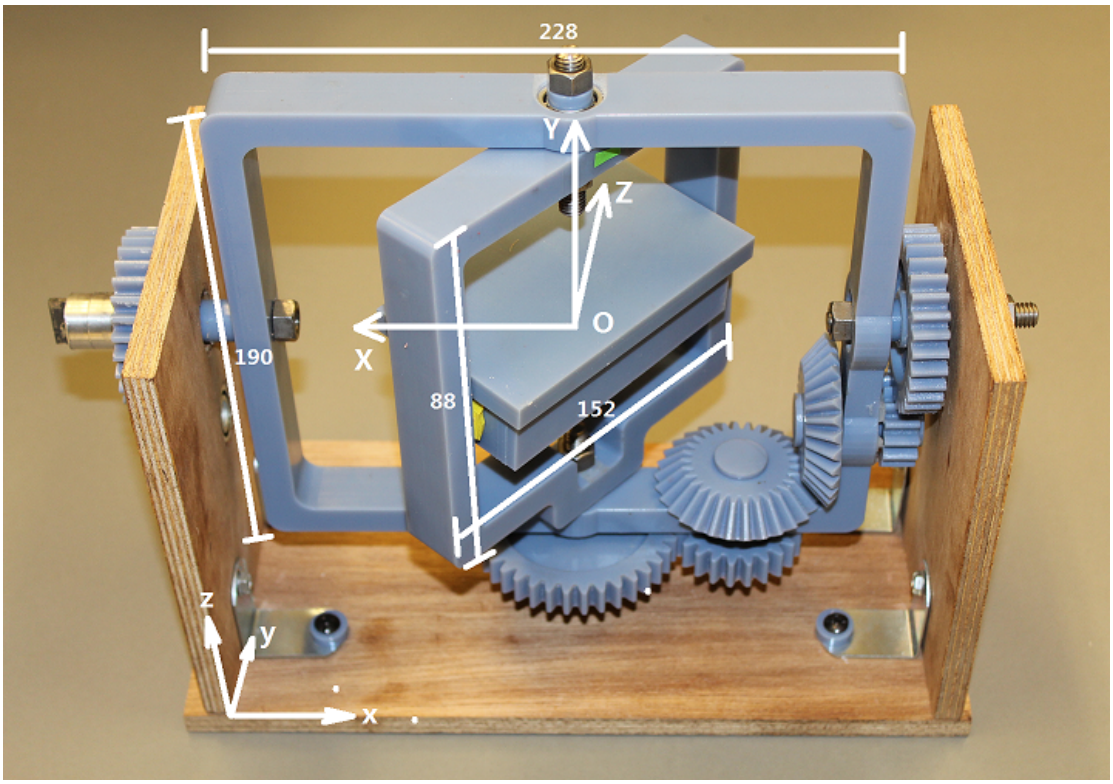

Figure 2.7 Rotational casting machine with dimensions (in the unit of mm) and coordinate systems.

It is difficult to consider all parameters simultaneously, unless numerical simulation is conducted. In this section, I will separately discuss more about each parameter that was computed or designed to produce the soft actuators presented earlier in this chapter. Tuning the parameters required the following: a proper axial speed ratio (Section 2.6.1), a model to relate rotational speed and actuator dimensions with viscosity (Section 2.6.2), the dependence of viscosity and ultimate strength of

elastomers on thinner percentage (Section 2.6.3), and mold geometries (Section 2.6.4). All data was produced using the 3D printed rotational casting machine in Figure 2.7. At the end of this section, we briefly show the procedures of the tip force tests and EMG-triggering experiment discussed in Section 2.4.3. The digital CAD files of 3D printed parts for building up the rotational machine can be found at: https://www.dropbox.com/sh/yf0fsf018gf9wmj/AADIrkANUyYPxpwBB0-TTr31a?dl=0.

2.6.1 Axial speed ratio design

The rotational casting machine is made up of two rotating frames: the outer one rotating about the X-axis driven by a motor and the inner one about the Y-axis driven by a bevel gear transmission. To exclude the effect of mold geometry and only consider the effect of axial speed ratio, we used a spherical mold (see Figure 2.17) for the design. The curvature of every point on the internal surface is equivalent for a spherical mold. A good axial speed ratio must satisfy: (1) avoid adding inhomogeneity for mold motion; (2) allow short periods for fast distribution of pre-elastomers.

There are two sets of coordinate systems shown in Figure 2.7: the XYZ coordinate, which is relative to the outer frame, and the global xyz-coordinate, which is fixed to the ground. Molds were fixed on the inner frame. We defined the axial speed ratio for the inner frame as following:

$$r = \frac{N_1}{N_2} = \frac{\omega_Y}{\omega_X} \qquad \text{(Equation 2.3)}$$

where N_1 and N_2 are coprime integers and ω_X and ω_Y are the rotating speed about X-axis and Y-axis.

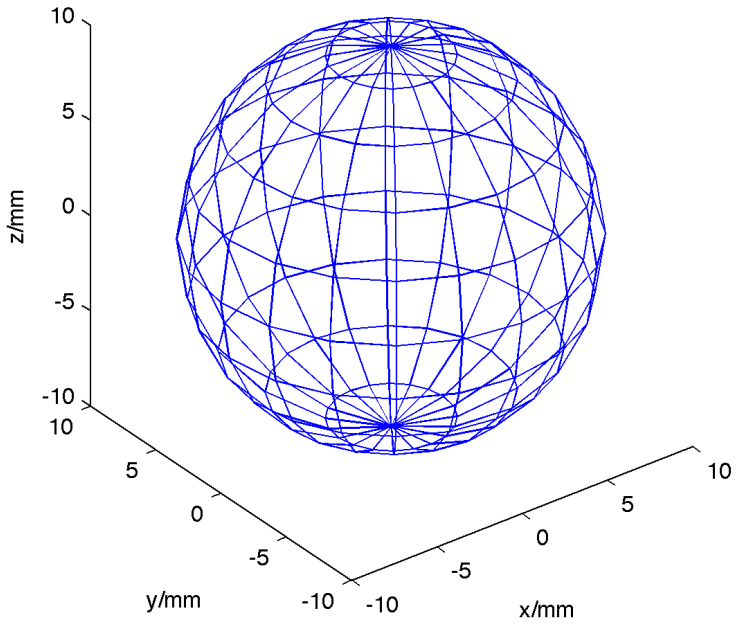

Figure 2.8 Grid on a spherical surface. Intersection points are points being simulated.

We simulated (using Matlab®) the rotation of the spherical mold using different axial speed ratios to understand how they would affect coating uniformity. Besides simulating the trajectories of certain points as shown in Figure 2.2, we chose 182 points distributed on the sphere surface (no point was greater than 3mm in separation) as shown in Figure 2.8.

Each point was rotated just as it would be on the rotational casting machine. Their z position was tracked at different axial ratios because only z position is distinguishable with respect to the three driving forces for rotational casting (gravity, drag and normal force). The data for the each chosen point was plotted into a probability density

functions (PDF, set at 1 mm intervals). PDFs for 182 points were plotted into one figure to see how different axial speed ratios affected mold motions (Figure 2.9). The ideal speed ratio would have produced identical density distribution for each point chosen after rotating for a complete period, yet we found no such speed ratio. We found the least common multiple (LCM) of N_1 and N_2 is a critical factor: the larger the LCM is, the fewer the number of PDFs and the more homogenous the coating.

The number limit we found for PDFs was six. Further analysis shows that the six different PDFs come from different initial Z-positions. Although the biaxial rotational casting machine could not produce identical motions for every point on the mold, we believe that a triaxial rotational casting machine could. For our purpose these PDFs were acceptable because they are symmetric, relatively flat, and identical for points with the same initial Z positions, thus we can simply manipulate the initial position of the mold to satisfy the homogeneity requirement of high priority.

Considering the second criterion, shorter period, we want small values for N_1 and N_2. Given the tradeoffs between large LCM and small values for N_1 and N_2, we chose r with a smaller LCM as long as the PDF number is close to six. For example, 46/37 is a better choice than 55/46. Also, r should be neither close to 1 nor too large. For example, if r = 101:100, when the mold completes one rotation about the Y-axis, it completes 101/100 rotations about the X-axis. The two axes have a 1/100-rotation difference, and it takes 100 rotations about the Y-axis to complete a full period. However, for r = 5:4, a complete period spans only 5 rotations about the Y-axis. If we choose r close to 5:4, we can complete roughly a full period every 5 rotations about the

Y-axis. Thus we chose numbers close to 3/2, 4/3, and 5/4, but with larger LCM's. From the above selection criteria, we selected axial speed ratio as 46:37 (close to 5:4) to use in our experiments.

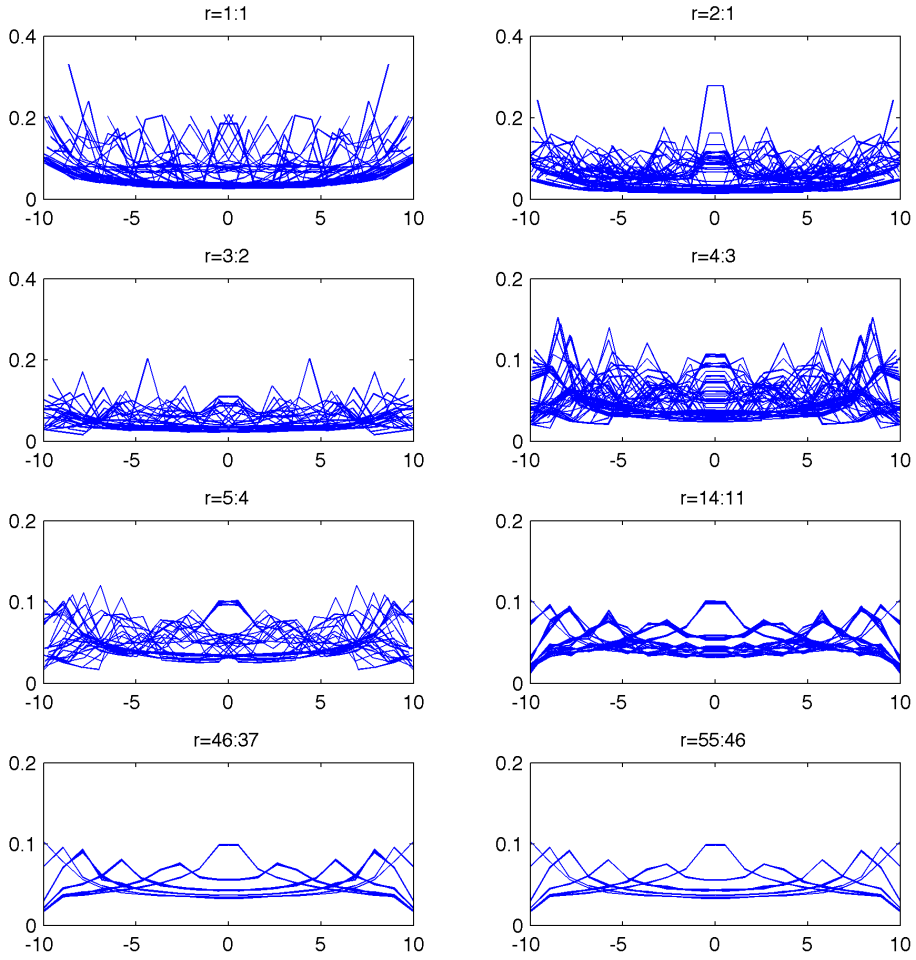

Figure 2.9 z-position PDFs for different axial speed ratios (x-axis in unit of mm)

For the above simulation, the mold is fixed at the center. Next we would prove that molds could be placed at any places of the machine. If we could prove this assumption, we could enlarge our machine and put a large number of molds in one run and reduce

the manufacturing time to realize mass production. In the following part, we will prove it theoretically.

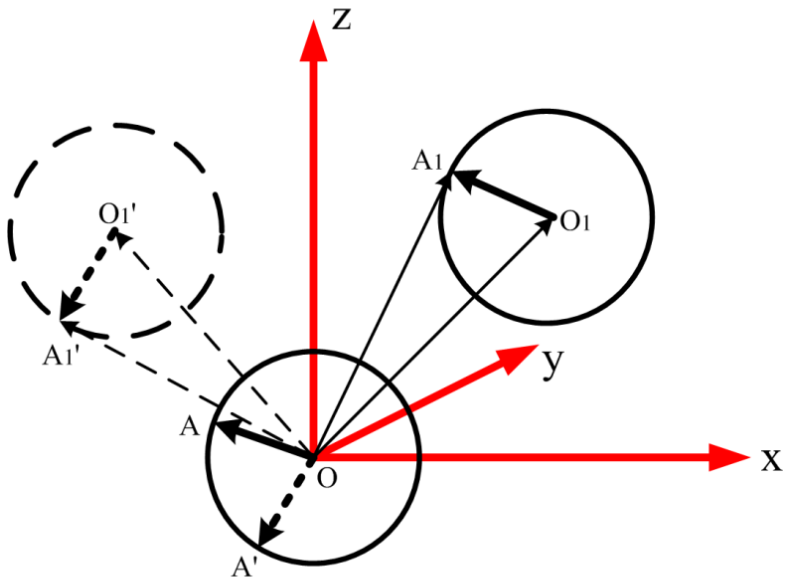

Figure 2.10 Schematic of mold rotation about two axes, the dotted line indicates the positions after rotating

Assume a spherical mold whose center is fixed at the center of the coordinates O and another mold whose center is fixed at O_1. Pick a random point A on the mold centered at O and pick a point A_1 on the other mold which is of the same relative position to O_1 as A to O. Rotate two molds together, first about x-axis an angle of θ_x then about y-axis and angle of θ_y. We will prove that the relative position of A_1 to O_1 after rotation is the same as that of A to O.

Proof:

Let

$$R_x = \begin{bmatrix} 1 & 0 & 0 \\ 0 & cos\theta_x & -sin\theta_x \\ 0 & sin\theta_x & cos\theta_x \end{bmatrix} \quad \text{(Equation 2.4)}$$

$$R_y = \begin{bmatrix} cos\theta_y & 0 & -sin\theta_y \\ 0 & 1 & 0 \\ sin\theta_y & 0 & cos\theta_y \end{bmatrix} \quad \text{(Equation 2.5)}$$

So

$$\overrightarrow{OA'} = RyRx\overrightarrow{OA} \quad \text{(Equation 2.6)}$$

$$\overrightarrow{OO_1'} = RyRx\overrightarrow{OO_1} \quad \text{(Equation 2.7)}$$

$$\overrightarrow{OA_1'} = RyRx\overrightarrow{OA_1} \quad \text{(Equation 2.8)}$$

Then

$$\overrightarrow{O_1'A_1'} = RyRx(\overrightarrow{OA_1} - \overrightarrow{OO_1}) = RyRx\overrightarrow{O_1A_1} \quad \text{(Equation 2.9)}$$

Finally,

$$\overrightarrow{OA'} = \overrightarrow{O_1'A_1'} \quad \text{(Equation 2.10)}$$

The reason that we only care about relative position is that the driven forces of rotational casting are gravity, drag and normal force from the mold with no centrifugal force, for which only the relative positions of elements on the mold matter. Also, centrifugal forces are avoided by limiting the rotational speed.

2.6.2 Model to relate viscosity with rotational speed and actuator dimensions

We assume that a proper axial speed ratio is designed to ensure spatial homogeneity for mold motions and the same spherical mold is used to exclude the effect of mold geometry. In addition, the following assumptions are made to establish a simple model for analyzing the relationship for pre-elastomer properties, input speed and other factors: (1) the pre-elastomers are incompressible and isotropic Newtonian fluid with shear viscosity, η and density, ρ; (2) only laminar flow exists; (3) no slip between the pre-elastomer and the mold surface; (4) ignore unsteady acceleration and only consider the steady state.

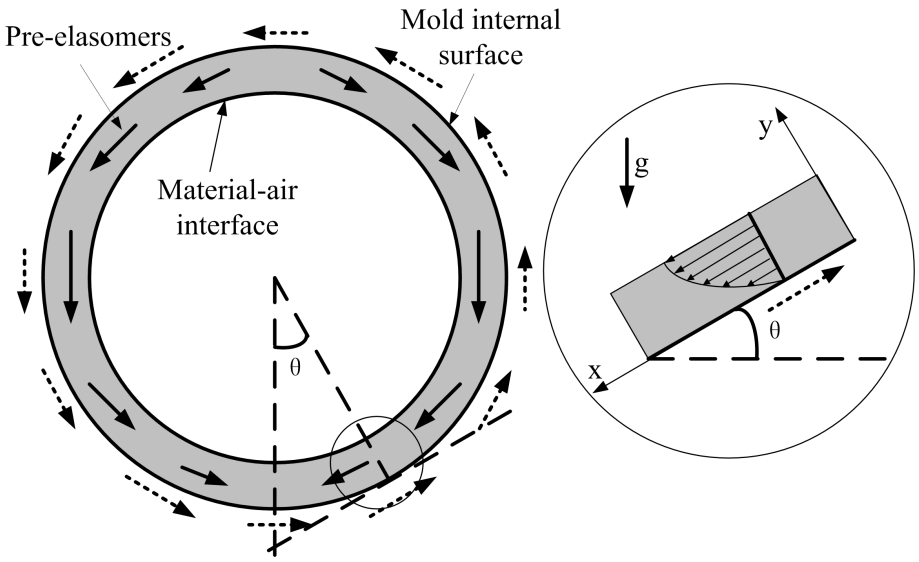

Figure 2.11 Cross-sectional profile of the spherical mold with pre-elastomers inside and an enlarged diagram of a locality with tangent plane of included angle θ with the ground; solid arrows indicate motions of pre-elastomers and dotted arrows indicate motions of mold elements

Under all the assumptions described above, the velocity field circled in Figure 2.11 can be described using Navier Stokes Equation as:

$$\eta \frac{\partial^2 u_x}{\partial y^2} + \rho g \sin\theta = 0 \qquad \text{(Equation 2.11)}$$

with boundary conditions as:

$$u_x(y = 0) = 0 \qquad \text{(Equation 2.12)}$$

$$\frac{\partial u_x}{\partial y}(y = h) = 0 \qquad \text{(Equation 2.13)}$$

where u_x is the velocity along x direction relative to mold, h is the thickness of the pre-elastomer at this point.

By solving the above equations with boundary conditions, we calculate:

$$u_x = -\frac{\rho g \sin\theta}{\eta}\left(\frac{1}{2}y^2 - hy\right) \qquad \text{(Equation 2.14)}$$

Then we determine the average velocity with wall thickness h and plane angle θ using the following equation:

$$\overline{u_{h,\theta}} = \frac{\int_0^h u_x dy}{h} = \frac{\int_0^h -\frac{\rho g \sin\theta}{\eta}\left(\frac{1}{2}y^2 - hy\right)dy}{h} = \frac{1}{3}\frac{\rho g \sin\theta}{\eta}h^2$$

(Equation 2.15)

Finally, we calculate the average velocity of pre-elastomers of the whole sphere along the mold with an average thickness, $\bar{h}$, using the following equation:

$$\overline{u_{\bar{h}}} = \frac{\int_0^{\pi} \overline{u_{\bar{h},\theta}} \cdot 2\pi R \sin\theta \cdot R d\theta}{4\pi R^2} = \frac{\pi}{12}\frac{\rho g}{\eta}\bar{h}^2 \qquad \text{(Equation 2.16)}$$

Now we have related the motion of pre-elastomers with forces and its properties and thickness. Before we discuss the rationality and motivation of calculating the above average velocity, we first discuss about the mold's motion.

The mold rotates about X-axis at the speed of ω_X and about Y-axis at the speed of ω_Y, thus

$$\vec{\omega} = \omega_X \hat{I} + \omega_Y \hat{J} \qquad \text{(Equation 2.17)}$$

X-axis is fixed with $\hat{I} = \hat{\imath}$, but Y-axis is rotating with $\hat{J} = cos\varphi\hat{\jmath} + sin\varphi\hat{k}$, where φ is the angle between Y-axis and y-axis, thus

$$\vec{\omega} = \omega_X \hat{\imath} + \omega_Y \cos\varphi\, \hat{\jmath} + \omega_Y \sin\varphi\, \hat{k} \qquad \text{(Equation 2.18)}$$

We ignore the rotation about the z-axis and only consider the rotations in the vertical direction, thus

$$|\vec{\omega}| = |\omega_X \hat{\imath} + \omega_Y \cos\varphi\, \hat{\jmath}| = \sqrt{\omega_X^2 + \omega_Y^2 \cos^2\varphi} \qquad \text{(Equation 2.19)}$$

For a fixed axial speed ratio r,

$$|\vec{\omega}| = \omega_X \sqrt{1 + r^2 \cos^2\varphi} \qquad \text{(Equation 2.20)}$$

So the mold could be seen as rotating about a horizontal axis with a speed $\omega_X\sqrt{1 + r^2 \cos^2\alpha}$. Half the sphere is rotating up and the other half is rotating down. For the half sphere rotating up, the radius of gyration can be calculated as:

$$\bar{R} = \frac{\int_0^{\pi/2} (R \sin\theta)(2\pi R \cos\theta) R d\theta}{2\pi R^2} = \frac{R}{2} \qquad \text{(Equation 2.21)}$$

So is the radius of gyration for the other half sphere that is rotating down. Now we could estimate the average velocity of points on the mold:

$$\overline{v_{up,\alpha}} = \overline{v_{down,\alpha}} = |\vec{\omega}| \cdot \bar{R} = \frac{\omega_X R}{2} \sqrt{1 + r^2 \cos^2\varphi} \qquad \text{(Equation 2.22)}$$

where φ changes with time linearly, so we could calculate the time-average velocity by integrating $|\vec{\omega}|$ with φ. Define $f(r) = \frac{\int_0^{2\pi} \sqrt{1+r^2\cos^2\varphi}\, d\varphi}{2\pi}$, thus

$$\overline{v_{up}} = \overline{v_{down}} = \frac{\omega_X R}{2} f(r) \qquad \text{(Equation 2.23)}$$

Now we relate the mold velocity with input rotational speed, dimension of the mold and speed ratio. Next, we relate mold motion with pre-elastomer's motion.

In the low viscosity regime (b), η is small, so based on Equation 2.16, $\overline{u_{\bar{h}}}$ is large. More specifically,

$$\overline{u_{\bar{h}}} > \overline{v_{up}} \qquad \text{(Equation 2.24)}$$

Notice that $\overline{u_{\bar{h}}}$ is the average velocity relative to mold, thus the direction of absolute velocity of pre-elastomers is downward. In a macro view, pre-elastomers flow to the very bottom of the mold. When the following condition is satisfied:

$$\overline{u_{\bar{h}}} = \overline{v_{up}} \qquad \text{(Equation 2.25)}$$

pre-elastomers start to stick the mold and have a tendency to climb up. From the above equation, we can estimate η_c as Equation 2.1.

As η increase, pre-elastomers lie in the coating regime and satisfy:

$$\overline{u_{\bar{h}}} < \overline{v_{up}} \qquad \text{(Equation 2.26)}$$

however, when

$$\overline{u_{\bar{h}}} << \overline{v_{up}} \qquad \text{(Equation 2.27)}$$

pre-elastomers stick completely with the mold and enter the high viscosity regime. The threshold η_h could be estimated from the following semi-empirical relation:

$$\overline{u_{\bar{h}}} = 0.05 \cdot \overline{v_{up}} \qquad \text{(Equation 2.28)}$$

The above equation shows we choose the threshold viscosity when the speed of the liquid only achieves 5% (α in the Equation 2.2) of the mold speed. The reason that we are using "average" velocity is: (1) velocity differs from point to point for both the mold and the pre-elastomer and they follow different rules of changing, so it is extremely difficult to get an analytical model for the whole system; (2) we used these equations to estimate the threshold viscosities and analyze how they are dependent on other parameters, in that case, a rough average estimate is enough and easy to implement.

In the next part, we will calculate the two threshold viscosities using Equation 2.25 and 2.28 and compare with data from experiments. The values for parameters are: $\rho = 1000\ \mathrm{kg/m^2}$, $g = 10\ \mathrm{m/s^2}$, $\omega_X = 6$ revs/min, $R = 10$ mm, $\bar{h} = 2$ mm, $r = \frac{47}{36}$.

From Equation 2.25:

$$\eta_c = \frac{\pi}{6}\frac{\rho g}{\omega_X R f(r)}\bar{h}^2 = 2.6\ \mathrm{Pa \cdot s} \qquad \text{(Equation 2.29)}$$

From Equation 2.28:

$$\eta_h = \frac{20\pi}{6}\frac{\rho g}{\omega_X R f(r)}\bar{h}^2 = 52\ \mathrm{Pa \cdot s} \qquad \text{(Equation 2.30)}$$

From Equation 2.25 and 2.28, we also see that ρ and $\bar{h}$ increase required η_c and η_h while ω_X, R and r decrease them when increase.

Then we directly tested η_c and η_h. We choose a set speed (6 revs/min) and began changing the viscosity to observe the motion of the pre-elastomers at different viscosities. For visualization we fabricated a mold (mold dimensions are the same as the spherical mold shown in Figure 2.17) using the transparent rubber VytaFlex 20 (from Smooth-On. Inc). We loaded Ecoflex 0030 precursors of different viscosities into the transparent mold and Figure 2.12 shows the screenshots at different times of five viscosities.

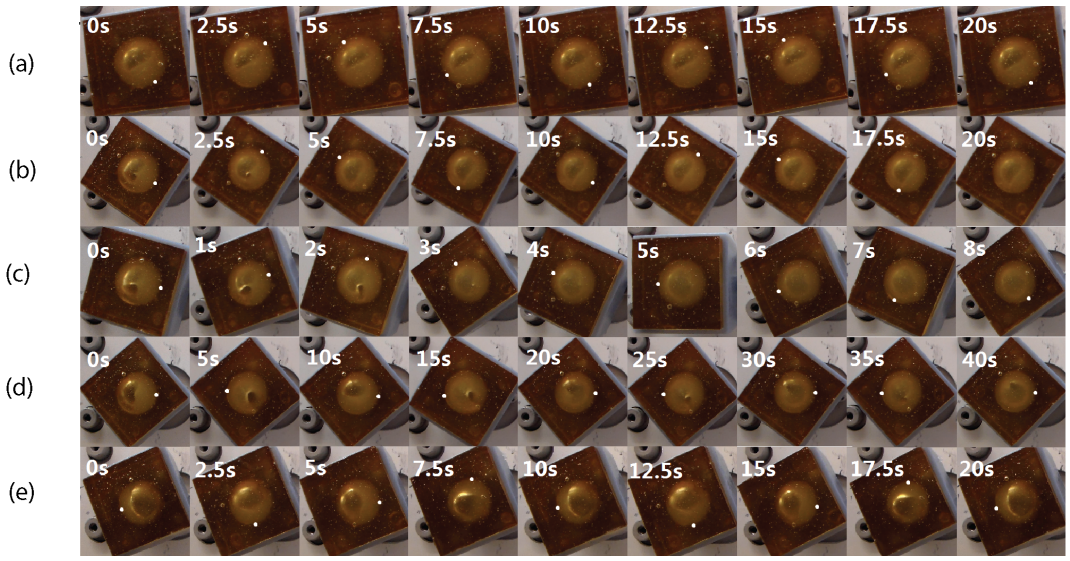

Figure 2.12 Pre-elastomer motions of five viscosities at different time intervals: (a) $\eta \sim 5$ Pa · s; (b) $\eta \sim 8$ Pa · s; (c) $\eta \sim 12$ Pa · s; (d) $\eta \sim 34$ Pa · s; (e) $\eta \sim 61$ Pa · s.

We observed the motions of pre-elastomers and tested the viscosity of pre-elastomer when it just start to stick to mold and when it ended moving relative to mold: $\eta_c \sim 7.1$ Pa · s and $\eta_h \sim 42$ Pa · s.

Comparing the experimental results with the calculated ones, we found that is close yet the experimental η_c is larger than the calculated one. At the start of the coating regime of Figure 2.1(b), pre-elastomers are still at the very bottom of the mold, the average thickness is larger than when they are distributed along complete internal surface, so $\bar{h}$ should be modified. For example, by substituting $\bar{h} = 4$ mm, we get $\eta_c = 10.4$ Pa · s.

2.6.3 Reducing viscosity by adding thinners to silicone

A necessary requirement for the pre-elastomers of rotational casting is:

$$\eta_0 < \eta_c \qquad \text{(Equation 2.31)}$$

Thus for pre-elastomers with high initial viscosity, thinners were used to reduce η_0. We added Silicone Thinner (ST, from Smooth-On, Inc.) to the silicone rubbers (including Ecoflex 0050, ELASTOSIL M4601 a/b and ELASTOSIL M4600 a/b) to reduce the viscosity of their pre-elastomers for rotational casting. Figure 2.13 shows the dependence of initial viscosity on ST percentage.

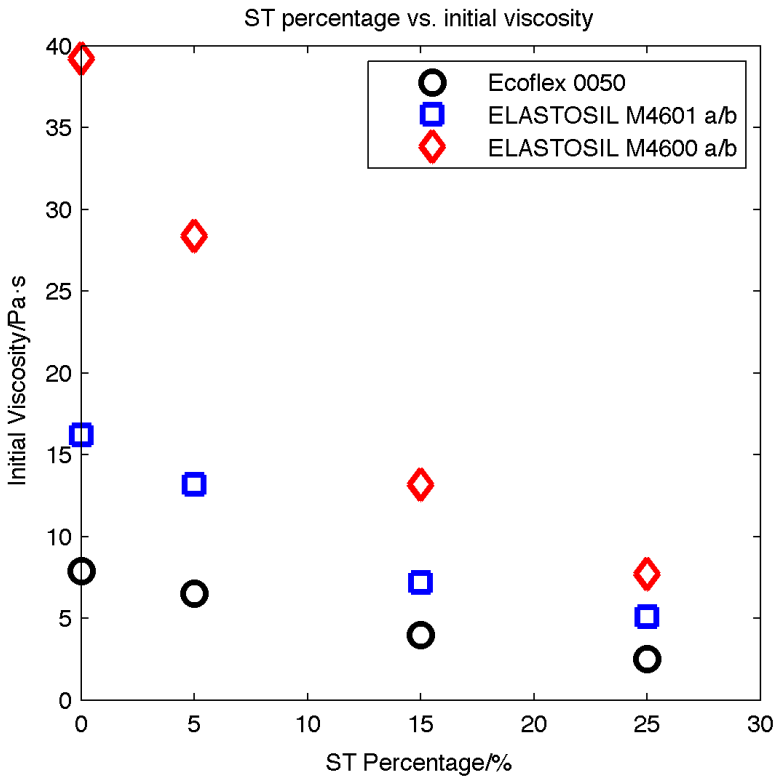

Figure 2.13 Thinner percentage vs. initial viscosity

Adding thinners also affected the mechanical properties of the cured elastomers, especially the strength and elasticity. Figure 2.14(a-c) show the dependence of ultimate strength, ultimate elongation and 100% modulus on ST percentage, respectively. The dependence of ultimate strength on ST percentage is unidirectional: increasing ST percentage decreases ultimate strength. For example, by adding 25% of ST, the

ultimate strength of ELASTOSIL M4600 a/b drops by 50% from 4 MPa to 2 MPa. Yet the dependence of ultimate elongation on ST percentage is ambiguous. For example, ELASTOSIL M4600 a/b reached its maximum ultimate elongation at the ST percentage of 25%. Ultimate elongation also decreases with the adding of ST.

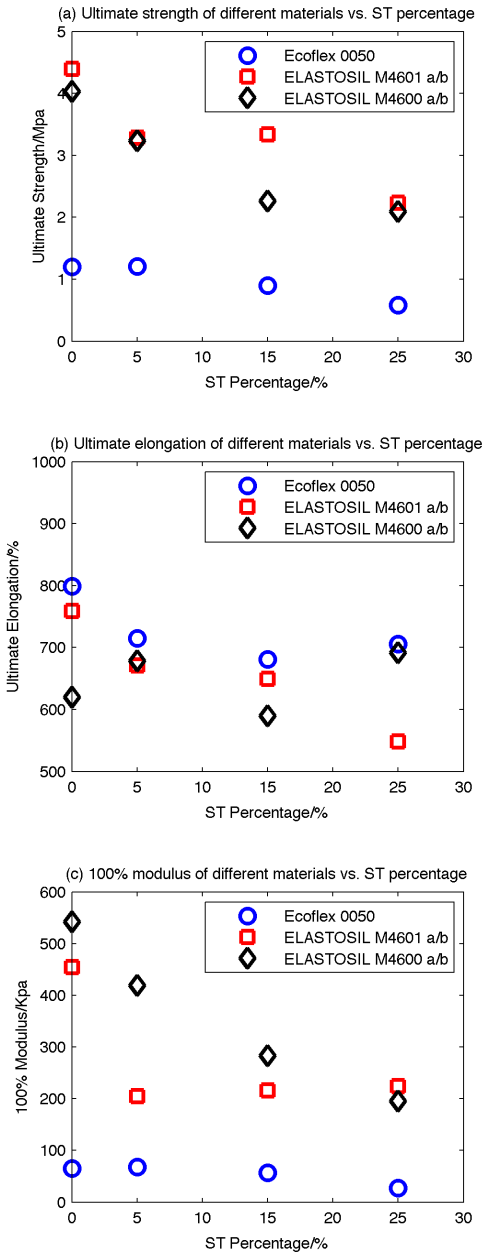

Figure 2.14 Tensile tests results of materials with different percentages of ST

In conclusion, adding ST decreases the ultimate strength, affects ultimate elongation and makes the material softer by decreasing its tensile modulus. In order to gain the required initial viscosity of the pre-elastomers, we sacrificed partial strength and elasticity of the cured elastomers. We also tested the ultimate strength by adhering two pieces of ELASTOSIL M4601 a/b together. The sample broke at the adhesive location and gave us an ultimate strength of 2.6 MPa. However, if we add 25% of ST into M4601 a/b, the ultimate strength dropped down to 2.3 MPa, which is lower than the adhesive strength (donated by σ_a). Thus another criterion for choosing the ST percentage besides Equation 2.31 is:

$$\sigma_s > \sigma_a \qquad \text{(Equation 2.32)}$$

where σ_s is the ultimate strength of the elastomer adding thinners.

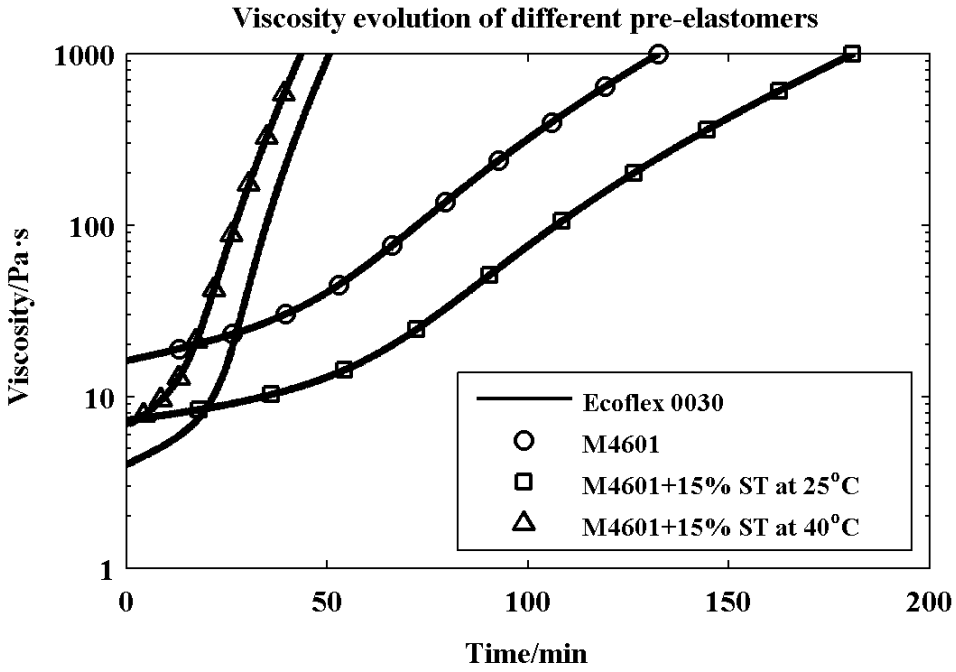

Figure 2.15 Viscosity evolution of different materials

For the above reasons we looked for a ST percentage to balance between the initial viscosity and the ultimate strength. We chose ELASTOSIL M4601 a/b and added 15% of ST to make cuboid actuator and the finger actuator. Figure 2.15 shows the viscosity evolution of Ecoflex 0030, M4601 a/b and M4601 a/b with 15% ST at different temperatures.

2.6.4 Mold dimensions

We used two types of molds in our paper: (1) molds for rotational casting; (2) molds for encapsulation. Figure 2.16 shows the three molds for rotational casting: mold for spherical actuator, mold for cuboid actuator (the same one as Figure 2.3(b)) and mold for finger actuator. They are all assembled from several 3D printed parts into a hollow piece with one connected cavity. Figure 2.17, 2.18 and 2.19 show dimensions and the cross-sectional views for the three molds.

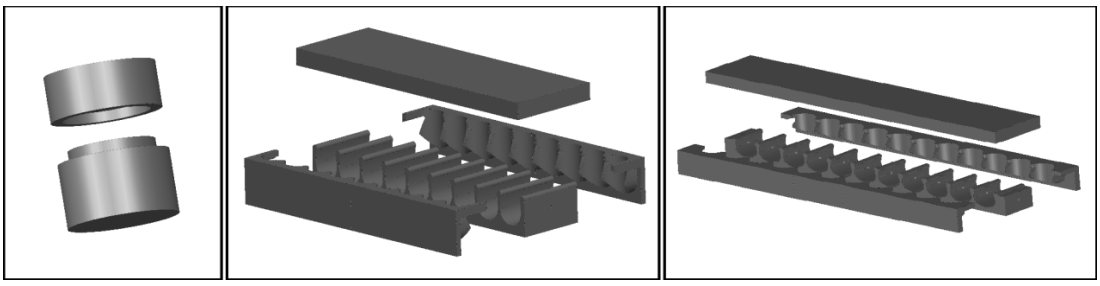

Figure 2.16 Explode views of mold assemblies for spherical actuator (left), cuboid actuator (middle) and finger actuator (right).

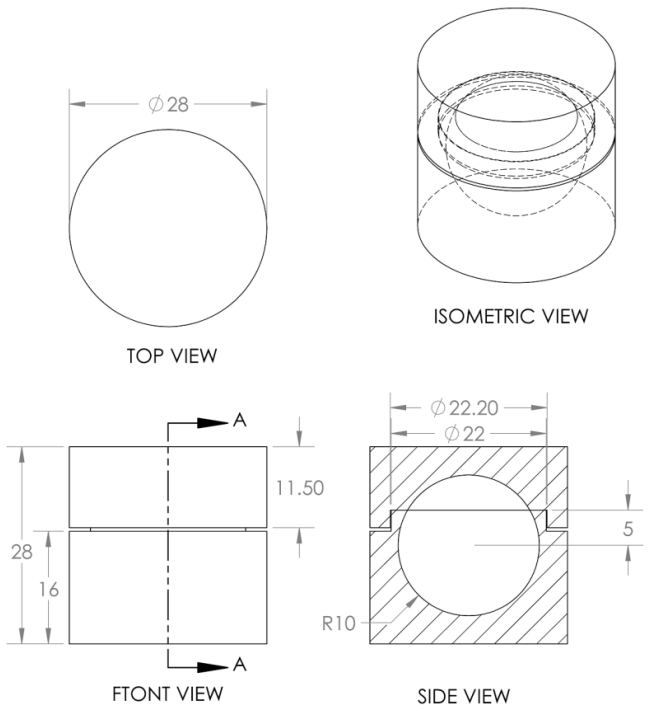

Figure 2.17 Orthogonal views of mold assembly for spherical actuator

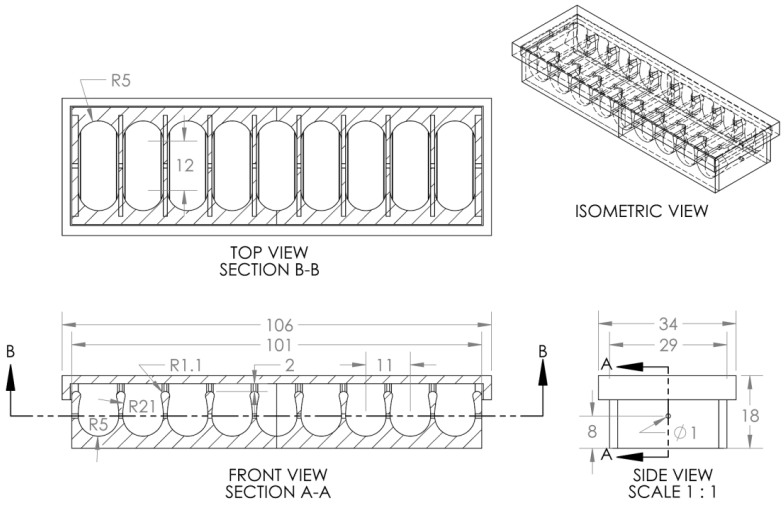

Figure 2.18 Orthogonal views of mold assembly for cuboid actuator

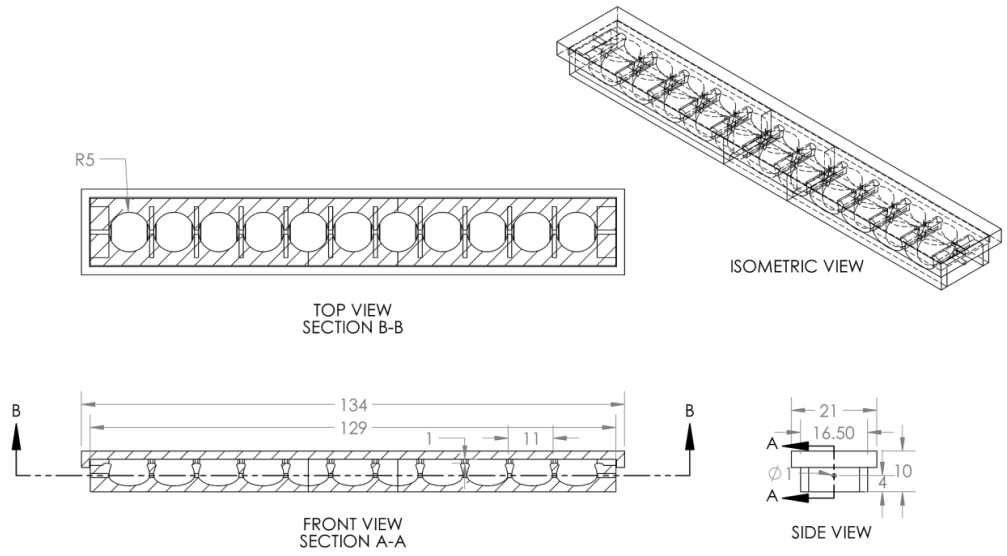

Figure 2.19 Orthogonal views of mold assembly for finger actuator

Note that dimensions for curves in the front view in Figure 2.19 are not given because the curves were not designed as circular arc; instead, they were designed by reducing the height of the design of the cuboid actuator (see Figure 2.18 in the front view by half.

The second kind of molds used in the paper are the molds for encapsulation, which include one to encapsulate the rotational casted actuator from mold in Figure 2.18 to form a cuboid actuator (see Figure 2.20) and the other to encapsulate the rotational casted actuator from mold in Figure 2.19 to form a finger actuator (see Figure 2.21).

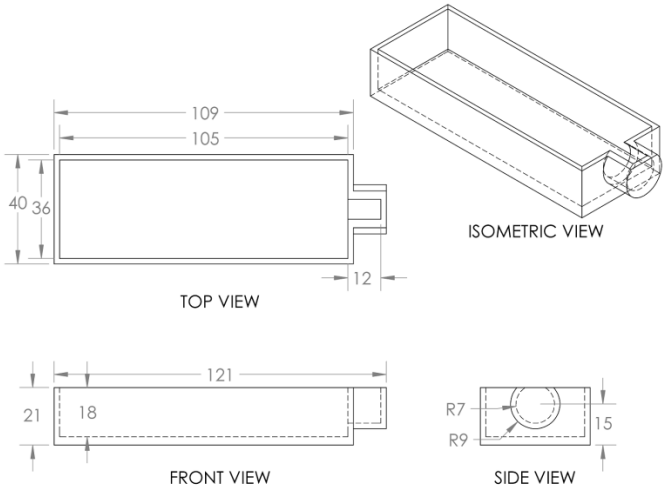

Figure 2.20 Orthogonal views of mold for encapsulation for a cuboid actuator

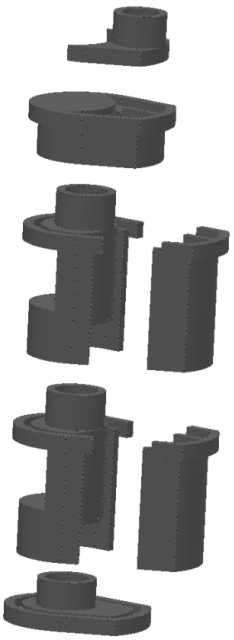

Figure 2.21 Exploded view of mold for capsulation for a finger actuator

As shown in Figure 2.21, the mold for encapsulation for a finger actuator is designed in seven interlocking 3D-printed parts to facilitate disassembly and removal of the

monolithic elastomer actuator after curing. A fit tolerance of 0.25 mm creates tight interlocking to prevent leakage while allowing for ease of assembly. Two mold segments (each composed of two pieces to facilitate mold removal) are stacked on top of each other and a base piece to form the primary structure of the actuator and the finger bands, while an upper extension segment creates a solid column for a hose clamp. A 9.0 mm central cavity accommodates the separately rotational casted interior actuator (with mold shown in Figure 2.19), which will be pneumatically inflated. The 3D printing design process allows for the mold to be easily customized with negligible change in manufacturing time. The important dimensions of the mold assembly are shown in Figure 2.22.

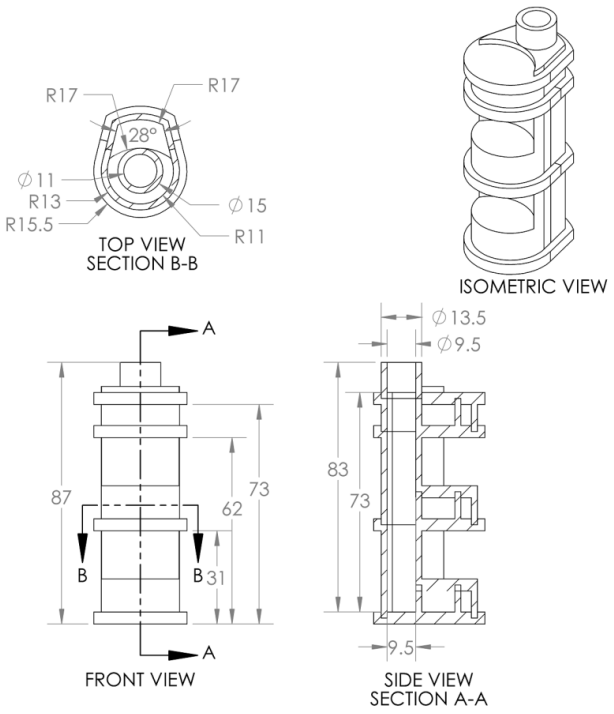

Figure 2.22 Orthogonal views of mold for encapsulation for finger actuator

2.6.5 Force test and EMG triggering experiment

Our force test set up is shown in Figure 2.4(b): (i) we placed the actuator on flat surface, with a force sensor under one of the tips; (ii) then we put a bezel over the top of it to constrain its height when actuated; (iii) we chose a height corresponding to a curvature and fixed the position, then increased pressures and recorded applied forces. Figure 2.4(c) shows the tip force vs. pressure relationship of actuators with two different curvatures. The two specimens had the same dimensions (105mm×36mm×18mm) but were manufactured at different times.

The EMG triggering experiment includes two steps: (1) collect muscle signal from user by attaching the EMG electrodes on their forearm and deliver the signal to Arduino; (2) use the signal collected from step 1 to open/close two solenoid valves, with one valve inflating the actuator and the other deflating it. We decided the threshold muscle potential from trials of the user. A video showing a user pick up a 2-kg weight with finger exo on the index is shown in Video 2.1.

REFERENCES

[1] F. Ilievski, A. D. Mazzeo, R. F. Shepherd, X. Chen, G. M. Whitesides, Soft robotics for chemists. *Angew. Chem.* **123**, 1930-1935 (2011).

[2] K. Suzumori, Elastic materials producing compliant robots. *Rob. Auton. Syst.* **18**, 135–140 (1996).

[3] S. Wakimoto, K. Wakimoto, K. Suzumori, Y. Nishioka, Miniature soft hand with curling rubber pneumatic actuators. *in proceeding of 2009 IEEE International Conference on Robotics and Automation*, 12 to 17 May 2009, Kobe, Japan, pp. 556-561.

[4] R. F. Shepherd, F. Ilievski, W. Choi, S. a. Morin, A. A. Stokes, A. D. Mazzeo, X. Chen, M. Wang, and G. M. Whitesides, Multigait soft robot. *Proc. Natl. Acad. Sci. U. S. A.* **108**, 20400–20403 (2011).

[5] H. T. Lin, G. G. Leisk, and B. Trimmer, GoQBot: a caterpillar-inspired soft-bodied rolling robot. *Bioinspir. Biomim.* **6**, 26007 (2011).

[6] C. Laschi, M. Cianchetti, B. Mazzolai, L. Margheri, M. Follador, and P. Dario, Soft Robot Arm Inspired by the Octopus. *Adv. Robot.* **26**, 709–727 (2012).

[7] A. D. Marchese, C. D. Onal, and D. Rus, Autonomous Soft Robotic Fish Capable of Escape Maneuvers Using Fluidic Elastomer Actuators. *Soft Robot.* **1**, 75–87 (2014).

[8] M. R. Cutkosky and S. Kim, Design and fabrication of multi-material structures for bioinspired robots, *Philos. Trans. A. Math. Phys. Eng. Sci.* **367**,1799-1813 (2009).

[9] N. Correll, C. D. Onal, H. Liang, E. Schoenfeld, D. Rus, Soft autonomous materials—using active elasticity and embedded distributed computation, in *Experimental Robotics*, Springer Berlin Heidelberg, January, 2014, pp. 227-240.

[10] G. K. Klute, J. M. Czerniecki, B. Hannaford, McKibben artificial muscles: pneumatic actuators with biomechanical intelligence. *In Proceedings of 1999 IEEE/ASME International Conference on Advanced Intelligent Mechatronics*, 19 to 23 September 1999, Atlanta, USA, pp. 221-226.

[11] Y. Park, B. Chen, C. Majidi, R. J. Wood, R. Nagpal, E. Goldfield, Active modular elastomer sleeve for soft wearable assistance robots. *in Proceedings of 2012*

IEEE/RSJ International Conference on Intelligent Robots and Systems, 7 to 12 October 2012, Vilamoura, Portugal, pp. 1595–1602.

[12] P. Polygerinos, S. Lyne, Z. Wang, L. F. Nicolini, B. Mosadegh, G. M. Whitesides, C. J. Walsh, Towards a soft pneumatic glove for hand rehabilitation, *in Proceedings of 2013 IEEE/RSJ International Conference on Intelligent Robots and Systems*, 3 to 7 November 2013, Tokyo, Japan, pp. 1512–1517.

[13] E. T. Roche, R. Wohlfarth, J. T. Overvelde, N. V. Vasilyev, F. A. Pigula, D. J. Mooney, K. Bertoldi, C. J. Walsh, A bioinspired soft actuated material. *Adv. Mater.* **26**, 1200-1206 (2014).

[14] M. Sugisaka, H. Zhao, The characteristics of McKibben muscle based on the pneumatic experiment system. *Artificial Life and Robotics* **11**, 223-226 (2007).

[15] Festo, Fluidic Muscle Brochure, http://www.festo.com/net/SupportPortal/Files/340811/Fluidic%20Muscle%20DINA4_en.pdf, accessed: June, 2008.

[16] R. V. Martinez, J. L. Branch, C. R. Fish, L. Jin, R. F. Shepherd, R. Nunes, Z. Suo, G. M. Whitesides, Robotic Tentacles with Three-Dimensional Mobility Based on Flexible Elastomers. *Adv. Mater.* **25**, 205-212 (2013).

[17] R. V. Martinez, C. R. Fish, X. Chen, G. M. Whitesides, Elastomeric Origami: Programmable Paper-Elastomer Composites as Pneumatic Actuators. *Adv. Funct. Mater.* **22**, 1376-1384 (2012).

[18] S. A. Morin, Y. Shevchenko, J. Lessing, S. W. Kwok, R. F. Shepherd, A. A. Stokes, G. M. Whitesides, Using "Click-e-Bricks" to Make 3D Elastomeric Structures. *Adv. Mater.* **26**, 5991-5999 (2014).

[19] C. M. Schumacher, M. Loepfe, R. Fuhrer, R. N. Grass, W. J. Stark, 3D printed lost-wax casted soft silicone monoblocks enable heart-inspired pumping by internal combustion. *RSC Advances* **4**, 16039-16042 (2013).

[20] R. Deimel, O. Brock, A compliant hand based on a novel pneumatic actuator. in *Proceedings of the 2013 IEEE International Conference on Robotics and Automation*, 6 to 10 May 2013, Karlsruhe, Germany, pp. 2047–2053.

[21] M. T. Tolley, R. F. Shepherd, B. Mosadegh, K. C. Galloway, M. Wehner, M. Karpelson, R. J. Wood, and G. M. Whitesides, A Resilient, Untethered Soft Robot. *Soft Robot.* **1**, 213–223 (2014).

[22] R. F. Shepherd, A. A. Stokes, J. Freake, J. Barber, P. W. Snyder, A. D. Mazzeo, L. Cademartiri, S. A. Morin, G. M. Whitesides, Using explosions to power a soft robot. *Angew. Chem.* **125**, 2964-2968 (2013).

[23] W. P. Cox, E. H. Merz, Correlation of dynamic and steady flow viscosities. *J. Polym. Sci.* **28**, 619-622 (1958).

[24] R. J. Crawford, M. P. Kearns, Practical guide to rotational moulding (iSmithers Rapra Publishing, 2003).

[25] P. J. Flory, Constitution of three-dimensional polymers and the theory of gelation. *Rubber Chem. Technol.* **15**, 812-819 (1942).

CHAPTER 3

CURVATURE CONTROL OF SOFT ORTHOTICS VIA LOW COST SOLID-STATE OPTICS[†]

3.1 Introduction

Soft robotic systems composed of organic elastomers have an intrinsic compliance that has demonstrated its potential as wearable devices because of their conformability, safety, and comfort [1]. The intrinsic compliance stems from the material's low elastic modulus, which is comparable to bio-tissues [2]. Though intrinsically compliant actuators like McKibben Artificial Muscles [3, 4] have existed for decades, new designs of fluidically-powered elastomeric actuator (FEAs) [5, 6] have shown great potential as wearable orthotics.

Current hand orthotics under development usually serve two functions: (1) rehabilitation training [7, 8] or (2) assisting activities of daily living [9, 10, 11]. Both of these uses require safe, reliable, and predictable performance and feedback control systems. Despite increasing sophistication in the design and fabrication of FEAs [12], the sensing and control of these actuators are still nascent. A prime reason for the lag in control sophistication is the high nonlinearity of these systems and relatively specialized fabrication required for soft sensors. Though compliant and stretchable sensors have been developed for FEAs, open-loop control is still the most commonly

[†] H. Zhao, R. Huang, and R. F. Shepherd, Curvature Control of Soft Orthotics via Low Cost Solid-State Optics, in *Proc. IEEE Int. Conf. Robotics Automation*, Stockholm, Sweden, May 16-21, 2016, pp. 4008-4013.

used method for their operation. Many control systems require higher accuracy, repeatability and resolution than presently available [13, 14, 15]. Besides simple open loop control, some relevant control methods for FEAs include adaptive control, real-time finite element method and vision-based PID control. Adaptive control has been applied to McKibben Muscles [16], which is essentially a linear actuator, but not bending FEAs. Real-time finite element method [17] can give a good estimate of the actuator's behavior, but this method requires sufficient knowledge of the system to perform accurate simulations. Traditional proportional-integral-derivative (PID) feedback control based on computer vision has been applied to hydraulic FEAs and shown great results, yet this method requires external cameras that limit the potential mobility of the wearer [18, 19].

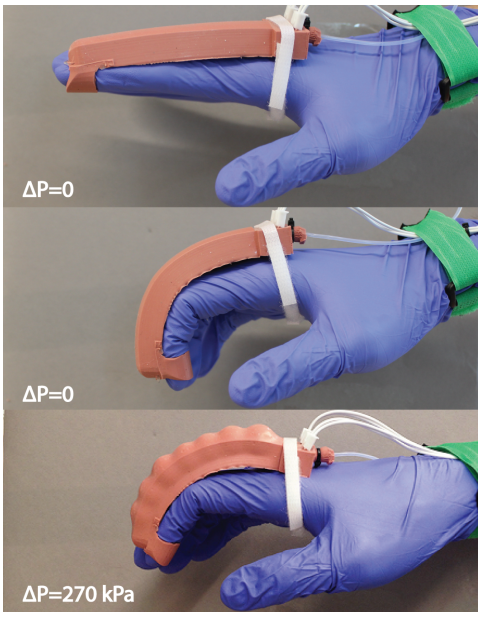

Figure 3.1 Optical fiber embedded orthotic unpowered (top), moving a finger while unpowered (middle) and actuating causing the finger to move while being pressurized (bottom).

In the previous chapter, I described a reliable and effective method for fabricating high force FEA-based orthotics using rotational casting [20]. To better improve the functionality of these actuators towards hand orthotics, this chapter demonstrates the monolithic integration of an optical light guide for curvature sensing. In addition to fabrication and integration, I have also developed a controller to maintain the curvature of FEAs. Specifically, I characterized the system's static and dynamic responses experimentally and developed a curvature control algorithm using gain-scheduled PID controller. We implemented the algorithm by adjusting the actuator's inflating pressure, which is generated from a compressed air source through a fast-responsive, pulse-width-modulation (PWM) controlled solenoid valve.

3.2 Design and Fabrication

3.2.1 Design

Talbe 3.1 Design paramertes of the finger Orthotic

Design parameters, units	Values
Length, mm	110
Effective length, mm	70
Range of motion, degrees	0-105
Pressure, kPa	0-270
Tip Force, N	0-5

The orthotic we designed (Figure 3.1) has the following features: (1) Low stiffness when deflated, which enables easy movement of the wearer's finger; (2) high force/torque generation; [20] (3) repeatable performance from its manufacturing technique (rotational casting); (4) integrated curvature sensor with high repeatability and resolution; (5) compatible bending range for finger motions. Table 3.1 summarizes the design parameter values of the finger exoskeleton.

3.2.2 Fabrication

The fabrication process for the orthotic with embedded curvature sensor includes three stages: (1) fabricate the internal actuator (Figure 3.2), (2) shape and pattern the sensor's light guide (Figure 3.3), and (3) assemble and cast into a complete orthotic (Figure 3.4).

3.2.2.1 Actuator fabrication

The internal actuator is a monolithic structure composed of a series of hollow chambers with nylon mesh incorporated in one side to program a bending mode of inflation. Figure 3.2 shows our custom-built rotational casting machine used to cast the seamless FEAs [20]. The material we used for the internal actuator is a blend of commercially available silicone rubbers (90% ELASTOSIL M 4601, 10% silicone thinner from Smooth On, Inc, by volume).

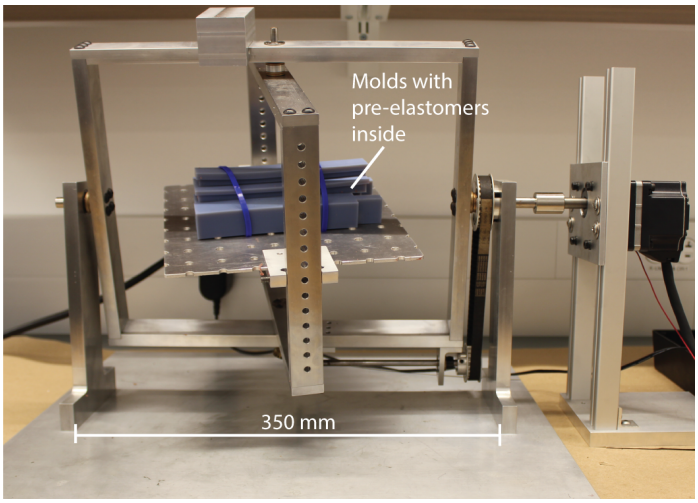

Figure 3.2 Custom-built rotational casting machine with multiple molds. Viscous pre-elastomers inside the mold flow against the internal walls coating them and forming a seamless actuator.

3.2.2.2 Curvature sensor fabrication

Optical fibers have been used previously for accurate sensing of bending [21, 22]. This system inputs light from an LED into an optical waveguide and a Photo-Darlington detector reads the output signal on the other side—increased bending causes lower light intensity from the waveguide and less current output from the photosensitive detector. To fabricate the waveguide, we bent a piece of 1-mm-diameter acrylic optical fiber into a U shape via thermoforming, and then we used a laser cutter (Zing 24 from Epilog) to roughen the optical fiber on one side (Figure 3.3). The anisotropic roughening enhances the signal change upon bending.

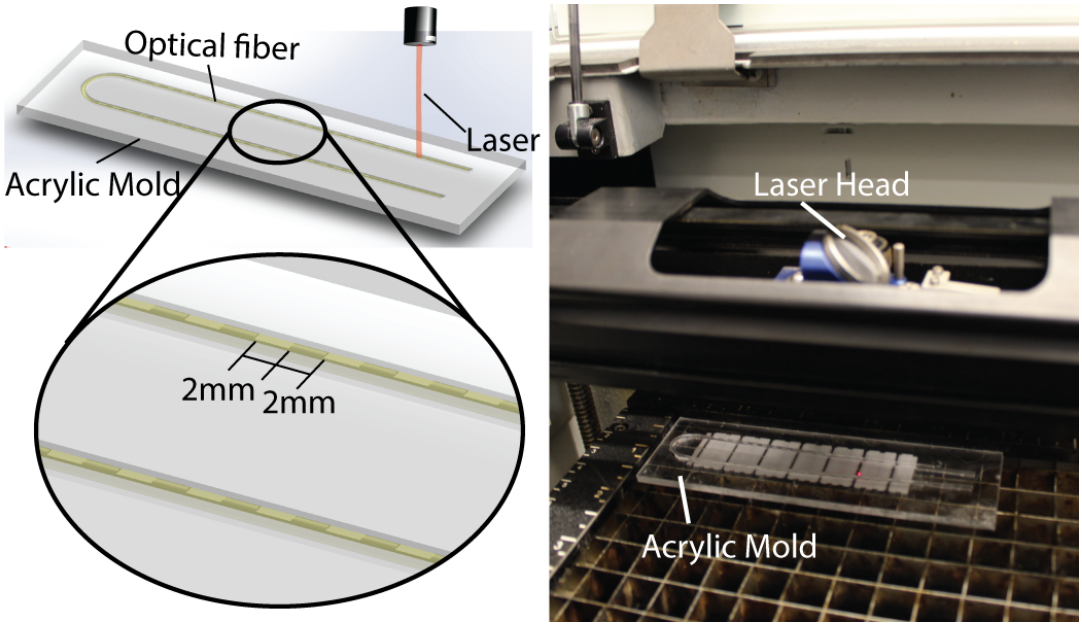

Figure 3.3 (left) U-shaped Optical fiber being roughened by a laser cutter. (right) a photo of the optical fiber being cut by a laser cutter.

Excessive roughening will cause the output light intensity to drop to zero; therefore, we engraved the optical fiber with 2 mm roughened lengths at intervals of 2 mm (Figure 3.3). The total engraving section is of the same length as the orthotic's

effective bending length. To avoid cracks from engraving causing fracture upon actuation, we oriented the fiber so it bends in the direction of closing the cracks. In this orientation, light intensity detected by the photo-Darlington increases with bending curvature.

3.2.2.3 Assembly and cast process

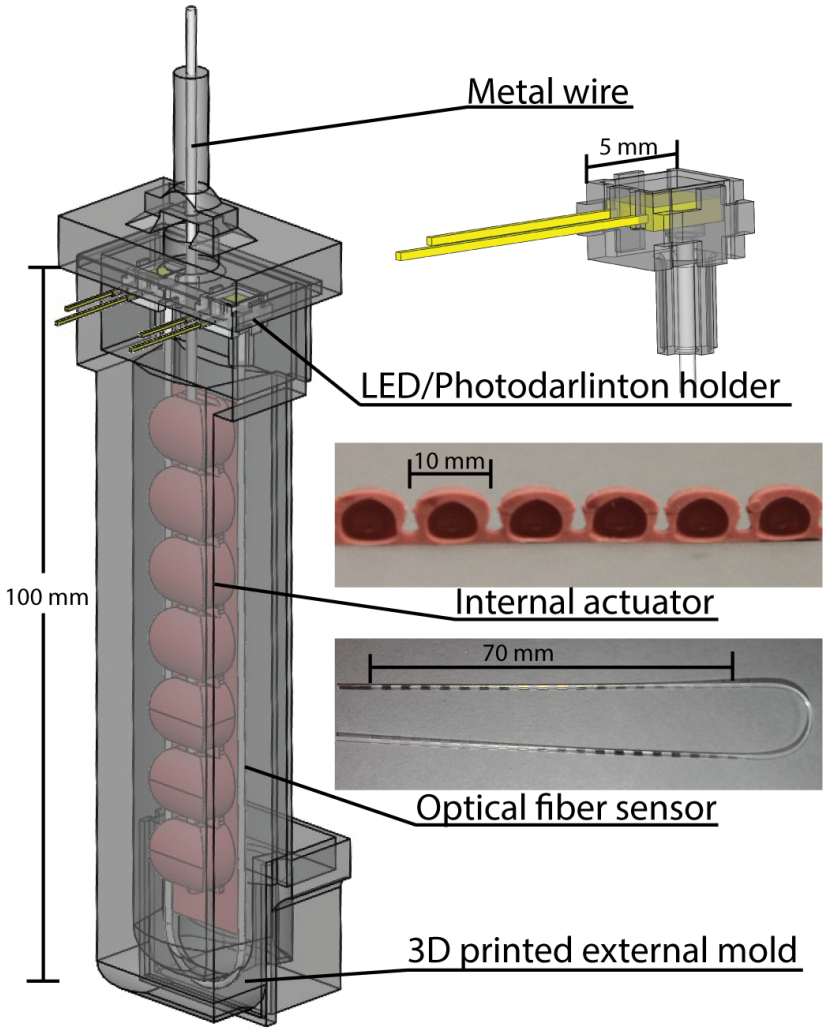

Figure 3.4 Assembly of parts cast into a single orthotic: optical fiber and LED/photo-Darlington was housed in the holders, and the holders were fixed on the mold through four pins.

To embed the sensor in the orthotic, we chose to cast the LED, photo-Darlington and the engraved optical fibers into the actuator. The peak wavelength of the LED and the sensitive wavelength of the photo-Darlington were both at the range of infrared light, which eliminated the interference of visible light. To ensure the best contact angle for the optical fiber, LED and photo-Darlington inside the actuator, we designed the housing shown in Figure 3.4. As the optical fiber is inextensible, we placed it close to the neutral bending plane of the actuator with the strain limiting fabric. We then poured silicone rubber pre-elastomer into the mold and cast them into a single piece. The resulting orthotic has the following features: 7 internal pneumatic chambers, nylon mesh fabric on one side, optical fiber curvature sensor close to the neutral plane, encapsulated LED and photo-Darlington, two pairs of exposed pins as electrical connections to the outer circuit, a rubber band for fixing onto the finger and a flat section for fixing onto the back of hand.

3.3 Experimental Setup

To characterize and control our orthotic system, we built a platform that is composed of a microcontroller board, an electrical relay and solenoid valve, a pressure sensor (PSE 530-R06 from SMC), a circuit for the optical fiber sensor, a constant-pressure air source, and power supply (Fig 3.5(a)).

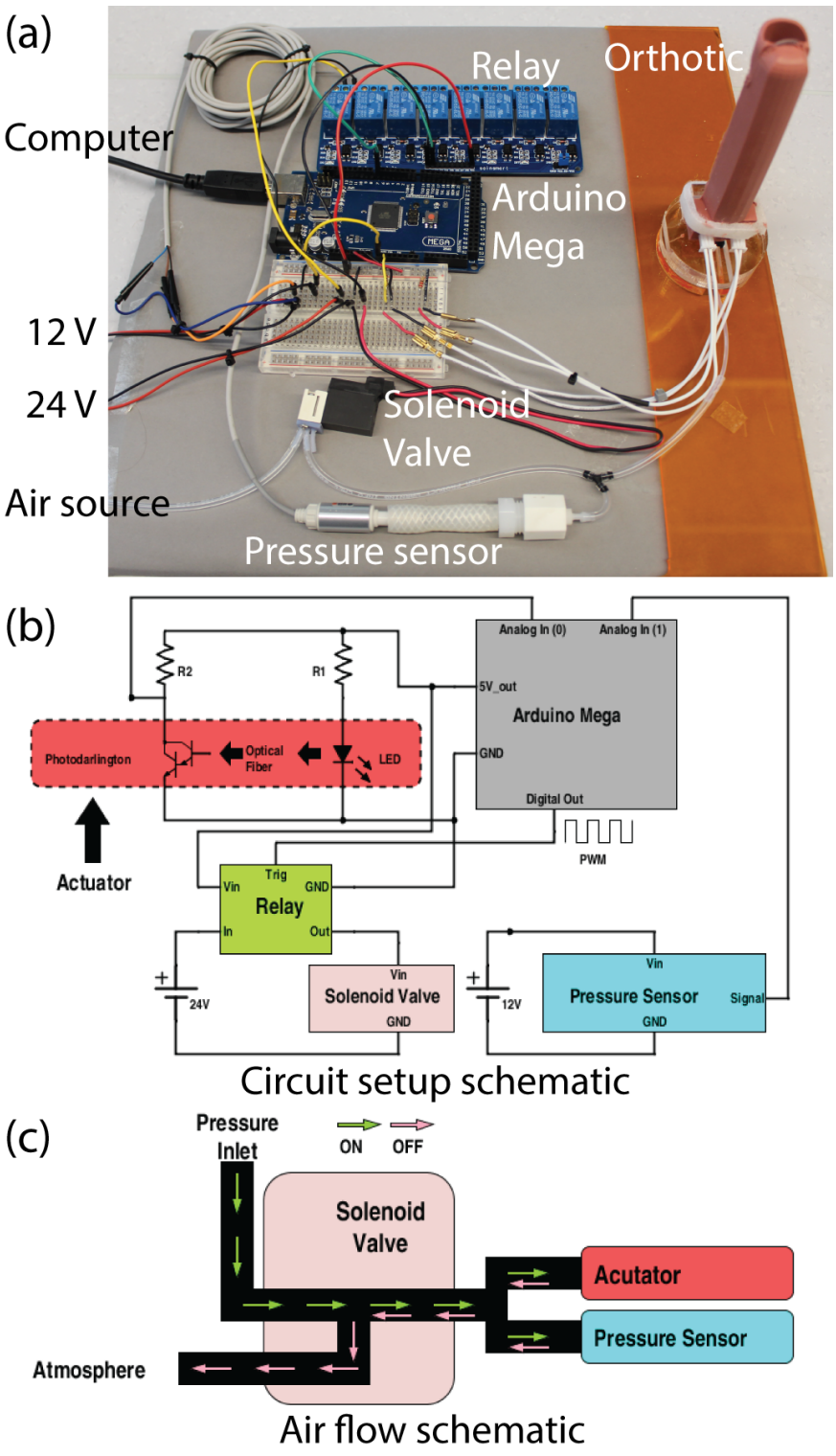

Figure 3.5 Testing platform for the orthotic: (a) a photo of the setup; (b) schematic of the circuit set up; (c) schematic of the air flow at both the on and off state for the solenoid valve.

The microcontroller we used is an ArduinoTM MEGA 2560 that collects analog data from the pressure and optical fiber sensors and implements the PID controller to output the Pulse Width Modulation (PWM) signals for valve control. The solenoid valve we chose was a VQ110U-5M from SMC Corporation. It is a large flow, normally closed, 3-port solenoid valve with a fast response time (On: 3.5 ms, off: 2 ms). The airflow schematic is shown in Figure 3.5(c). The relay we used was an SRD-05VDC-SL-C from Songle Relay with an operation time of 10 ms and release time of 5 ms. The response times of the solenoid valve and the relay are critical as they limit the PWM frequency we could use to control the open and close the valve. Using this relay and valve system, we chose 60 Hz as the PWM frequency. We chose acrylic optical fiber (CK-40, EskaTM, Inc.) and an 870 nm LED (IF E91D, Industrial Fiber Optics, Inc). The photo-Darlington detector (IF D93, EskaTM, Inc.) has a peak photosensitivity of 850 nm. To limit the current, we used resistances of 220 ohm (R1) and 100 ohm (R2) in the circuits of the LED and photo-Darlington, respectively (Figure 3.5(b)). This test platform can be easily extended to control multiple FEAs.

3.4 Results and Discussions

3.4.1 Calibration of the optical fiber sensor

Before conducting tests on the finger orthotic, we calibrated an optical fiber sensor embedded into elastomeric orthotic using a video camera and image processing. The curvatures ($1/r$) were achived through a high-resolution camera located facing the side of the orthotic and 7 points were picked on the neutral plane line to fit the orthotic

curvature into a circle. Despite a non-linear response (we fit it into a third-order polynomial as shown in Figure 3.6), the sensor exhibited very good properties in terms of resolution, accuracy, repeatability and curvature range. Additionally, the sensor also exhibits good dynamic properties (i.e., a very short response time of 5 ms). Table 3.2 summarizes the capabilities of our embedded curvature sensor.

Table 3.2 Optical fiber sensor parameters

Properties	Parameters, unit	Value
Sensitivity	Slope of current over curvature, mA/m^{-1}	0.3-3.8
Accuracy[a]	Relative error, %	5.4
Resolutiona	Minimum discriminated curvature, m^{-1}	0.04
Repeatabilitya, [b]	Curvature standard deviation, m^{-1}	0.05
Range	Curvature range, m^{-1}	0-26
Dynamic Propertiesc	Response time, ms	5

[a)] These are average values;
[b)] Based on three separate tests performed on the same optical fiber sensor;
[c)] These are not tested data but from the datasheets of commercial LED and photo-Darlington.

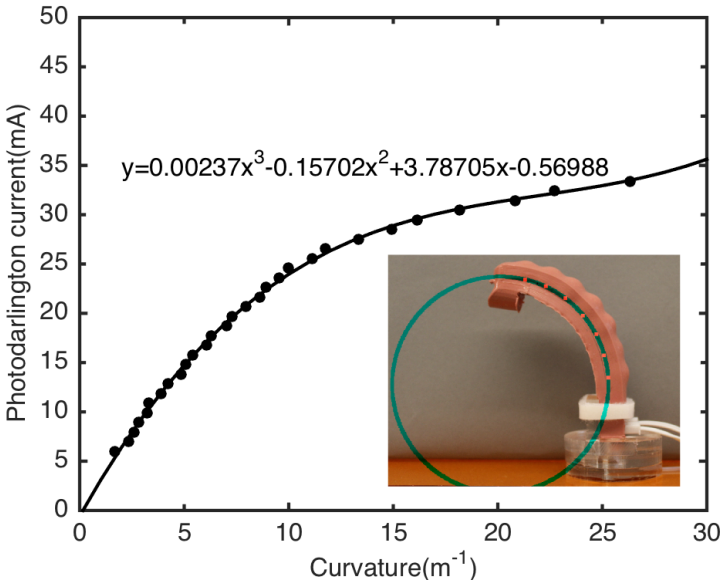

Figure 3.6 Calibration curve of the embedded optical sensor.

Note that the values we collected above were specific to the orthotic sensor. Some of the properties could be further improved to satisfy stricter requirements; for example, the range of the sensor could be extended to as large as 50 m^{-1} by simply changing the roughening pattern.

3.4.2 Quasi steady state response of the orthotic

Using the calibrated curvature sensor, we tested the quasi-steady state response of the orthotic (Figure 3.7). For our orthotic system, we assume a constant curvature along the orthotic and we chose pressure (P) as the input and curvature ($\kappa = 1/r$) as the output. The single input single output (SISO) system is described as:

$$\dot{\kappa} = f(\kappa, P) \qquad \text{(Equation 3.1)}$$

The quasi steady state response of this system where we fixed the internal pressure and assumed $\dot{\kappa} = 0$ was recorded and shown in Figure 3.7. It is a nonlinear system, due to the nonlinear properties of the hyperelastic elastomer and the geometry of the actuator design; however, we were able to fit it to a piecewise linear system. We divided the response into three ranges based on their slopes: (1) small curvature range (0 to 4 m^{-1}); (2) medium curvature range (4-7 m^{-1}); and (3) large curvature range (7-26 m^{-1}). Within each range, the system shows linearity. This approximation allowed us to characterize the dynamic response of the system and implement the gain scheduled controller design.

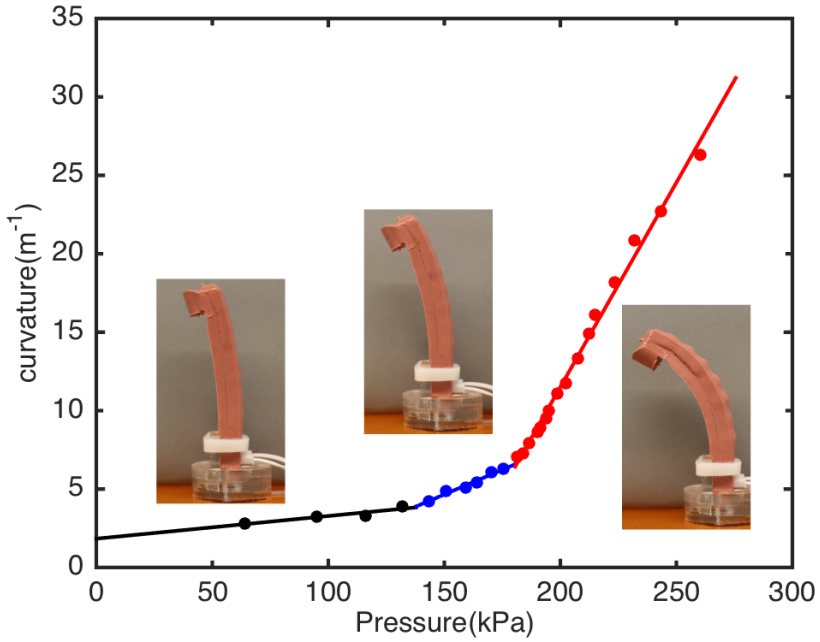

Figure 3.7 Quasi-static state response of the orthotic approximated by a piecewise linear model: black-small curvature range, blue-medium curvature range and red-large curvature range.

3.4.3 Orthotic dynamic response

For each of the three ranges described above, we tested the orthotic's dynamic response by generating sinusoidal input of different frequencies using a PWM signal (Figure 3.8). The results show that the dynamic responses for each region are similar, however, the gains (i.e. ratio of curvature to pressure) are different. This orthotic has a bandwidth of around 8 Hz, allowing it to absorb high frequency oscillation of pressure resulting from relative low frequency of PWM signal (60 Hz).

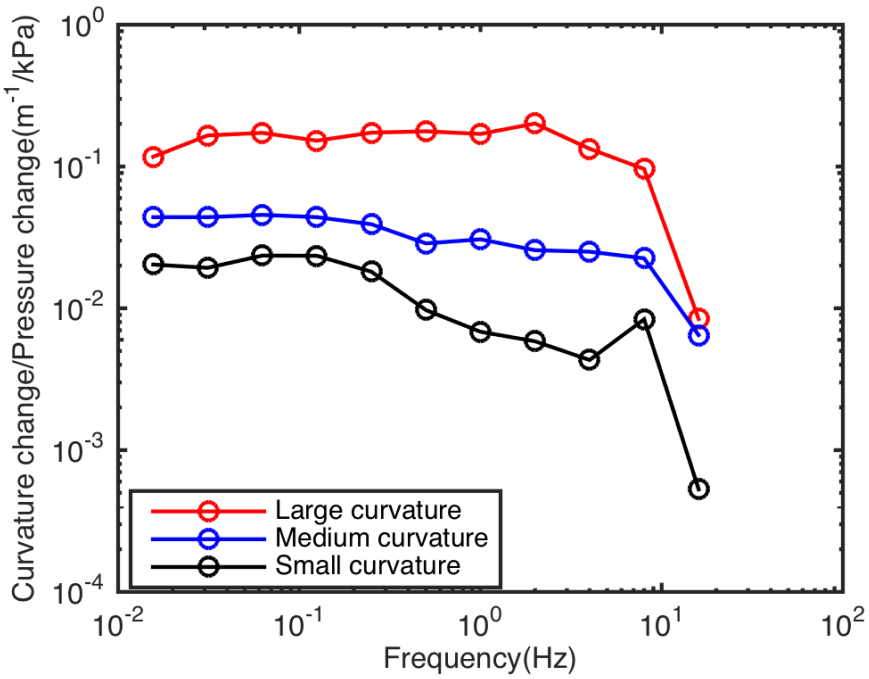

Figur3.8 Dynamic response of the orthotic at different curvature ranges.

3.4.4 Gain-scheduled PID controller

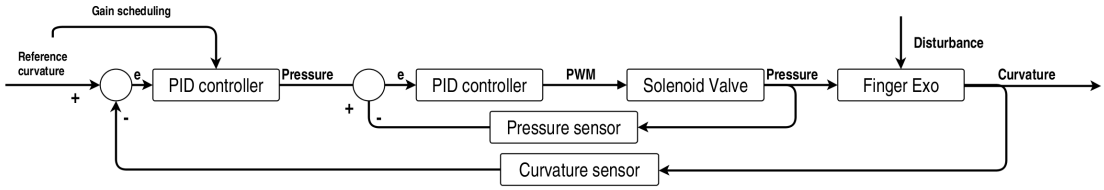

Figure 3.9 Block diagram of the dual loop control system

We used a dual loop PID to control the curvature of a free moving orthotic. The block diagram of the control system is shown in Figure 3.9. The inner loop was a low-level PID controller that uses input from a pressure sensor to adjust the internal pressure of the soft orthotic, which is required because pressure generated from the low-frequency PWM signal is nonlinear and frequency-dependent. Due to the plant's nonlinearity, a

fixed PID controller for the outer loop covering the complete range will cause either instability at high curvature range or slow response at small curvature range. Therefore, we used a gain-scheduled PID controller for the outer loop and, based on the static response of the system in Figure 3.7, we chose the scheduling variable to be the reference curvature (κ_{ref}). The discrete implementation of the gain-scheduled PID controller by our microcontroller is described as:

$$P_{command,k} = K_{P,j}e_{r,k} + K_{D,j}\left(e_{r,k} - e_{r,k-1}\right) + K_{I,j}\sum_{1}^{k} e_{r,i}$$

$$\text{where } j = \begin{cases} \text{Small range, when } \kappa_{ref} \in [0,4]\ \text{m}^{-1} \\ \text{Medium range, when } \kappa_{ref} \in (4,7]\ \text{m}^{-1} \\ \text{Large range, when } \kappa_{ref} \in (7,26]\ \text{m}^{-1} \end{cases}$$

(Equation 3.2)

To test the system's ability to absorb external disturbances and maintain its prescribed curvature, we intentionally introduced disturbances of different intensities (ranging from 2 m^{-1} to 5 m^{-1}) after it reached equilibrium (Figure 3.10). We also demonstrated its disturbance rejection ability by using a weight to block its way to the prescribed curvature (Video 3.1): it could easily push a small weight (e.g., 1N) and reach its targeted curvature, yet when it came to large weight (e.g., 5N), it oscillated and exhibited instability. Also, when the reference curvature was changing very rapidly, the system also exhibited instability. These dynamic instabilities are most pronounced at the threshold of each range in our piecewise linear function. To account for these highly dynamical systems, more sophisticated controllers will be required. The gain-scheduled PID controller parameters and performance are summarized in Table 3.3.

Despite the small tracking error and good performance in rejecting disturbances, the dual-loop gain-scheduled PID controller has a large rise time that makes it difficult to perform dynamic tracking of time-varying reference signals. While we do not address this further in this paper, using simpler discontinuous controller will reduce the rising time significantly.

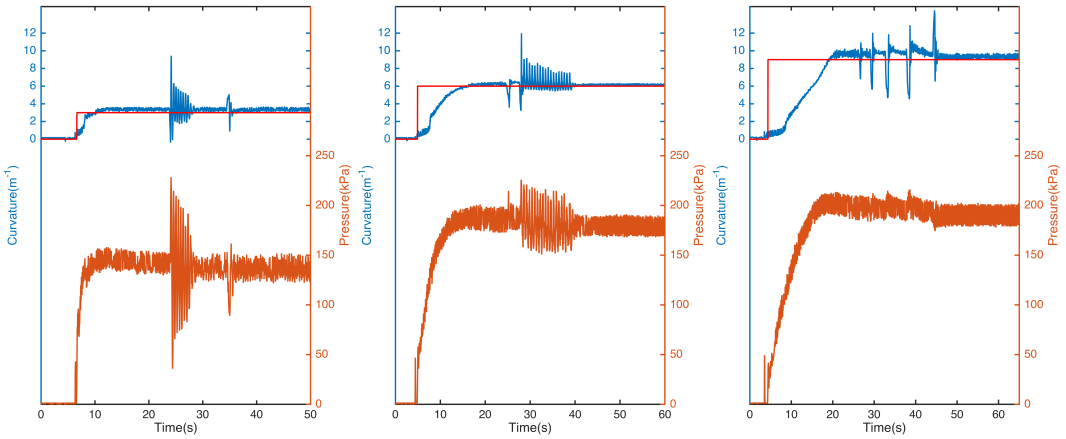

Figure 3.10 Gain-scheduled PID control performace of small curvature range (left), medium curvature range (middle) and large curvature range (right):a step reference signal is exerted (red) and the input pressure (orange) and output curvature (blue) was tracked through the embedded optical fiber sensor over time; disturbances were introduced to test the systems' sensitivity.

Table 3.3 parameters and performance of gain-scheduled PID controller

		Small range	Medium range	Large range
PID parameters	Kp	2.4	0.6	0.2
	Ki	0.0002	0.0005	0.002
	Kd	0.02	0.005	0.01
Performance	Steady state error, m^{-1}	0.26	0.19	0.37
	Rising time[a], s	2.5	8.2	12.1
	Stability[b]	Stable	Stable	Stable

a) Time required to rise from 10% to 90% of equilibrium value;
b) Tested by giving a disturbance of greater than 2 m^{-1};

3.5 Conclusions

In this chapter, I demonstrated a soft orthotic with position control via embedded solid-state curvature and pressure sensors. I described the fabrication of each part, including the rotational casted internal actuator, the laser cut optical fiber-based curvature sensor and their integration with off the shelf hardware. I developed a PID control system for both the optical and pressure sensing system and performed the sensor calibration, static characterization, dynamic characterization and demonstrated curvature feedback control.

My results not only increase the knowledge space of FEAs, including their nonlinearity, dynamic response and control complexity, but also demonstrates a low-cost, reliable, and easy to implement optical fiber based sensor. Though, in this chapter, I used a constant curvature assumption for the model and control the finger orthotic, it is a simple extension to include multiple fibers for piecewise curvature sensing. Future work will incorporate increased sensor densities for more sophisticated control of complex orthotics (e.g., gloves for rehabilitation [23]) and designing better controller for tracking dynamic reference input.

REFERENCES

[1] A. Bicchi and G. Tonietti, Fast and 'soft-arm' tactics. *IEEE Robot. Autom. Mag.* **11**, 22–33 (2004).

[2] D. Rus and M. T. Tolley, Design, fabrication and control of soft robots, *Nature* **521**, 467–475 (2015).

[3] B. Tondu, V. Boitier, and P. Lopez, Naturally compliant robot-arms actuated by McKibben artificial muscles, in *Proceedings of 1994 IEEE International Conference on Systems, Man, and Cybernetics*, 2 to 5 Octorber 1994, pp. 2635–2640.

[4] N. G. Tsagarakis and D. G. Caldwell, Development and control of a 'soft-actuated' exoskeleton for use in physiotherapy and training. *Auton. Robots*. **15**, 21–33 (2003).

[5] F. Ilievski, A. D. Mazzeo, R. F. Shepherd, X. Chen, and G. M. Whitesides, Soft robotics for chemists. *Angew. Chemie - Int. Ed.* **50**, 1890–1895 (2011).

[6] R. F. Shepherd, F. Ilievski, W. Choi, S. a. Morin, A. A. Stokes, A. D. Mazzeo, X. Chen, M. Wang, and G. M. Whitesides, Multigait soft robot. *Proc. Natl. Acad. Sci. U. S. A.* **108**, 20400–20403 (2011).

[7] P. Polygerinos, K. C. Galloway, E. Savage, M. Herman, K. O'Donnell, and C. J. Walsh, Soft robotic glove for hand rehabilitation and task specific training. in *Proceedings of the 2015 IEEE International Conference on Robotics and Automation*, 26 to 30 May 2015, Seattle, USA, pp. 2913–2919.

[8] H. K. Yap, J. H. Lim, F. Nasrallah, J. C. Goh, and R. C. Yeow, A Soft Exoskeleton for Hand Assistive and Rehabilitation Application using Pneumatic Actuators with Variable Stiffness. in *Proceedings of the 2015 IEEE International Conference on Robotics and Automation*, 26 to 30 May 2015, Seattle, USA, pp. 4967-4972.

[9] P. Heo, G. M.Gu, S. Lee, K. Rhee, and J. Kim, Current hand exoskeleton technologies for rehabilitation and assistive engineering. *Int. J. Pre. Eng. Man.* **13**, 807-824 (2012).

[10] T. Kline, D. Kamper, and B. Schmit, Control system for pneumatically controlled glove to assist in grasp activities. in *Proc. IEEE ICORR*, Chicago, USA, Jun. 28 to July 1, 2005, pp. 78-81.

[11] P. Polygerinos, S. Lyne, Z. Wang, L. F. Nicolini, B. Mosadegh, G. M. Whitesides, and C. J. Walsh, Towards a soft pneumatic glove for hand rehabilitation. *in Proceedings of 2013 IEEE/RSJ International Conference on Intelligent Robots and Systems*, 3 to 7 November 2013, Tokyo, Japan, pp. 1512-1517.

[12] A. D. Marchese, R. K. Katzschmann, and D. Rus, A recipe for soft fluidic elastomer robots. *Soft Robot.* **2**, 7-25 (2015).

[13] J. B. Chossat, Y. Tao, V. Duchaine, and Y. L. Park, Wearable soft artificial skin for hand motion detection with embedded microfluidic strain sensing. in *Proceedings of the 2015 IEEE International Conference on Robotics and Automation*, 26 to 30 May 2015, Seattle, USA, pp. 2568-2573.

[14] J. T. Muth, D. M. Vogt, R. L. Truby, Y. Mengüç, D. B. Kolesky, R. J. Wood, and J. A. Lewis, Embedded 3D printing of strain sensors within highly stretchable elastomers. *Adv. Mater.* **26**, 6307–6312 (2014).

[15] Y. Menguc, Y. L. Park, H. Pei, D. Vogt, P. M. Aubin, E. Winchell, L. Fluke, L. Stirling, R. J. Wood, and C. J. Walsh, Wearable soft sensing suit for human gait measurement. *Int. J. Rob. Res.* **33**, 1748–1764 (2014).

[16] G. Tonietti and A. Bicchi, Adaptive simultaneous position and stiffness control for a soft robot arm. in *Proc. IEEE/RSJ Int. Conf. Intelligent Robots Systems*, Lausanne, Switzerland, Sept. 30- Oct. 4, 2002, pp. 1992-1997.

[17] C. Duriez, Control of elastic soft robots based on real-time finite element method. in *Proceedings of the 2013 IEEE International Conference on Robotics and Automation*, 6 to 10 May 2013, Karlsruhe, Germany, pp. 3982–3987.

[18] A. D. Marchese, K. Komorowski, C. D. Onal, and D. Rus, Design and Control of a Soft and Continuously Deformable 2D Robotic Manipulation System. in *Proceedings of the 2014 IEEE International Conference on Robotics and Automation*, 31 May to 7 June 2014, Hong Kong, China, pp. 2189–2196.

[19] A. D. Marchese, R. Tedrake, and D. Rus, Dynamics and trajectory optimization for a soft spatial fluidic elastomer manipulator. in *Proceedings of the 2015 IEEE International Conference on Robotics and Automation*, 26 to 30 May 2015, Seattle, USA, pp. 2528-2535.

[20] H. Zhao, Y. Li, A. Elsamadisi, and R. F. Shepherd, Scalable manufacturing of high force wearable soft actuators. *Extreme. Mech. Lett.* **3**, 89–104 (2015).

[21] A. Djordjevich and M. Boskovic, Curvature gauge. *Sensor. Actuat. A-phys.* **51**, 193-198 (2002).

[22] K. S. Kuang, W. J. Cantwell, and P. J. Scully, An evaluation of a novel plastic optical fibre sensor for axial strain and bend measurements. *Meas. Sci. Technol.* **13**, 1523 (2002).

[23] R. Shepherd, H. Zhao, N. Heinze, T. Pfeiffer, Fluidic Actuators for Sensorimotor Feedback in Brain-Driven Scenarios with Magnetoencephalogaphy Recordings, filed as US Provisional No. 62/414,439.

CHAPTER 4

SOFT ORTHOSIS WITH INTEGRATED OPTICAL STRAIN SENSORS AND EMG CONTROL[‡]

4.1 Introduction

Human fingers and hands are frequently injured because they are delicate, complex, and used persistently. Over 3 million people in the U.S. suffer from hand or forearm disabilities [1], and worldwide hand injuries account for one third of all work injuries [2]. Due to the importance of hands and the prevalence of hand issues, there is an increasing effort towards developing hand orthotics. These efforts have resulted in active hand orthoses that have been used for rehabilitation training and restoring partial hand function [3]. To ensure safety and to reduce control complexity, some orthoses use mechanical compliance [4, 5] like under-actuated linkages [6] or low stiffness materials and structures (e.g., rubbers and flexible wires) [7, 8-11]. The orthoses made of elastomeric materials tend to be more comfortable, perhaps because their low elastic modulus (10 kPa<G'<1 MPa) [12] is similar to that of human skin (~100 kPa) [13].

Orthotic systems made of elastomers, and powered with fluid pressure, show potential for both rehabilitation and gripping assistance [8-11]. For both purposes, the control must use sensory feedback (e.g., sensing of position, force, etc.) in order to apply the intended motions or forces. Commercially available flexible sensors usually suffer

[‡] H. Zhao, J. Jalving, R. Huang, R. Knepper, A. Ruina, R. Shepherd, A helping hand: Soft orthosis with integrated optical strain sensors and EMG control. *IEEE Robot. Autom. Mag.* **23**, 55-64 (2016).

from low sensitivity, low repeatability and signal drift. Liquid-metal based resistive and soft capacitive sensors can be sensitive, but rely on expensive material or require a multi-step construction process [14-16]. Computer vision can provide high quality position sensing [17], but the camera systems, besides being costly and complex, can interfere with the user's motion. Due to these sensor limitations, most soft orthotics do not use them; instead they are "open-loop".

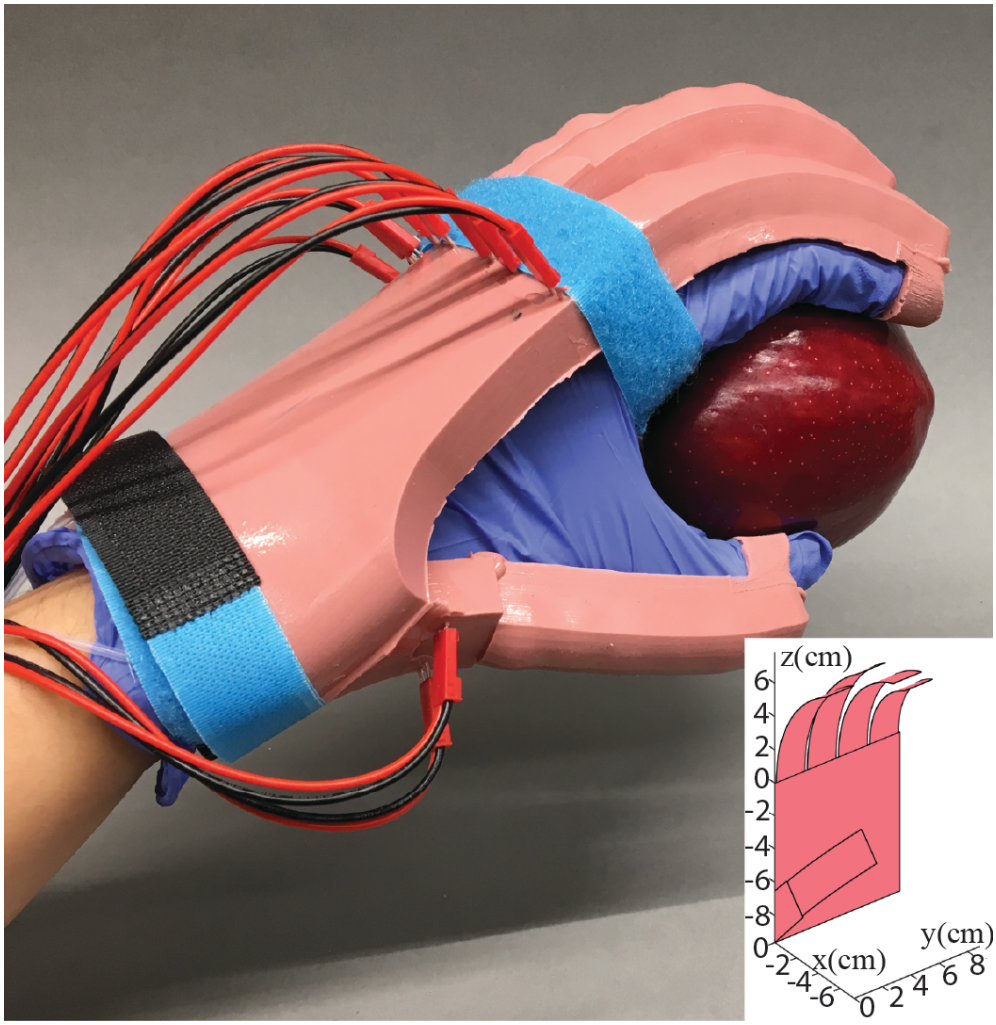

Figure 4.1 The glove is a soft orthosis. Here it helps a limp human hand grasp an apple. The inset shows a computer representation of the finger shape, as estimated using curvatures sensed by the embedded fiberoptic cables (these cables are the sensors used in the feedback control loop).

To address these issues, in this chapter I am developing a closed-loop controlled soft orthotic with integrated curvature sensors. My goal is a low cost soft orthotic that can be worn by a typical human hand and provide enough tip force at each finger to be helpful for grasping light objects (e.g., fruits), while also providing finger position (defined as average curvature) control. I have achieved reasonable functionality at these goals by using three advances described in this chapter: (i) a new rotational-casting technique, followed by an over-molding process for making the glove; (ii) measuring finger motion through optical losses in a molded-into-place etched plastic fiber-optic cable; and (iii) controlling motion with inexpensive, binary pneumatic switches controlled by a simple finite-state-machine. The composite glove is purely polymeric, highly compliant, and provides little resistance to natural motion when not pressurized. When inflated, the fingers of the glove curve and stiffen.

4.2 Soft orthotic glove with embedded sensors and actuators

Here I describe the overall design of the device of our soft orthosis (Figure 4.1).

4.2.1 Design

The glove has multiple functions: (i) it is an actively powered assistive device that helps each finger bend independently; (ii) it is a self-contained sensing device, the optical fibers that are molded into the fingers are curvature sensors, and thus also approximately sense deflection even for passive motions with no actuation; and (iii) by combining actuation and control, the glove is a robotic hand with fingers that can achieve prescribed motions or forces.

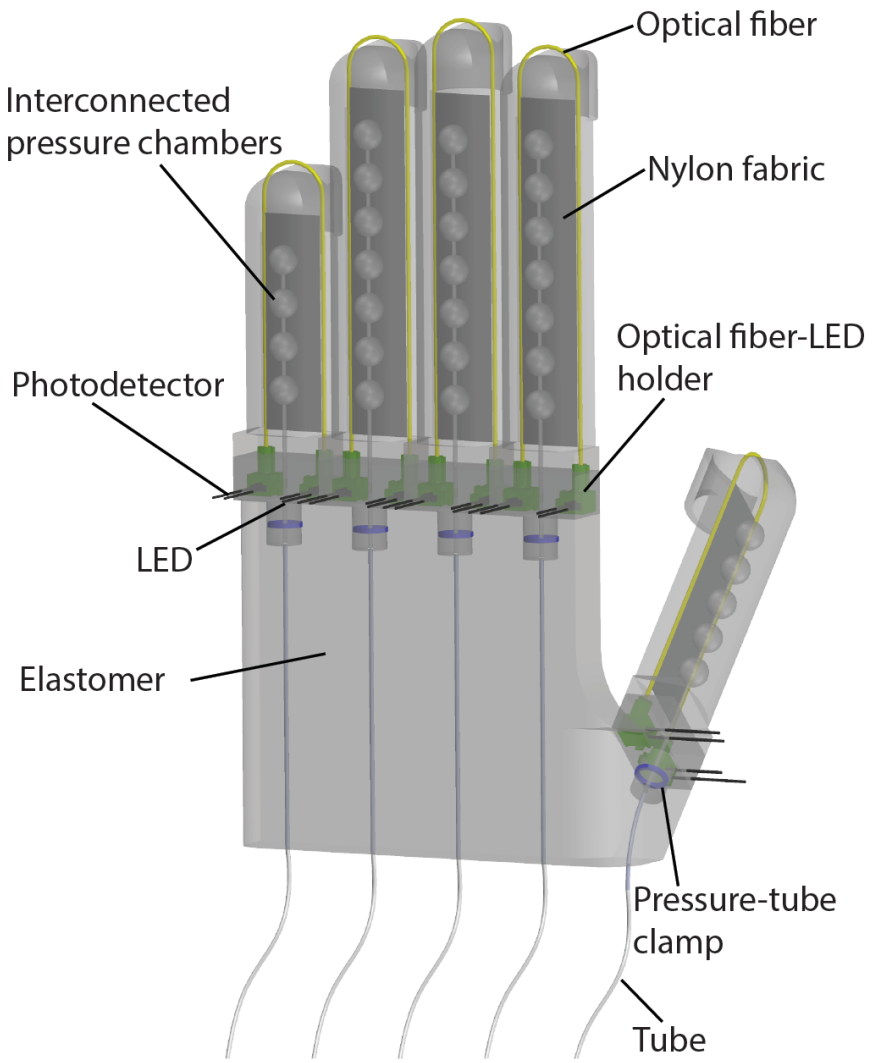

Figure 4.2 Schematic of the glove. Each component is labeled and exists on each finger: LEDs, pressure-chambers, optical fibers, photodetectors, nylon fabric, clamps, air-supply tubes and optical-component holders.

The body of the glove is made of a silicone elastomer (ELASTOSIL® M4601 A/B; Wacker Chemie, AG) to which we added 10% Silicone Thinner from Smooth-On, Inc. Each finger has a series of interconnected air chambers and a relatively inextensible nylon fabric along the palm side of each finger (Figure 4.2); upon fluid pressurization,

these actuators cause a grasping motion [18]. In the language of beam theory, the neutral axis for bending is just outside this strain-limiting fabric, and not in the middle of the finger. The finger mechanics are discussed further in Section 4.2.2.

The optical fiber sensors go from the root of the finger to the tip and back, bent in a U around the nylon fabric and are approximately in the bending beam's neutral plane. At one end of each optical fiber is an LED. At the other end is a photodetector (a "photo-Darlington" that reacts to light intensity by amplifying a current). These transmitter-sensor pairs are held to the fiber ends with custom 3D-printed holders and they are powered via thin electrical wires (red and black, Figure 4.1). Pneumatic power comes from an external pressure source via tubes that are inserted into holes molded into the wrist side of the glove. The tubes are connected to a pressure source via inexpensive three-position (pressurize, hold, and drain) electrical solenoid valves.

4.2.2 Actuator motion analysis

In this orthotic, each of the five fingers is made of a series of interconnected hollow spherical chambers. Figures 4.3(a) and (b) show a single finger in two configurations: (i) its "rest state," when the gauge pressure, the difference between the interior and exterior pressure, is zero, ΔP=0; and (ii) bent to a curvature $\kappa = 1/\rho$ caused by both the pressure difference, ΔP>0, and the bending load the finger carries.

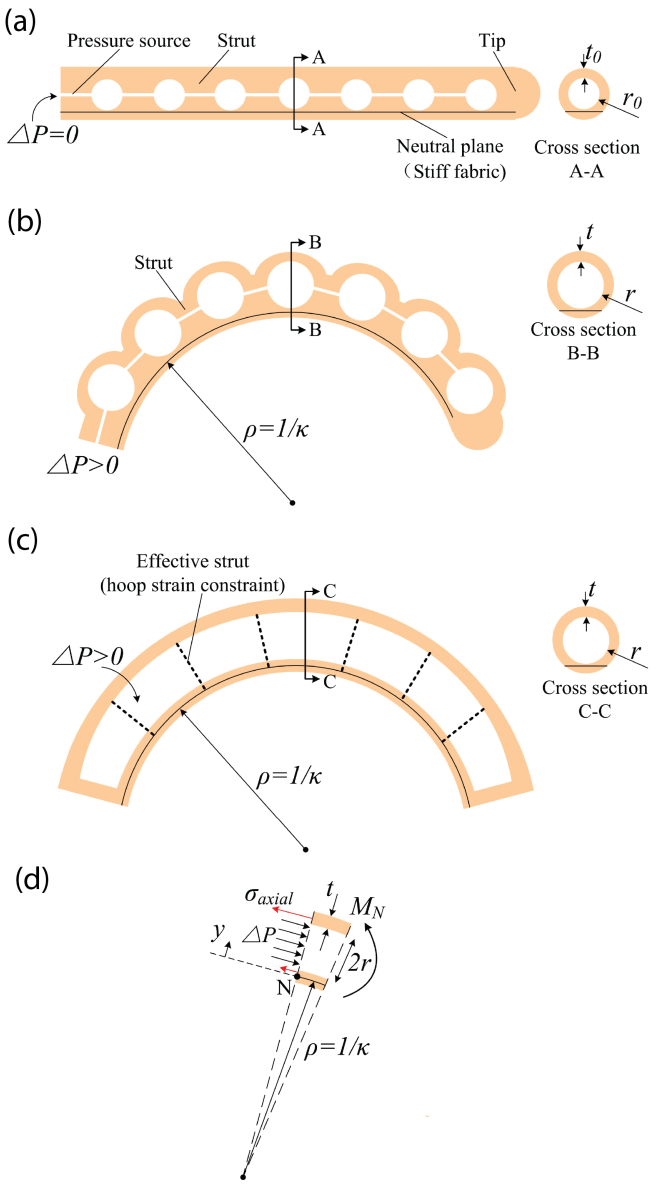

Figure 4.3 Schematic of one finger. (a) Rest state, with no loads and no pressure; (b) bending equilibrium state where internal pressure is balanced by the stretching of elastomer; (c) simplified model of the bending equilibrium state: struts are replaced by hoop strain constraint and other parameters stay the same; (d) free body diagram of a short section of the finger actuator at the bending equilibrium state with both pressure and an externally induced moment MN.

To approximately calculate the curvature κ in terms of other parameters, we further simply the finger model into a bending thin-wall cylindrical pressure vessel. The hoop strain (the increase in diameter of the cylindrical finger) is constrained by the "struts"

(the walls between the spheres) (Figure 4.3(b)). We model the "strut" structures by assuming the hoop strain is constrained (Figure 4.3(c)). We model the whole cylindrical finger (elastomer, stiff fabric at the bottom, gas pressure and radial constraint) using a composite-beam model.

We approximate the fabric at the finger bottom as inextensible, thus the beam neutral axis is at the finger bottom. We assume that any external axial load is at the neutral axis so does not enter the bending calculations. For simplicity, we assume that the cylinder wall thickness t is much less than the finger radius *r* (*t*<<*r*) and that the elastomer is linear and isotropic. The net moment M_N about the neutral axis is due to the axial elastic tension stress in the elastomer σ_{axial} (acting on the hollow cylinder with radius r, thickness t and moment of inertia about the neutral axis of $I_N = 3\pi r^3 t$) and that due to the gas pressure ΔP (acting on the area πr^2 a distance r from the neutral axis).

$$M_N = -\int \sigma_{axial}\, y dA + r \cdot \Delta P \cdot (\pi r^2) \qquad \text{(Equation 4.1)}$$

Equilibrium of the cylinder in the y direction (Figure 4.3(d)) gives a modified version of the standard thin-walled pressure vessel formula

$$\Delta P \cdot r = \sigma_{hoop} t + T_s \qquad \text{(Equation 4.2)}$$

where σ_{hoop} is the hoop stress in the elastomer and T_s is a force per length that comes from restraint against hoop strain (against cylinder bulging). In the model here, the restraint represents the sidewall struts of the spheres. It could also represent restraint from circumferential fibers [20] or from interior foam [21]. As per conventional

composite beam theory, we assume plane normal sections remain plane and normal and hence the elastomer axial strain is given by

$$\epsilon_{axial} = \kappa y \qquad \text{(Equation 4.3)}$$

The linear elastic material properties of the elastomer are:

$$\epsilon_{axial} = \sigma_{axial}/E - \nu\,\sigma_{hoop}/E - \nu\,\sigma_{radial}/E$$

$$\epsilon_{hoop} = \sigma_{hoop}/E - \nu\,\sigma_{axial}/E - \nu\,\sigma_{radial}/E \qquad \text{(Equation 4.4)}$$

where the elastomer elastic modulus is E and Poisson's ratio ν.

As per usual pressure-vessel theory, in which the fluid pressure is much smaller than the vessel (elastomer) stresses, we neglect the radial stress, setting $\sigma_{radial} = 0$. As mentioned in regard to Equation 4.2 above, for simplicity we assume that the restraint against bulging can be represented as a circumferential stress per unit length, T_s. Again, for simplicity, we think of these fibers as having modulus (force per unit length) E_f, so

$$T_s = E_f \epsilon_{hoop} \qquad \text{(Equation 4.5)}$$

Substitution of Equation 4.2 to 4.5 into Equation 4.1 and integrating over the hollow cross section we get

$$\kappa = -\frac{E_f - \nu^2 E_f + Et}{3\pi r^3 t\left(EE_f + E^2 t\right)} M_N + \frac{E_f - \nu^2 E_f - 2E\nu t + Et}{3t\left(EE_f + E^2 t\right)} \Delta P$$

(Equation 4.6)

With no radial restraint ($E_f = 0$) and ν~0.5, the common approximation for elastomeric materials, the coefficient of ΔP vanishes and the pressure has no effect on curvature or bending moment. Thus for elastomeric fingers of this general design, the induction of curvature is entirely dependent on the restraint tension, T_s; with no circumferential constraint, in this case from struts, but possibly from interior foam or circumferential fibers, there is no bending due to pressure. The simplest approximation for this restraint is to assume inextensible fibers, struts or whatever ($E_f = \infty$), in which case the relation between pressure, curvature and net finger moment is

$$\kappa = -\frac{1-\nu^2}{3E\pi r^3 t} M_N + \frac{1-\nu^2}{3Et} \Delta P \ . \qquad \text{(Equation 4.7)}$$

This linear-elastic small-strain composite-beam model shows, for example, how curvature increases with pressure and decreases with increasing elastomer modulus and elastomer thickness. Most importantly, the model shows the necessity of radial (circumferential) constraint in elastomeric fingers for pressure to cause bending, at least to the extent that this small-strain linear theory applies. When applied to long and narrow balloons (ν=0.5), the theory says that to first order there is no elongation with pressurization. In reality, however, with large expansions long and narrow balloons do elongate some. Similarly, even without radial constraint, elastomeric fingers will bend with large enough pressurization (violating the simple small strain theory here).

The maximum net finger moment can also be derived from the above model by setting $\kappa = 0$:

$$M_{Nmax} = \pi r^3 \Delta P \qquad \text{(Equation 4.8)}$$

When substituting $\Delta P = 270$ kPa and $r = 10$ mm, we get $M_{Nmax} = 0.8\ \mathrm{N \cdot m}$. For an 8 cm long finger this yields a theoretical upper limit for the finger tip force of 10 N.

4.3 Manufacture of the soft orthotic glove

Our orthotic glove is constructed using a new rotational-casting technique followed by an over-molding process. The optical fiber sensor is also fabricated from an innovative method.

4.3.1 Rotational casting

There exist several methods to produce soft actuators [22], each with its own drawbacks. Replica molding (sometimes referred to as soft lithography) can lead to delamination at material bonds. Investment, or lost-wax, casting involves the building and destruction of molds for each part, costing time and money. With rotational casting, however, we have molds that are reusable and simultaneously produce multiple actuators that do not delaminate when pressurized (Figure 4.4) [19]. For this process, we 3D print a mold, partially fill it with viscous pre-elastomers, fix the mold onto the casting machine, and rotate it until the elastomer solidifies. Finally, we peel the actuators from the molds (Figure 4.4(c)).

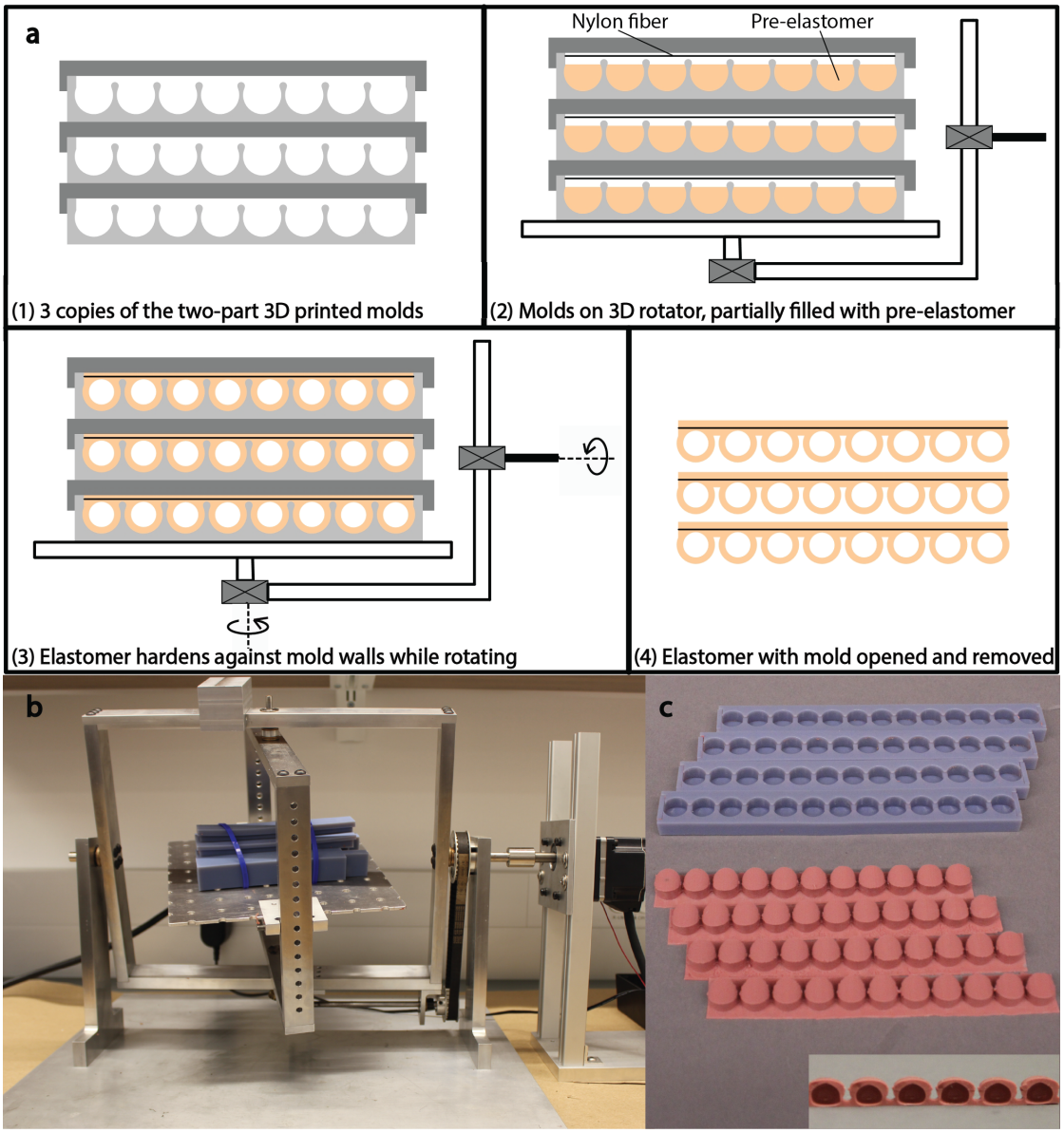

Figure 4.4 Rotational casting. (a) Casting process: 1) Molds; 2) Partially filled molds; 3) Rotational casting process; 4) Final elastomer structure. (b) Rotational casting machine with multiple molds affixed. (c) Molds used (top) and monolithic elastomers produced from those molds, with cross sections shown in the bottom right corner.

4.3.2 Preparation of optical-fiber sensors

Our strain sensor is a lightguide fabricated from one piece of plastic optical fiber. First, using thermoforming at 50 ℃, we form the optical fiber into a U shape that allows us to reliably align it into the finger actuator (Figure 4.5). Then, using a laser

engraver (50 Watts Epilog Zing 24), we etch off a thin layer from one side of the U (lower right of Figure 4.5). Etching damages the cladding layer of the fiber, reducing internal reflections, part of the light is thus lost when travelling the length of the fiber. Because only one side is etched, the amount of light dissipation is affected by bending; we measure this light amount change via a photodetector and correlate it to curvature [23].

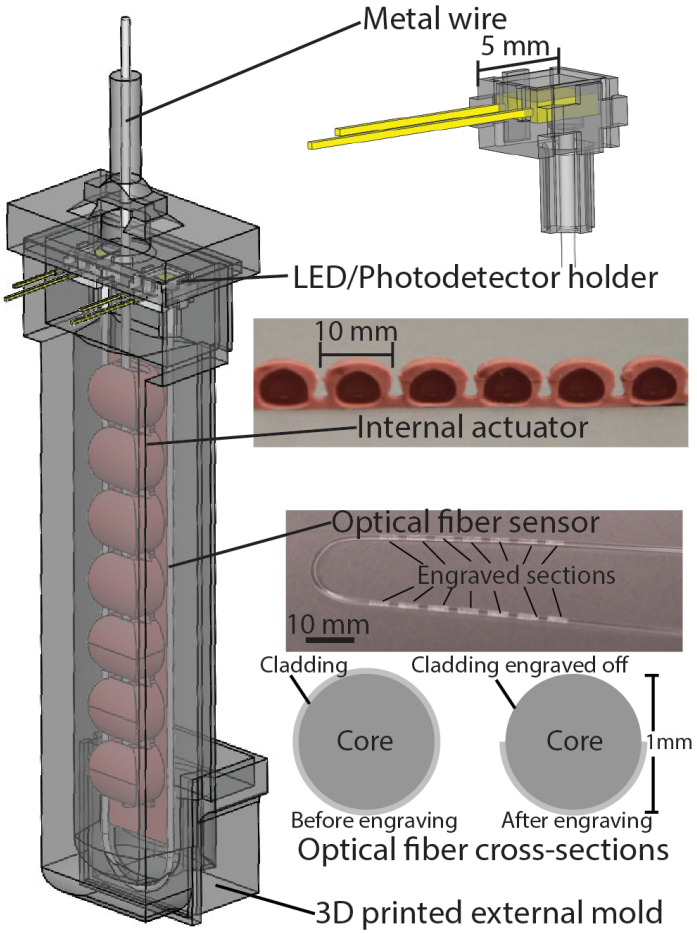

Figure 4.5 Over-molding of different components. Internal chambers of the actuator are aligned with the over-mold. One end of the U-shaped lightguide attaches to the fixtures in the over-mold. The fixtures are attached by the pins of the LED and a photodetector. After assembly, silicone pre-elas tomer is poured into the over-mold to form a single finger actuator with sensors.

If too much of the fiber is engraved, the light dissipation can saturate while the sensor is still in a working range of curvature. To ensure that our sensor lies below this saturation limit, we only engrave a sequence of short sections of the surface. The lightguide responds to both extension and compression of the engraved side: compression increases the signal intensity (preferable) and extension decreases it. Therefore, we align the fibers within the fingers to operate in compression, which has an additional benefit of reducing the likelihood of fatigue fracture of the micro-cracks which we introduced during etching.

4.3.3 Over-molding

We assemble the rotational casting and the lightguide sensor in a 3D printed finger mold, and over-mold them into a self-contained finger actuator. A steel wire is used to mold a connecting pathway between the internal actuators and is fixed in place using a 3D printed mold cap (Figure 4.5). A custom 3D-printed fixture holds the LED, photodetector, and the optical fiber sensor in the correct positions and orientations. After assembling, more silicone pre-elastomer is poured into the mold to over-mold into a complete finger with integral actuator and sensor. We cast five fingers of appropriate lengths into a complete hand orthotic.

4.4 Control system

The present control system uses a state machine controller shown in Figure 4.6. Each finger is controlled by its own 3-position valve (air in, hold, and air out), and each 3-position valve is made from two 2-position valves (air in, and air out) mounted to a

pressure manifold. The simple non-linear controller lets air into a finger to increase curvature, and lets air out to decrease curvature. If the curvature is close to the target (within a specified deadband) then flow is stopped, maintaining gas volume, and preventing set-point hunting. Approaching this deadband region, flow is stopped to prevent overshoot.

The 2-way valves are normally closed (Figure 4.6(a); X-valve, Parker Hannifin Corporation) and switched using power transistors (TIP120). The inflating valve connects the gas source to the actuator, and the deflating valve vents the actuator to the atmosphere. When the inflating valve is open and deflating valve is closed, gas from the source pressurizes the actuator—the "in" state. When the inflating valve is closed and the deflating valve is open, gas vents from the actuator to atmosphere—the "out" state. When both are closed, gas remains inside the actuator—the "hold" state (Figure 4.6(a, b)). Viscoelasticity, gas compressibility, and gas-line resistance cause a lag between valve decisions and sensed motion and leads to an overshoot. Creating a deadband big enough to inhibit the resulting overshoot oscillations, however, leads to poor system accuracy. To prevent oscillations and maintain accuracy, we added state transitions to cut flow or leakage before the acceptable target deadband was sensed as reached (Figure 4.6(c) and Table 4.1). This controller code is repeated ad-infinitum at time intervals of Δt=5ms, as that is slightly longer than the timing required for the valves to open or close.

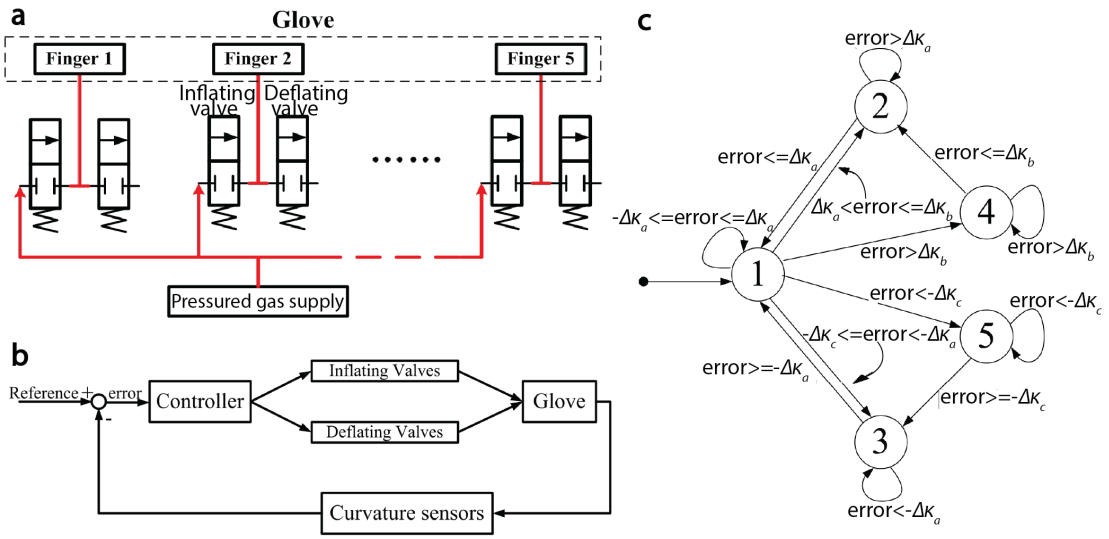

Figure 4.6 Control system: (a) diagram of how each finger is connected to the gas supply through valves; (b) block diagram of the control system; (c) controller represented in a state machine diagram, where error is calculated from the current measured value subtracted from the targeted value and $\Delta\kappa_a$ $\Delta\kappa_b$ and $\Delta\kappa_c$ are three threshold parameters to compare with error; definitions of state 1 to 5 is in Table 4.1.

Each finger has its own state-machine controller, with each having five states. A state corresponds to a command to each three-position valve. State transition conditions are based on the 'error' $\Delta\kappa$ —the difference between the target and the measured curvatures. A check for a transition is made every controller cycle. There are three threshold parameters in the state-machine controller: acceptably small error is specified as "$\Delta\kappa_a$", where large-enough $\Delta\kappa_a$ prevents excessive attempts at correction, and "$\Delta\kappa_b$" and "$\Delta\kappa_c$" define the thresholds of the large-error region. When these thresholds are exceeded, inflation or deflation occurs, respectively. Between the high and low error regions, two settling time variables "*X*" and "*Y*" for positive and negative error determine a remnant valve-off time. In effect, the valves are attenuated by 1/(*X*+1) and 1/(*Y*+1) in these intermediate-error bands. In general, $\Delta\kappa_a$ determines the accuracy of tracking but leads to an instability if set too small. Increasing $\Delta\kappa_b$ and

$\Delta\kappa_c$ will increase stability but decrease the actuating speed. *X* and *Y* represents how long to wait during both the "in and hold" and "out and hold" states—increasing X and Y improves stability and decreases speed. The valves are off in the deadband, fully actuated towards the target when the error is large, and attenuated by 1/(*X*+1) and 1/(*Y*+1) in zones near the deadband. In effect, this is an implementation of a three level Pulse Width Modulation (PWM) system with three levels (all off, all on, and attenuated).

Table 4.1 Actions during states

State	Inflating valve	Deflating valve	Comments
1	Off for Δt	Off for Δt	"Hold"
2	On for Δt, then Off for $X\Delta t$	Off for $(X+1)\Delta t$	"In and hold"
3	Off for $(Y+1)\Delta t$	On for Δt, then Off for $Y\Delta t$	"Out and hold"
4	On for Δt	Off for Δt	"In"
5	Off for Δt	On for Δt	"Out"

4.5 Experimental results and discussion

4.5.1 Calibration of optical-fiber sensors

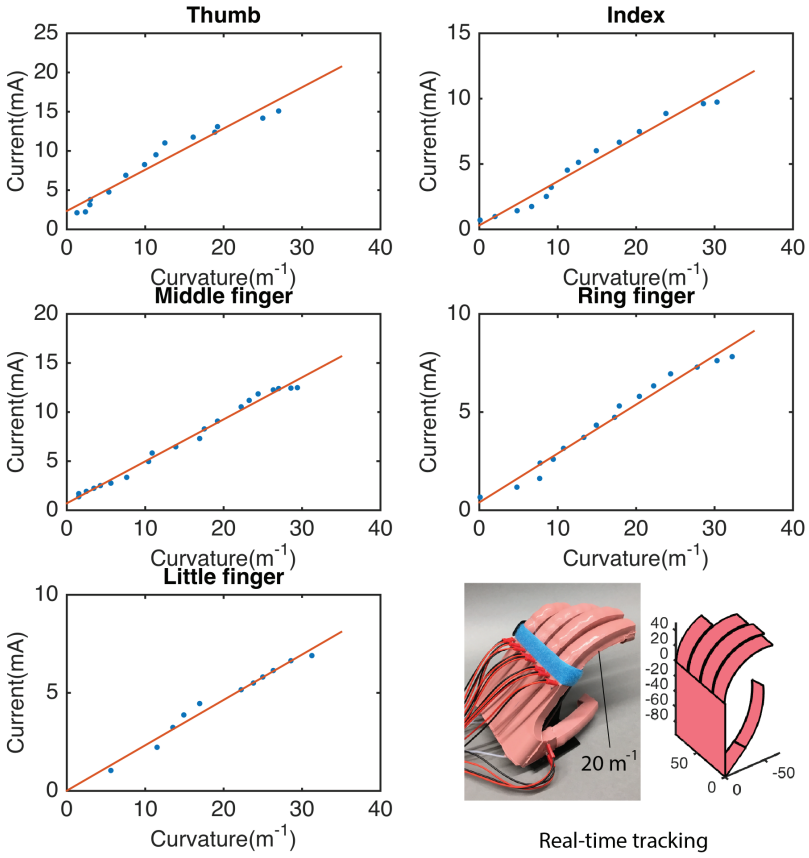

Figure 4.7 Lighguide calibration. Photodetctor current output at various curvatures of the actuators. Blue dots are measured results and red lines are linear fits. The last figure shows the real time curvature tracking of the glove after calibration where all fingers are bent at a curvature of 20 m^{-1} (5 cm radius).

To calibrate the lightguides, we imaged each finger from the side while measuring the current output I from the photodetector (Figure 4.7). We calculated the curvature κ by picking 4-7 points (determined by the number of chambers in the actuator) from each picture and fitting them to a circle. For curvature from 0 to 35 m^{-1}, the calibrations of all five fingers were linearly fit with a sensitivity ($\lambda \propto \Delta I/\Delta\kappa$) range of 0.23 mA$\cdot$ m

$< \lambda <$0.49 mA· m. This sensitivity can be adjusted by changing both the engraving pattern and LED intensity. Other sensor features include: (i) a fast response time of 5 ms; (ii) a high curvature resolution of 0.04 m^{-1}; (iii) repeatability of 0.05 m^{-1}, measured by the standard deviation of a single curvature over five different tests. The response time, resolution and repeatability outperform other sensing systems based on resistance and capacitance [14-16]. The sensor, however, has a nonlinear response beyond the range we tested; λ decreases at higher curvatures.

4.5.2 Force test with the electromyography (EMG) signal

We did a force test for each finger actuator [19] and the output tip force ranged from 0 to 5N, by applying pressure ranging from 0 to 270 kPa [24]. This force output is similar to that of fiber-reinforced soft actuators reported as hand assistive device [9, 10], smaller than a cable driven soft glove [7], and at most half of the theoretical upper limit calculated above. To better understand how this orthosis functions as a hand assistive device, we measured the applied force of four fingers while monitoring the EMG intensity as a measure of the user's effort [25]. A healthy user wore the glove and held a hand exerciser as shown in Figure 4.8. On each button of the hand exerciser, we attached a force sensor (FlexiForce A301 Sensor from Tekscan) to record the force exerted on it. Simultaneously, we measured forearm muscle exertion using a MyoTM armband that uses eight EMG sensors applied uniformly around the forearm.

The wearer pressed the four buttons to an average force of 1.0 N, and we then activated the orthosis. We observed an immediate increase in force from 1.0 N to 1.6 N, which then dropped to 1.4 N. We then depressurized the orthosis and observed an immediate drop in applied force to 0.3 N, which then rose up to 1.0 N. We repeated this process and got similar results. Finally, we asked the user to press the buttons to achieve a force of 1.6 N, using solely their own effort.

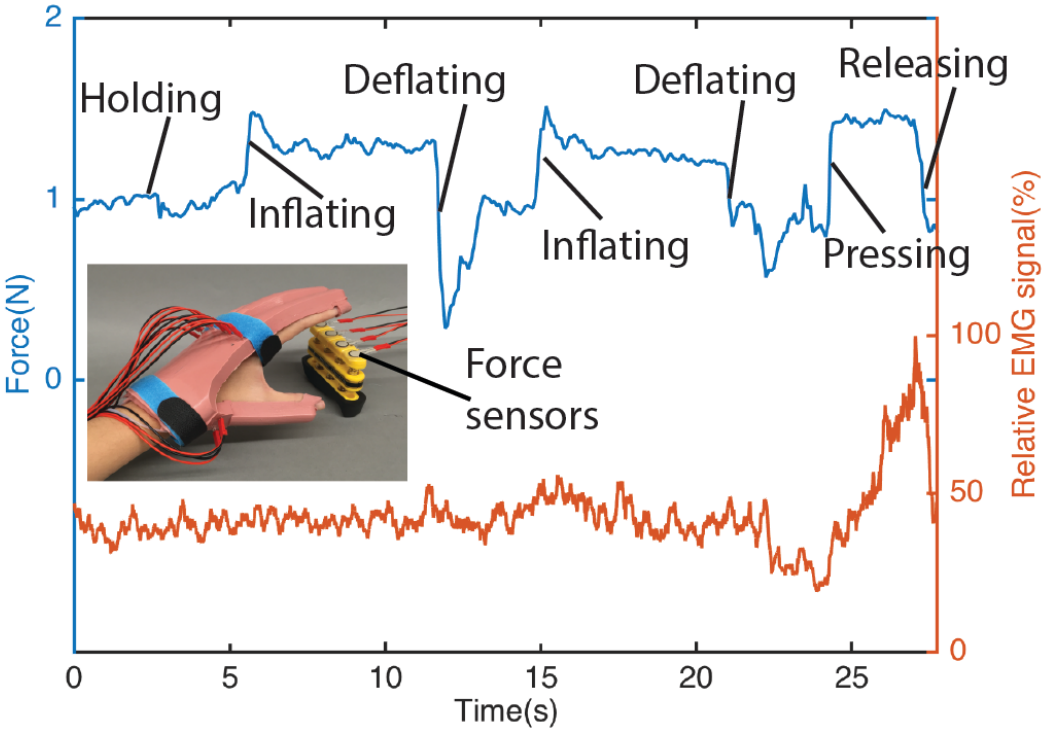

Figure 4.8 Force test with worn glove. A hand exerciser with force sensor attached to each button was held by the user and the EMG signal was recorded at the same time.

From the above experiments, we saw that the actuator caused a significant and sudden overshoot force when activated and deactivated, the system then reached a stable state. During the later period, when the user was achieving 1.6 N of applied force from 1.0 N, we recorded an increase of the EMG intensity (the summation of all eight sensors

of the armband). While the user was applying 1.0 N of force and the orthosis was augmenting to 1.6 N, the measured EMG intensity remained constant. This experiment demonstrated that the orthosis was assisting the user by augmenting his force by a factor of 1.6, saving muscular effort.

4.5.3 Control results

As a test of our controller, we performed unloaded tracking tests for step changes in a curvature target. We ran the controller in an Arduino MEGA, using the analogue and digital pins for sensor input and valve commands, respectively. We set $\Delta\kappa_a$=0.3 m^{-1}, X=Y=3 (attenuation by 1/4 in near-deadband zones) and chose three different values of $\Delta\kappa_b$ and $\Delta\kappa_c$.

We tested the controller's step response using various step stimuli for various durations (Figure 4.9). When $\Delta\kappa_b$=$\Delta\kappa_c$=$\Delta\kappa_a$ the controller is an on-off controller with deadband and no transitional zone, leading to oscillations around the reference. When $\Delta\kappa_b$=$\Delta\kappa_c$=4$\Delta\kappa_a$, we observed good accuracy (within 0.3 m^{-1} curvature), good stability (no oscillation or overshoot) and high speed (rise time of about 150 ms). When $\Delta\kappa_b$=$\Delta\kappa_c$=13$\Delta\kappa_a$, a large intermediate attenuation zone, the rise time increased to 500 ms.

Many have explored the use of EMG signals for control of orthotics [26]. We attempted to check the potential of our orthotic towards this goal. We used a filtered EMG signal as a reference to represent a curvature target.

While a Butterworth low-pass filter has been used with myoelectric signals [26], we found that persistent force application by the fingers did not translate into a constant filtered signal. Instead, we collected an EMG signal from a user's forearm using the MyoTM armband at 200 Hz and used a moving average filter of 100 samples every 200 ms to produce a 5 Hz signal with less noise. We then fed this signal into our controller as the reference signal. Figure 4.10 shows both the raw EMG signal and the processed data for tracking. Our results show that the orthosis, using a state machine controller, can follow an EMG signal with small overshoot and small oscillation.

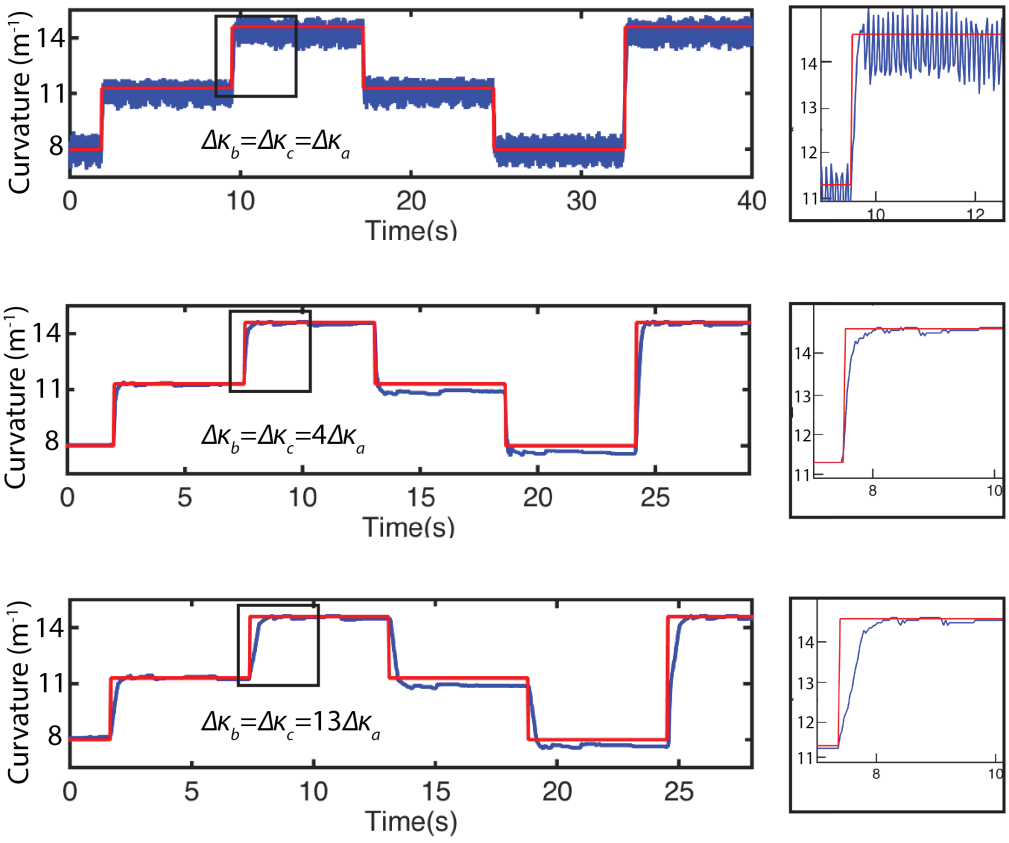

Figure 4.9 Step response of the controller with three different state-transition parameter sets. Red lines are the input signals and blue lines are the measured system responses. The right plots show enlarged views of step response data.

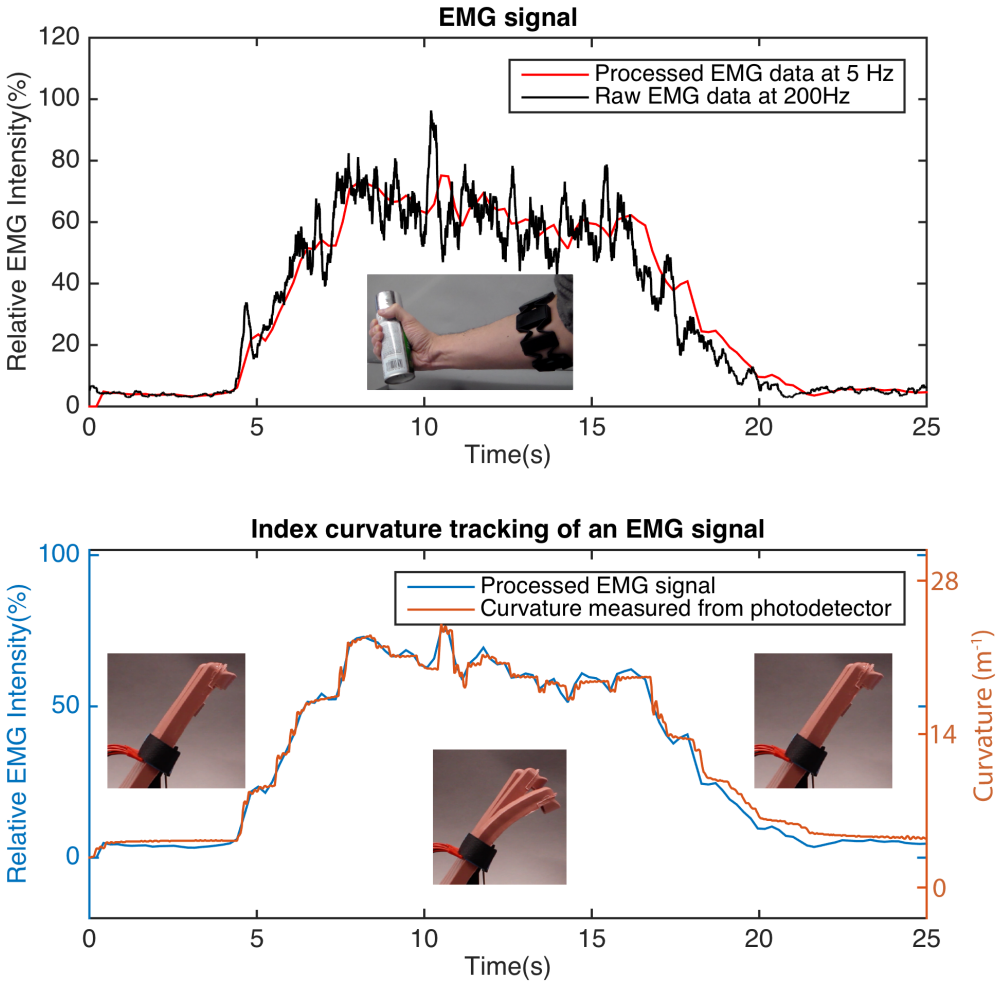

Figure 4.10 Index curvature tracking of an EMG signal previously collected from a healthy user.

4.6 Conclusion and Future Work

I designed both the hardware and a control method for a closed loop soft orthosis. I performed initial quantification of its force augmenting capabilities and feedback control via optical fiber sensors embedded into each actuator. I also showed that the orthotic can be used to track commands from an EMG signal. My simplified linear mechanical analysis shows the key role of radial, that is circumferential, constraint for

the functioning of inflated elastomeric fingers. It also shows that stronger fingers are possible using circumferential unidirectional fibers around round-section polymeric fingers with axial constraint at the bottom, verifying prior experimental results [20].

My system, promising as it is, needs improvement. First, our present choice of materials and actuator design do not yield enough force to conduct many common daily activities (e.g, opening a jar requires a torque of about 1 to 2 $N \cdot m$ [27], requiring tens of Newtons to grip a typical lid). Tougher materials, such as polyurethanes, along with larger circumferential constraint, should allow me to achieve higher forces. Next, with a more refined state-machine controller I should be able to improve the system's tracking ability. Finally, my sensing, and hence control, is limited to only curvature. With compliant force sensors, I could achieve force or compliance control. My hope is that the low cost of our device and controller will lead to devices that could be useful to a large population of patients in need of hand prostheses.

REFERENCES

[1] R. C. Ficke, Digest of Data on Person with Disabilities. Department of Education. USA, Januray 1992. Available: http://eric.ed.gov/?id=ED347767.

[2] J. Marty, B. Porcher, and R. Autissier, Hand injuries and occupational accidents. Statistics and prevention. *Ann. Chir. Main.* **2**, 368-370 (1982).

[3] P. Heo, G. M. Gu, S. Lee, K. Rhee, and J. Kim, Current hand exoskeleton technologies for rehabilitation and assistive engineering. *Int. J. Precis. Eng. Man.* **13**, 807-824 (2012).

[4] Y. Hasegawa, Y. Mikami, K. Watanabe, and Y. Sankai, Five-fingered assistive hand with mechanical compliance of human finger. in *Proc. IEEE Int. Conf. Robotics Automation*, Pasadena, CA, USA, May 19- 23 2008, pp. 718-724.

[5] A. Bicchi and G. Tonietti, Fast and" soft-arm" tactics. *IEEE Robot. Autom. Mag.* **11**, 22-33 (2004).

[6] J. Iqbal, H. Khan, N. G. Tsagarakis, and D. G. Caldwell, A novel exoskeleton robotic system for hand rehabilitation–Conceptualization to prototyping. *Biocybern. Biomed. Eng.* **34**, 79-89 (2014).

[7] H. In, B. B. Kang, M. Sin, and K. Cho, Exo-Glove: A Wearable Robot for the Hand with a Soft Tendon Routing System. *IEEE Robot. Autom. Mag.* **22**, 97-105 (2015).

[8] P. Polygerinos, K. C. Galloway, E. Savage, M. Herman, K. O. Donnell, and C. J. Walsh, Soft robotic glove for hand rehabilitation and task specific training. in *Proc. IEEE Int. Conf. Robotics Automation*, Seattle, WA, USA, May 26- 30 2015, pp. 2913-2919.

[9] H. K. Yap, J. H. Lim, F. Nasrallah, F. Z. Low, J. C. Goh, and R. C. Yeow, MRC-glove: A fMRI compatible soft robotic glove for hand rehabilitation application. in *Proc. IEEE ICORR*, Singapore, Singapore, Aug. 11- 14 2015, pp. 735-740.

[10] P. Polygerinos, K. C. Galloway, S. Sanan, M. Herman, and C. J. Walsh, EMG controlled soft robotic glove for assistance during activities of daily living. in *Proc. IEEE ICORR*, Singapore, Singapore, Aug. 11- 14 2015, pp. 55-60.

[11] J. H. Low, M. H. Ang, and C. H. Yeow, Customizable soft pneumatic finger actuators for hand orthotic and prosthetic applications. in *Proc. IEEE ICORR*, Singapore, Singapore, Aug. 11- 14 2015, pp. 380-385.

[12] D. Rus and M. T. Tolley, Design, fabrication and control of soft robots. *Nature* **521**, 467-475 (2015).

[13] P. G. Agache, C. Monneur, J. L. Leveque, and J. De Rigal, Mechanical properties and Young's modulus of human skin in vivo. *Arch. Dermatol. Res.* **269**, 221-232 (1980).

[14] R. L. Hammond, Y. Menguc, and R. J. Wood, Toward a modular soft sensor-embedded glove for human hand motion and tactile pressure measurement. in *Proc. IEEE/RSJ Int. Conf. Intelligent Robots Systems*, Chicago, IL, USA, Sept. 14- 19 2014, pp. 4000-4007.

[15] J. Chossat, Y. Tao, V. Duchaine, and Y. Park, Wearable soft artificial skin for hand motion detection with embedded microfluidic strain sensing. in *Proc. IEEE Int. Conf. Robotics Automation,* Seattle, WA, USA, May 26- 30 2015, pp. 2568-2573.

[16] P. Roberts, D. D. Damian, W. Shan, T. Lu, and C. Majidi, Soft-matter capacitive sensor for measuring shear and pressure deformation. in *Proc. IEEE Int. Conf. Robotics Automation*, Karlsruhe, Germany, May 6- 10 2013, pp. 3529-3534.

[17] A. D. Marchese, K. Komorowski, C. D. Onal, and D. Rus, Design and control of a soft and continuously deformable 2d robotic manipulation system. in *Proc. IEEE Int. Conf. Robotics Automation*, Hong Kong, China, May 31- June 7 2014, pp. 2189-2196.

[18] R. F. Shepherd, F. Ilievski, W. Choi, S. A. Morin, A. A. Stokes, A. D. Mazzeo, X. Chen, M. Wang, and G. M. Whitesides, Multigait soft robot. *Proc. Nat. Acad. Sc. U. S.* **108**, 20400-20403 (2011).

[19] H. Zhao, Y. Li, A. Elsamadisi, and R. F. Shepherd, Scalable manufacturing of high force wearable soft actuators. *Extreme. Mech. Lett.* **3**, 89–104 (2015).

[20] R. Deimel, and Oliver Brock, A compliant hand based on a novel pneumatic actuator. in *Proc. IEEE Int. Conf. Robotics Automation*, Karlsruhe, Germany, May 6-10 2013, pp. 2047-2053.

[21] B. C. Mac Murray, X. An, S. S. Robinson, I. M. van Meerbeek, K. W. O'Brien, H. Zhao, and R. F. Shepherd, Poroelastic Foams for Simple Fabrication of Complex Soft Robots. *Adv. Mater.* **27**, 6334-6340 (2015).

[22] A. D. Marchese, R. K. Katzschmann, and D. Rus, A recipe for soft fluidic elastomer robots. *Soft Robot.* **2**, 7-25 (2015).

[23] A. Djordjevich and M. Boskovic, Curvature gauge. *Sensor. Actuat. A-phys.* **51**, 193-198 (2002).

[24] H. Zhao, R. Huang, and R. F. Shepherd, Curvature Control of Soft Orthotics via Low Cost Solid-State Optics. in *Proc. IEEE Int. Conf. Robotics Automation*, Stockholm, Sweden, May 16- 21 2016, pp. 4008-4013.

[25] O. M. Blake and J. M. Wakeling, Estimating changes in metabolic power from EMG. *SpringerPlus* **2**, 1-7, 2013.

[26] M. DiCicco, L. Lucas, and Y. Matsuoka, Comparison of control strategies for an EMG controlled orthotic exoskeleton for the hand. in *Proc. IEEE Int. Conf. Robotics Automation*, New Orleans, LA, USA, Apr. 26- May 1 2004, pp. 1622-1627.

[27] A. I. M. Voorbij and L. P. A. Steenbekkers, The twisting force of aged consumers when opening a jar. *Appl. Ergon.* **33**, 105-109 (2002).

CHAPTER 5

OPTOELECTRONICALLY INNNERVATED SOFT PROSTHETIC HAND VIA STRETCHABLE OPTICAL WAVEGUIDES[§]

5.1 Introduction

Human hands serve not only prehensile functions, but also as powerful sensory organs [1]: we feel the world by sense of touch mostly through our hands. Hence, the loss of a hand means not only losing the ability of grasping and manipulation, but it also closes a door to sensory perception—hand amputees can no longer touch and feel through their fingers. Therefore, an ideal prosthetic hand should achieve dexterous manipulation as well as rich sensation [2]. Fortunately, many kinds of brain-computer interfaces (BCI) are being developed to realize the direct communication between human brain and external devices [3–5], and the effectiveness of using feedback sensation to enhance the functionality of prosthetic hands has been demonstrated by other researchers through patient-involved experiments [6, 7]. The work presented in this chapter is focused on increasing sensation in a soft and dexterous prosthetic hand.

Advanced prosthetic hands have realized dexterous motions by increasing the number of degree of freedom (DOF)[8], [9] or using under-actuated mechanisms [10–13]. Most of these hand prosthetic systems are powered by motors [2, 8, 10–13]. Recently,

[§] H. Zhao, K. O'Brien, S. Li and R. Shepherd, Optoelectronically innervated soft prosthetic hand via stretchable optical waveguides. *Science Robotics* **1.1** (2016): eaai7529.

fluidically powered soft actuators have shown their potential as prosthetics and orthotics [14–16] ; these devices, compared with motor-driven counterparts, are lighter, undergo continuous and more natural deformation with simple control inputs [17, 18], are easy to fabricate [14, 19] , and due to their liquid phase processing are more likely to be realized in mass production (e.g., replica molding, injection molding, rotational molding) [20, 21]. Very few soft prosthetics, however, have demonstrated equivalent sensing ability as motor-driven hand prosthetics, which many times achieve proprioceptive sensing through motor motion encoders [8, 10–13] and realize force sensing through multi-axial Force/Torque load cells [10, 12, 13], which are bulky and rigid. On the contrary, fluidically driven soft systems operate via stretching of their bodies at strains, $\epsilon = (L-L_0)/L_0 > 0.50$ [14, 19, 22]. Most existing sensors are incompatible with these large strains and, while excellent efforts are being made in the area of developing stretchable sensors for soft actuators [23–29], there is still an opportunity for reliable, easy to fabricate, safe, and chemically stable ones.

This chapter reports the first use of stretchable optical waveguides for strain sensing in a prosthetic hand. These photonic strain sensors are easy to fabricate, chemically inert, demonstrate low hysteresis and high precision in their output signals. As a demonstration of their potential, in this chapter I use them as curvature, elongation, and force sensors integrated into a fiber-reinforced soft prosthetic hand. I use this optoelectronically innervated prosthetic hand to conduct various active sensation experiments inspired by the capabilities of a real hand.

5.2 Stretchable sensors based on waveguides

In the early 1970s, Xerox Corporation patented an optical waveguide modulator by deforming an elastomeric cladding [30]. In the 1980s, elastomeric waveguides were used in strain sensing [31], tactile sensing [32], position sensing [33], acoustic sensing [34] and gas sensing [35]; however, the fabrication of those sensors usually required complex instruments and processes and could only be achieved by large corporations and national laboratories. Since the 1990s, due to newly available fabrication techniques (e.g., soft lithography [36]), elastomeric waveguides have been applied as innovative sensors in academic research [37, 38]. I have developed a class of these sensors, elastomeric optical waveguides, and applied them to prosthetics.

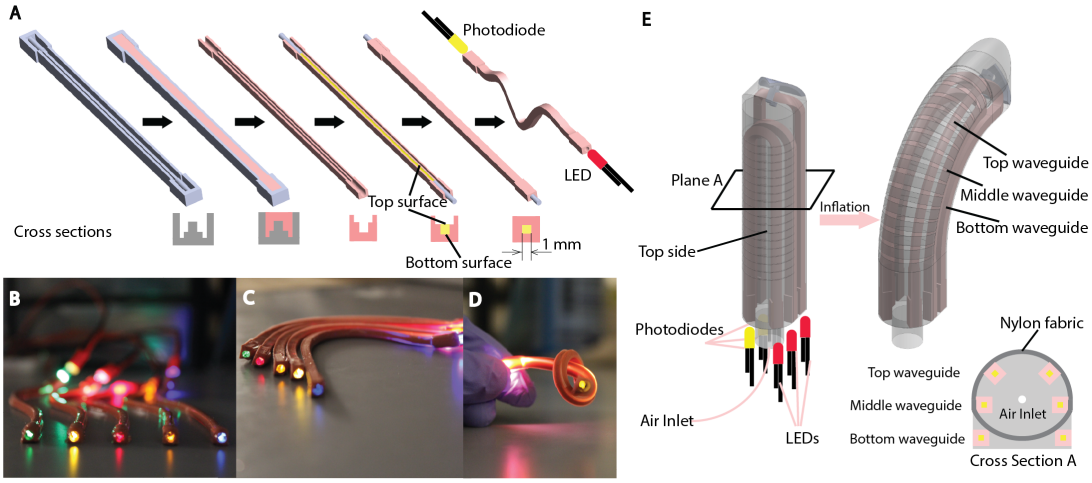

Figure 5.1 Stretchable waveguide fabrication and structure of the optoelectronically innervated soft finger. (a) Steps for fabricating a waveguide and the corresponding cross section for each step; (b) fabricated waveguides with assorted color LEDs inserted from one end in a sinuous shape; (c) waveguides in a curved shape; (d) waveguide in a knot; (e) schematic of a soft innervated finger in both unpowered state (left) and powered state (right) and its cross section (bottom right corner).

This waveguide is fabricated to be intentionally lossy—as light propagates through it, some radiates to the environment and the more it is deformed, the more light is lost.

We measure the light power loss of the waveguide through a photodetector to indicate its deformation. Specifically, the sensory waveguide is a step index multimode optical fiber composed of a high index of refraction core, n_{core} ~1.46, with cross sectional area A_{core} ~1 mm x 1 mm, clad with a lower n_{clad} ~1.40 elastomer of A_{clad} ~3 mm x 3 mm. To fabricate the stretchable waveguide, we use a four-step soft lithography process [39] (Figure 5.1(a)): (i) 3D print a mold for making the cladding, (ii) pour pre-elastomer for cladding into the mold and demold after curing, (iii) fill the cladding with the pre-elastomer of core material, and (iv) pour pre-elastomers of the cladding to enclose the core. We also cast two holes at each end of the waveguide to house the LED and photodetector (i.e., photodiode). Soft lithography ensures that all structures of the initial mold are replicated in the final waveguide without any detail loss, including surface roughness [40].

The core material of the waveguide is a transparent polyurethane rubber (Vytaflex 20; Smooth On, Inc.) with a refractive index of n_{core} =1.461 and a propagation loss of 2 dB/cm at a wavelength of 860 nm and the cladding material is a highly absorptive silicone composite (ELASTOSIL® M 4601 A/B; Wacker Chemie AG) with a refractive index of n_{clad} =1.389 and a propagation loss of 1,500 dB/cm at a wavelength of 860 nm. The optical properties for these two materials over a larger wavelength range (400 nm to 1,000 nm) are shown in Figure 5.8(a,b). Due to the relatively large difference in n for elastomers, the numerical aperture (NA=0.45 at 860 nm) ensures a large acceptance angle ((θ_{max}~26°) of light input and thus lowers the coupling difficulties for the LED and the photodetector at the extents of the waveguide.

The resulting waveguide is different from commercial ones for several reasons:

(i) It is highly compliant and stretchable. The core and cladding materials have ultimate elongations, ϵ_{ult} ~10 and ϵ_{ult} ~7, respectively, and elastic moduli (measured at 100% strain), *E'*~300 kPa and *E'*~400 kPa, respectively (Figure 5.9). The combination of high compliance and extensibility allows these waveguides to operate as bending, elongation, and pressure sensors for most situations a hand would typically encounter (e.g., pressing, touching, grasping).

(ii) The core material has a relatively large propagation loss as compared to ones used for fiberoptic communication. As our waveguides are applied to prosthetic hands for sensation, this relatively large propagation loss improves sensitivity during elongation while still allowing a detectable amount of light over the length scales typical of a human hand using a low-cost photodiode and a simple current amplifying circuit.

(iii) Our cladding material absorbs light at a rate of 1,500 dB/cm. This low index material not only serves as the cladding to ensure total internal reflection for light inside the waveguide, but also serves as the jacket to protect the core and forms the coupling house for LED and photodetector, preventing ambient light from altering the signal.

(iv) We 3D print the molds using a polyjet printer (Objet 30) for our optical waveguides. This fabrication process generates a surface roughness between the core and cladding of 6 nm (RMS, see Figure 5.10). This relatively rough interface causes

scattering and thus more loss of propagation, however, the design freedom of 3D printing allows for complex sensor shapes.

After the waveguides are fabricated, we cast three of them into a finger actuator using over-molding (Figure 5.1(e)). The body of the finger is made of silicone elastomer (Ecoflex 0030, Smooth On, Inc.), whose optical and mechanical properties are shown in Figure 5.8 and Figure 5.9. The three dimensional integration of the sensors and actuators means the waveguides are parts of the body and they will deform when the actuator does, serving as proprioceptive sensors.

5.3 Characterization of waveguide sensors

We define the output power of a waveguide with no bending, no elongation and no pressing deformation as the baseline power I_0. With the output power as I, the output power loss in decibels (dB) is then defined as:

$$a = 10\log_{10}(I_0/I) \qquad \text{(Equation 5.1)}$$

By this definition, the output power loss compared to the baseline is always 0; with increasing power $a<0$, and with decreasing power $a>0$.

To characterize the sensitivity of the waveguides during different deformation modes, we measured the output power of a length of stretchable waveguide during (i) elongation, (ii) bending, and (ii) pressing (see Figure 5.11 for characterization methods).

Elongation: For the elongation data (Figure 5.2(a)), we observed a highly linear response curve of power loss with strain. This linear curve can be derived from the Beer–Lambert law:

$$A = eLc \qquad \text{(Equation 5.2)}$$

Where A is absorbance, L is the path length, e is the absorptivity of the material and c is the concentration of chemical species in the medium that attenuate light. Assume constant e and c while stretching, A is proportional to L, and by definition of A,

$$A = \log_{10}(I_0/I) + b = a/10 + b \qquad \text{(Equation 5.3)}$$

where b is the baseline absorbance. Strain is defined as

$$\epsilon = (L - L_0)/L_0 \qquad \text{(Equation 5.4)}$$

So that

$$a = 10ecL_0\epsilon \qquad \text{(Equation 5.5)}$$

and $10ecL_0$ is a constant.

Experimental results using a L_0 = 100 mm waveguide yielded a linear, stretch dependent loss of ~2 dB/cm over $\Delta\epsilon$ ~ 0.85 using an LED (peak wavelength~875 nm, TSHA4400 from Vishay Intertechnology, Inc) and a photodiode (380 nm-1100 nm, SFH 229 from OSRAM Licht AG); using different input power, light frequency or photodetector parameters will alter this sensitivity. It is, therefore, important to calibrate the waveguides accordingly. In addition to linearity, the waveguide when

operating as a stretch sensor also shows high repeatability (see Figure 5.12(a) and Video 5.1), high precision and high signal-to-noise ratio (50-150, Figure 5.2, error bars indicate noise) over the tested range.

Bending: The waveguide we developed has anisotropic optical transmission properties (Figure 5.2(b)). The "top" of the waveguide core interface (indicated in Figure 5.1(a)) is atomically smooth, while the "bottom" core interface has an RMS roughness of 6 nm due to demolding from a 3D printed surface (Figure 5.10). The result of this anisotropy is that the signal output depends on the direction of bending: towards the top surface (i.e., top is in compression, bottom is in tension) leads to a signal rise followed by a drop in output power, while bending toward the bottom surface causes the output power to decrease monotonically. Using this difference, we can determine whether the sensor is being bent up or down. There is no anisotropy in bending side to side (although future versions could be programmed with this feature).

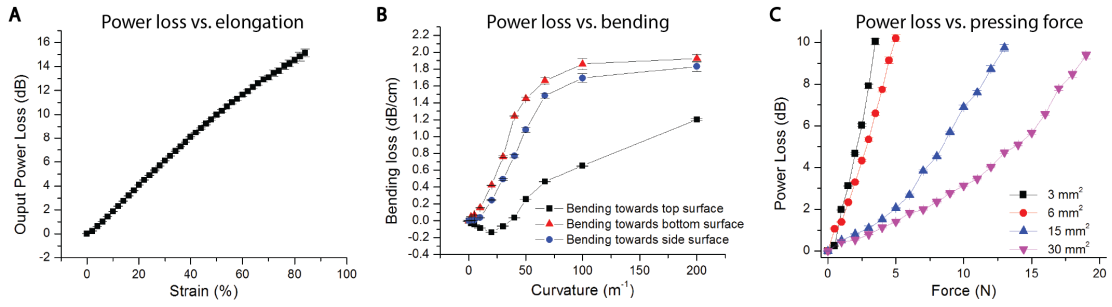

Figure 5.2 Characterization of waveguide sensor for: (a) pure elongation, (b) pure bending, and (c) pure pressing. (Error bars indicate standard errors from 20 cyclic tests of one waveguide sample.)

In addition to directional anisotropy, the optical transmission loss rate depends on curvature [41]. To characterize this dependence, we measured the power output during bending at uniform curvature up to $\kappa \sim 200$ m^{-1}. The output power loss vs. κ shows a linear trend in the medium curvature range of 20 – 70 m^{-1} and a sensitivity of 0.02 dB·m/cm. We note that, although the sensing profile is non-linear, it is highly repeatable and precise (Video 5.2), and thus easy to calibrate.

Pressing: Due to the low elastic moduli of our constituent elastomers, small forces exerted over the area of a fingertip can cause a large local deformation in the waveguide. We used this property to sense pressing, and tested the power output response to varying forces exerted externally. Our results show acute pressing (e.g., ΔA <6 mm^2) causes a linear response in output power; however, blunt pressing (e.g., ΔA >15 mm^2) results in a non-linear response (Figure 5.2(c)). This results means we can change the sensitivity of the waveguide by changing its dimensions to fit the working range of a particular application. The repeatability of pressing sensation is demonstrated in Video 5.3 and Figure 5.12(b).

This compliant, stretchable waveguide shares the same material library (including silicone elastomers, polyurethane elastomers, tough hydrogels, etc.) as many commonly developed soft robots [19, 21, 42]. It shows high linearity to elongation, bending and local pressing and is highly repeatable and precise. To demonstrate the capability of these waveguides for imparting sensation to soft robots, we incorporated them into the fingers of a soft prosthetic hand.

5.4 Innervated prosthetic hand design

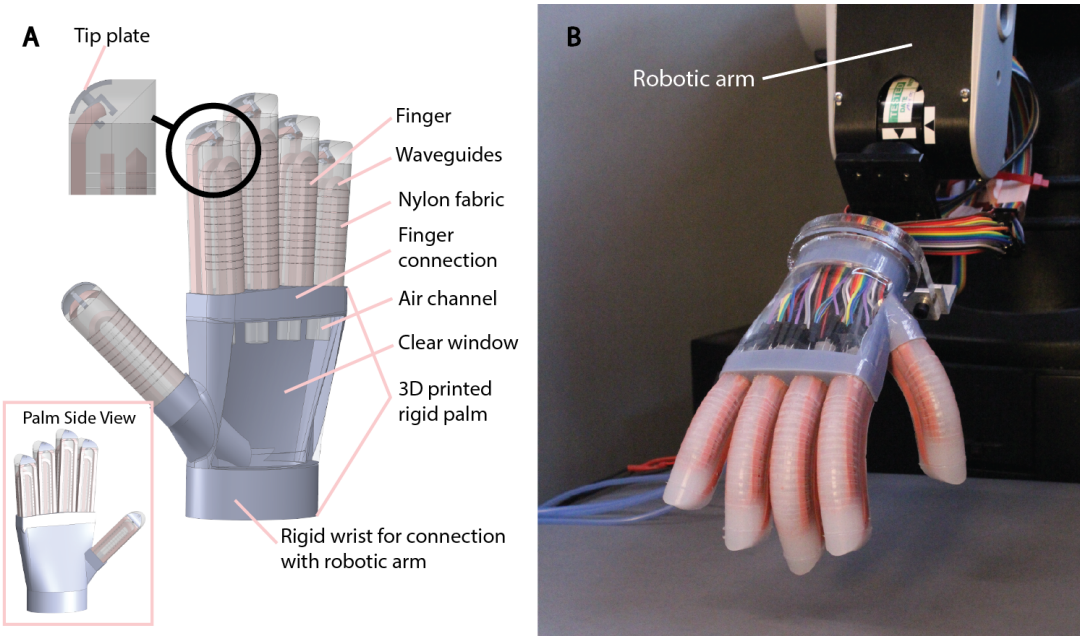

Figure 5.3 Innervated prosthetic hand. (a) Schematic of hand structure and components; (b) image of the fabricated hand mounted on a robotic arm with each finger actuated at ΔP =100 kPa.

Our prosthetic hand is composed of four pneumatically actuated soft fingers and a thumb mounted onto a 3D-printed rigid palm (Figure 5.3(a)). Each digit is a hollow silicone tube (outer diameter = 18 mm, inner diameter = 1 mm; Figure 5.1(a)) with fibers patterned into the elastomer. Compressed air enters each finger through their hollow cores and the inflation pressure causes the fingers to bend and the hand to grasp.

Actuation: We patterned the fabric in the actuator to cause a finger-like motion upon pressurization. The nylon fabric is laser cut to be solid on one side and have slits on the other. This design is based on a mechanical model we established previously, where constraining circumferential stretching during inflation causes more axial

actuation and the strain-limiting portion on one side of the elastomeric structure causes bending around that layer [16]. The slits allow for circumferential constraint while still allowing the gaps in between to stretch for actuation. Figure 5.1(e) shows that the finger curves in between the slits, yet there is negligible circumferential bulging. On the palm side of the actuators (i.e., the neutral bending plane), there was no elongation due to the solid sheet of nylon.

Control: For our demonstration, we used a single air supply for all four fingers and thumb, and we used two solenoid valves (X-valve, Parker Hannifin Corporation) for each to control actuation—one for allowing flow into a finger (actuate) and the other to exhaust it (de-actuate). We controlled the on/off state of each valve to determine the pressure inside each finger and, thus, its motion. Though we have demonstrated sophisticated control over actuators previously [16, 43], we chose "open loop" in this paper to focus on the importance of the stretchable waveguides for active sensation. To test the capabilities of the prosthetic hand, we affixed it to the end joint of a 5-DOF robotic arm (CRS CataLyst Express; Figure 5.3(b)).

Sensing: To impart the sense of touch to the soft prosthetic, we embedded the photonic strain sensors throughout the actuator membranes. In our demonstration, we incorporated three waveguides into each finger, where each is bent into a U-shape (towards the gravity-driven interface) so that LEDs can transmit light through the entirety of the actuators and the photodetectors can sense it on the other side (Figure 5.1(e)). The photonic sensor located at the top of the actuator experiences the largest axial strain and thus the largest sensitivity to the bending motion. We placed the

second sensor in the middle plane of the finger, which has medium axial strain, but also relays information about internal pressure.

The final waveguide serves as a touch sensor for the fingertip of the prosthetic hand; we achieve this isolated function by placing it at the neutral bending plane, where there is no axial strain. This photonic sensor is different from the other two sensors because it is longer and extends to the tip of the finger. The tip of the finger experiences no deformation while inflating and is used solely for detecting contact force when touching objects. In order to tune the external force sensing range of our prosthetic hand's fingertips, we integrated a stiff plate (ΔA ~ 2 x 3 mm^2) at the fingertips in contact with the waveguide to enhance the sensitivity (Figure 5.3(a)). This force amplifying structure directly transmits external tip force to the waveguide.

Video 5.4 demonstrates the isolated functions of three waveguides in one finger: (i) when we pressed the finger tip, the bottom waveguide responded and the other two did not; (ii) when we inflated the finger, the middle and top waveguide showed responses immediately and the bottom waveguide did not. To distinguish the different functions of the middle waveguide and top waveguide, we kept the inflation pressure constant while we bent the finger back to straight; we observed a significant signal drop (50%) for the top waveguide and a negligible signal drop (10%) for the middle waveguide. When the finger is deflated, there is a significant signal drop (90%) for the middle waveguide. In the following section, we use these differences for haptic sensation.

5.5 Active haptic sensing experiments

Our soft prosthetic hand is a multifunctional one with both powerful motor capabilities (Figure 5.4(a-c)) and versatile sensory ones (Fig 5.4(d-f)). Each digit of the hand is capable of both proprioception (sensing internal pressure and active bending) and exteroception (sensing passive bending and external force at the fingertip). To demonstrate these capabilities, we designed three experiments inspired by common tasks of the human hand including: detecting shape and texture, probing softness, and object recognition.

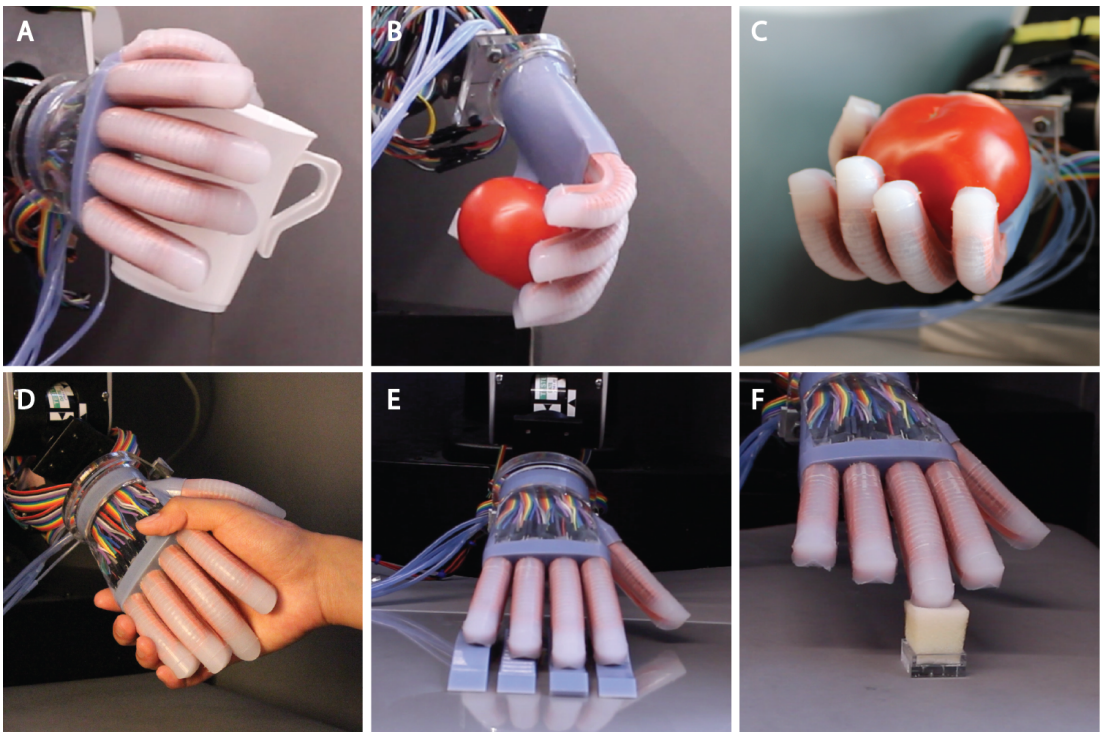

Figure 5.4 Capabilities of the hand. (a) Holding a coffee mug; (b) grasping a tomato with the palm facing down and (c) palm facing up; (d) shaking a human hand; (e) lateral scanning over surfaces to detect roughness and shape; and (f) probing the softness of a soft sponge using the middle finger.

5.5.1 Lateral scanning to detect shape and texture

The most commonly used exploratory procedure for detecting roughness and shape of a surface by a human hand is lateral scanning[44]. Using our robotic arm, we guided the hand to conduct lateral scans at a fixed height over several surfaces to distinguish their shape and texture (Video 5.5). We oriented the palm of the hand at a shallow angle (20°) with the surface so that each fingertip was touching the surface. When performing lateral scanning, the soft finger can be expressed as a spring and the height of the point it is touching changes the states of the spring—both compression distance, ΔH, and contact force, ΔF. As the fingers moved along the contoured surfaces, the bottom waveguide measured ΔF as it changed with surface height, ΔH. Increasing the stiffness of the finger also increases its sensitivity, $k = \Delta F / \Delta H$. As actuation pressure increases, the measurement sensitivity increases, but this increased pressure also causes the hand to close. With an actuator pressure of ΔP=100 kPa (~15 psi), we were able to find a suitable balance between sensitivity and an open hand shape.

Using this method, we tested the ability of the fingers to topographically map seven different 3D printed surfaces (Figure 5.5(a), left). After a simple calibration using an inclined plane with known height and angle, we reconstructed the height profile of the seven surfaces (Figure 5.5(a), right). From this data, we observed that our hand could distinguish curves as small as 5 m^{-1} and roughness on the order of 100 microns. We also found that our hand can be used to reconstruct the shape of simple objects such as a computer mouse (Figure 5.5(c,d)) including the scroll wheel and the click of the mouse buttons. Although the sensitivity of our hand is far from that of a human's,

which can sense roughness on the scale of nanometers [45], we have demonstrated a promising system for replicating shape and texture detection using stretchable, optical sensors with a soft hand.

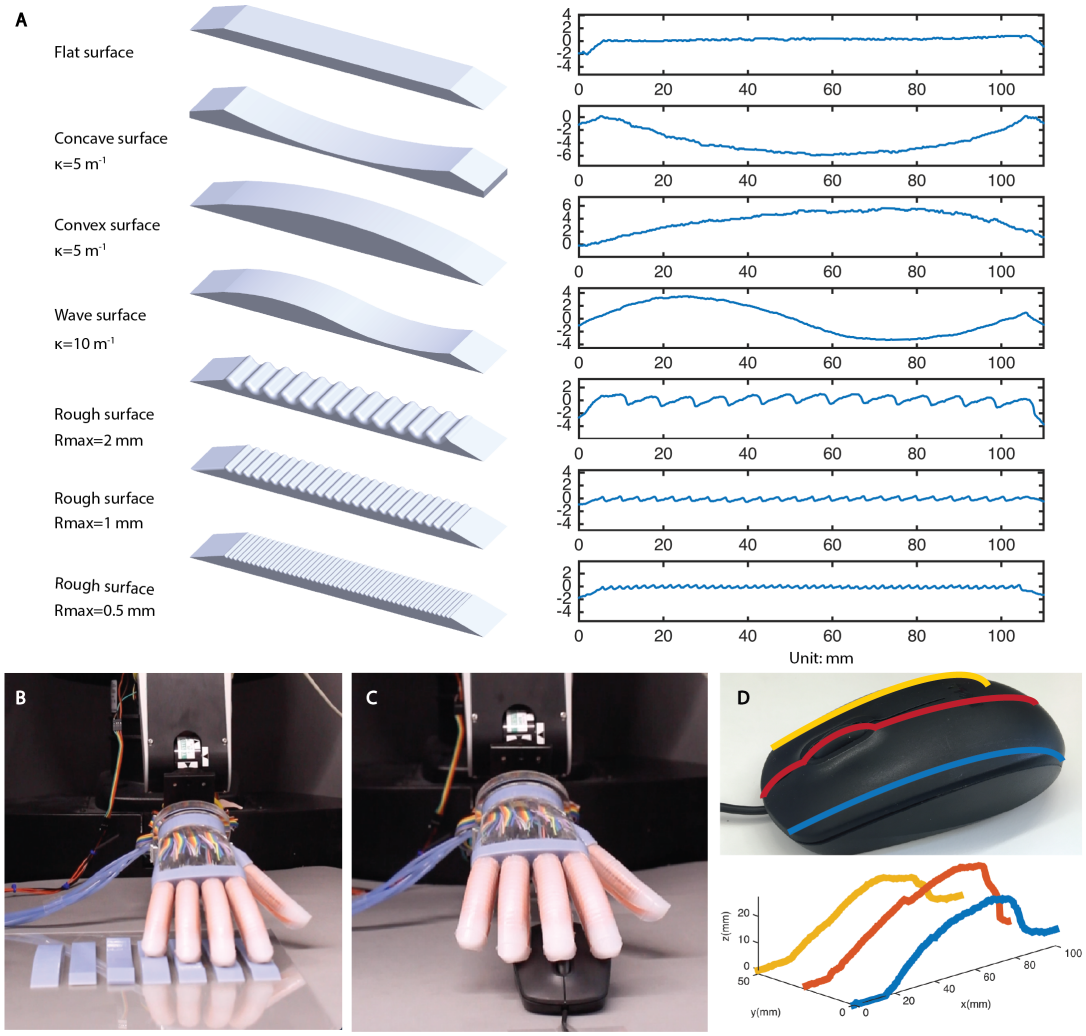

Figure 5.5 Shape and texture detection. (a) (left) Seven surfaces of different shape and roughness and (right) the reconstructed surfaces by the hand; (b) picture of the lateral scanning for (A) using bottom waveguide of each digit; (c) lateral scanning of a computer mouse; (d) mouse and the reconstructed shape.

5.5.2 Softness Detection

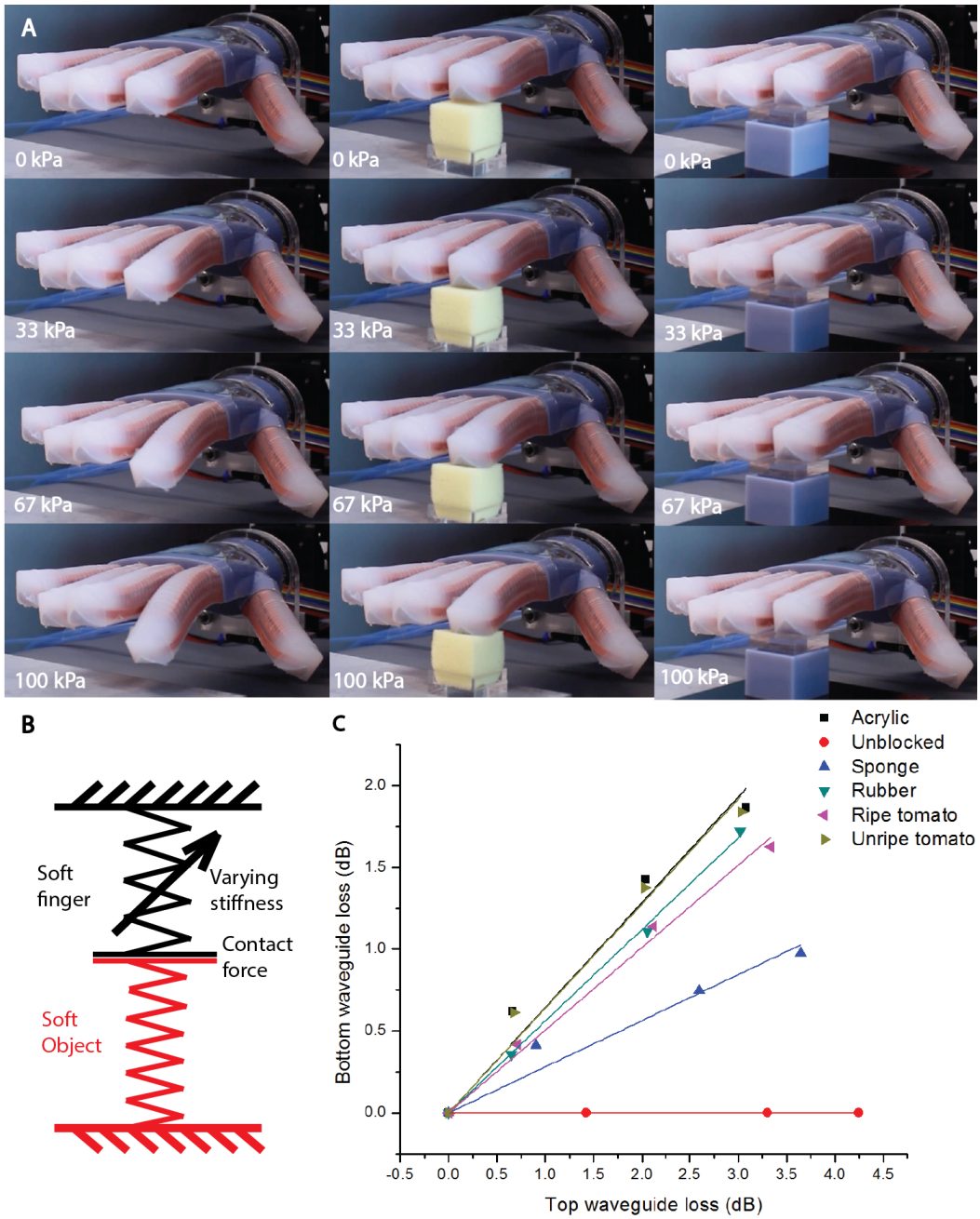

Figure 5.6 Softness detection. (a) States of the softness detection at different air pressures for unblocked (right), sponge (middle) and acrylic (right); (b) model of softness detection; (c) force-curvature curves for different objects detected from bottom and top waveguides of index.

Along with shape and texture, our hands can also detect the softness of objects. As the relationship between ΔH and ΔF is used in most forms of mechanical testing, we applied this information to measuring the softness of objects. To demonstrate this ability, we used our prosthetic hand to measure the softness of an unblocked (control) state along with five common materials and objects: acrylic, polyurethane sponge, silicone rubber, a ripe tomato, and an unripe tomato. We measured their softness by positioning the tip of an unactuated (0 kPa) finger so that it was barely touching the top of the object to be measured. We took readings of the tip force and the degree of bending in the unactuated state as well as at varying internal pressures, indicated by the bottom waveguide power loss and the top waveguide power loss, respectively (Video 5.6).

Figure 5.6(a) shows the index finger measuring softness of the unblocked state, sponge, and acrylic. The system, consisting of the finger and the material being probed, can be modeled as a two-spring system (Figure 5.6(b)). By varying the stiffness of the finger (via the internal pressure, which is monitored by the middle waveguide power loss), we were able to generate a stress-strain curve for each of the materials we measured (Figure 5.6(c)): the loss in the bottom waveguide is proportional to the contact force (thus stress) on the object while the loss in the top waveguide is proportional to its deformation (thus strain). We measured four states (0 kPa, 33 kPa, 67 kPa and 100 kPa) for each object and fit them into a linear curve. The slope of these fitted lines is the indicator we picked for the softness of the objects (larger slopes indicate harder objects). As expected, this data shows the objects decreasing in softness in the following order: unblocked, sponge, rubber, ripe tomato,

unripe tomato, acrylic. Note that our hand can barely distinguish the difference in softness between an unripe tomato and the acrylic. This issue is mainly because of the large contrast between the object's and the finger's stiffness: higher internal pressures would be required to achieve detectable position changes in harder objects. This result is similar to that of human's process of detecting softness: we apply a large force to detect a hard object and a gentle press for a soft one.

5.5.3 Object Recognition

In our final demonstration, we combined shape and softness measurement to select the ripest (softest) among a group of three tomatoes aligned in a row. First, we used our lateral-scanning, shape-reconstruction method to determine the shape and location of three tomatoes (Figure 5.7(a)). After determining their location, we positioned the index finger to measure their softness (Figure 5.7(b)). As shown in Video 5.7, our hand was able to locate and select the ripe (red) tomato based upon its softness. Though there is seemingly little difference in output signal from Tomato 2 to Tomato 3, we were still able to determine the ripe tomato was softer (larger top waveguide loss and smaller bottom waveguide loss). During the process of scanning and probing, we caused a human-like gentle motion by our soft prosthetic hand to avoid the risk of destroying the tomatoes.

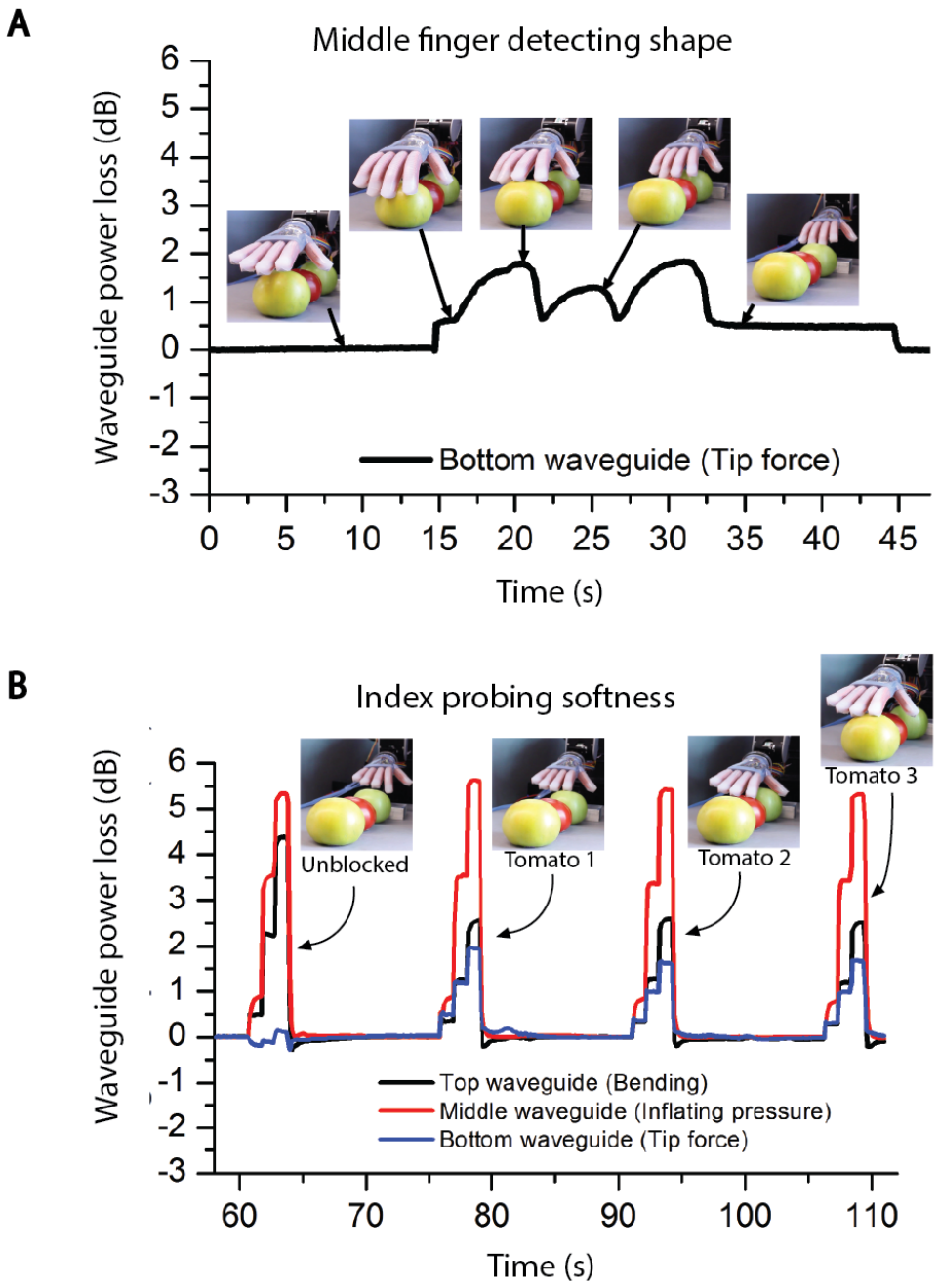

Figure 5.7 Waveguide power loss during the process of detecting shape and probing softness. (a) Process of middle finger detecting shape using its bottom waveguide: actuate fingers, scan above tomatoes, de-actuate fingers. (b) Process of index finger probing softness using three waveguides: press unblocked, press tomato 1 (unripe), press tomato 2 (ripe), and press tomato 3 (unripe).

5.6 Conclusions and Discussions

In this chapter, I presented a soft prosthetic hand with rich sensation realized via stretchable optical waveguides. My work is the combination and extension of several developing areas in both material science and robotics: 3D printing, soft lithography, and soft robotics. This sensor demonstrates excellent precision (signal-to-noise ratio > 50) and stretchability ($\Delta\epsilon$ ~8 5% strain). We believe the easy fabrication, low cost, chemical compatibility, and high repeatability of the developed stretchable waveguide sensors will benefit the field of robotics (e.g., soft robot bodies and skins for hard ones). In addition, I demonstrated that soft prosthetic hands could not only perform dexterous manipulation, but also achieve various haptic sensing functions through simple innervation and control.

My current prosthetic hand prototype, still in its early stage, shows many capabilities, yet still has many aspects that can be improved upon. First, sensory density can be greatly increased. As the waveguide sensors and the body of the actuator share the same material library, more sensors could be incorporated into the actuators, or completely replace the body of the actuators, to achieve higher information density for both proprio- and extero-ception. The sensitivity can also be increased by using a larger power range from the LED (from the baseline power to ambient light power), by using high-power laser diodes, and increasing the pressure range of the soft actuators (within the material's elasticity range) to press on objects with more force. In essence, the waveguide sensor I developed is a strain sensor based on geometric change; therefore, by 3D printing more complex sensor shapes, I can use them for

more than bending, pressure, and press sensing (e.g., damage detection). Finally, although I positioned these sensors in different places on the actuator, we still observed signal coupling. When more sensors are incorporated to extract denser information, the output signals will be increasingly coupled and it will be difficult to calibrate the relationship between input and output signals; however, because the outputs of waveguide sensors are precise and repeatable, by collecting large quantities of data, I could use machine-learning techniques to map inputs to outputs (regression) or perform more subtle object recognition (classification) (46).

5.7 Materials and Methods

Objectives and design of the study. Our objective is to prove that optical sensors can be co-integrated into soft actuators and provide high quality sensory capabilities. We designed an elastomeric optical waveguide that is highly stretchable, chemically stable, easy to fabricate, and also exhibits high precision in signal output. We chose the combination of 3D printing and soft lithography as the fabrication method because of its large design freedom and proven ability to replicate shapes in soft materials with high precision[18]. We designed each finger of our prosthetic hand to be soft to make use of their intrinsic compliance so that we can implement most of our experiments by open-loop control. Importantly, the softness of the finger actuators allows external forces to transmit to the internal structure and embedded sensors.

Fabrication of waveguides. Molds for cladding were 3D printed using an Objet 3D printer in glossy mode. The mold was put in oven at 60 °C for 4 hours. Mold release was applied on the surface of the mold. ELASTOSIL M4601 part A and part B were

mixed at a ratio of 1:1 using a planetary centrifugal mixer at speed of 2000 rpm for 30 s and the mixed pre-elastomer was poured into the mold for cladding and put in oven at 60 °C for 1 h for curing. The cured piece was demolded from the mold and laid flat on a tray. Vytaflex 20 part A and part B were mixed at a ratio of 1:1 using planetary centrifugal mixer at speed of 2000 rpm for 1 min and the mixed pre-elastomer was poured into the cured cladding piece within 10 min. The cladding with the uncured core was put on a hot plate at 70 °C for 1h. After the core was cured, pre-elastomer of M4601 (prepared in the same way as the cladding piece) was poured onto the top of the core and cured in oven.

Fabrication of the innervated finger. Two shorter waveguides and one longer one were prepared in advance. Linear slits were cut into a rectangular piece of Nylon fabric (see Figure 5.14). Three waveguides, nylon fabric and the finger molds (Figure 5.13) were assembled together and the mold cap was put on. Pre-elastomer of Ecoflex 30 was poured into the mold. Finally, a thin steel spring wire was inserted into the mold through a thin hole on the mold cap. The assembly was put in oven at 60 °C for 30 min. The assembly was disassembled, the steel wire was taken off and the cured finger was demolded. A tube was inserted from the end hole and a clamp was used to fasten the air inlet.

Characterization of materials. The refractive index of materials was measured using Woollam Spectroscopic Ellipsometer with 30 mm x 30 mm x 3 mm samples. The absorbance of materials was measured using Shimadzu UV-Vis-NIR Spectrometer. The mechanical tests were conducted on Zwick tensile test machine. Surface

roughness was measured using MicroXAM optical profilometer. Three separate samples were used to conduct each characterization.

Characterization methods for waveguide sensors. Elongation: we fixed two ends of the waveguide onto the two jaws of a bench vise and precisely rotated the screws to stretch the waveguide to different strains, and at the same time, we recorded the power loss (Figure 5.11(a)). Bending: we manipulated the waveguide to conform to laser cut acrylic arcs and recorded the corresponding power loss (Figure 5.11(b)). Pressing: we fixed the ends of the waveguide and laid it flat on a scale. We then put a plate with known width onto the waveguide, and placed different weights onto the plate to record the power loss. This process was repeated with plates of varying width (Figure 5.11(c)). Only one sample was used for each characterization and each signal was collected 20 times to get the mean and standard deviation.

Data acquisition and processing. We used an LED as the light source and photodetector as the light sensor for our optical waveguides. Using a current to voltage (I/V) converter circuit (Figure 5.15), we were able to detect the light power received at the photodetector. Due to slight variations in manufacturing, some waveguides had higher intrinsic power loss than others. We selected the resistance values for our LED and I/V converter circuits to adjust for these differences in transmissivity between waveguides. With appropriate resistor values selected (Table 5.1), each waveguide sensor produced a maximum voltage of approximately 5V. By measuring the voltage, we were able to determine the power loss of the sensors when stretched, bent, or touched. Capacitance in the I/V converter circuit was chosen to be 4,700 pF to ensure

low noise and fast speed. We measured the output voltage of our circuits using 15 analog pins of an Arduino (Arduino MEGA 2560) Microcontroller, and used its serial port with a baud rate of 9600 to transmit the data to a computer. This data was received through MATLAB R2016, for further processing and plotting. Our sampling frequency was approximately 60 Hz for each of the 15 sensor channels.

5.8 Supplementary Materials

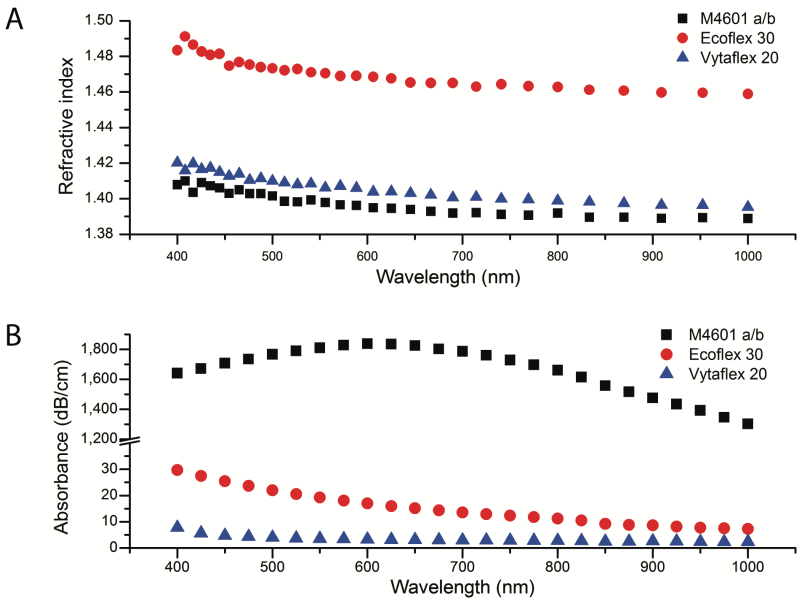

Figure 5.8 Optical properties of M4601 a/b, Ecoflex 30 and Vytaflex 20. (A) Refractive index over 400 nm to 1,000 nm; (B) Absorbance over 400 nm to 1,000 nm.

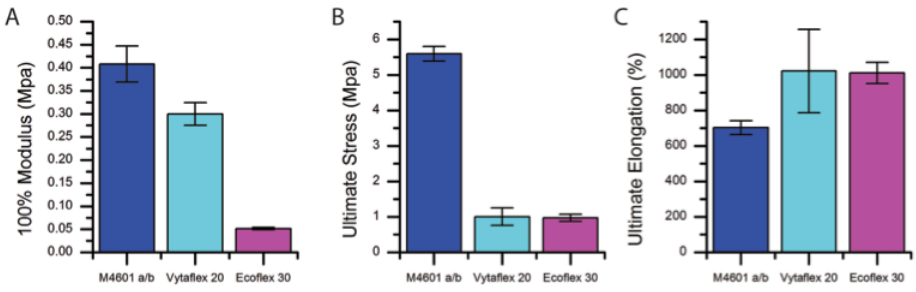

Figure 5.9 Mechanical Properties of M4601, Ecoflex 30 and Vytaflex 20. (A) 100% elastic modulus; (B) Ultimate stress; (C) Ultimate elongation.

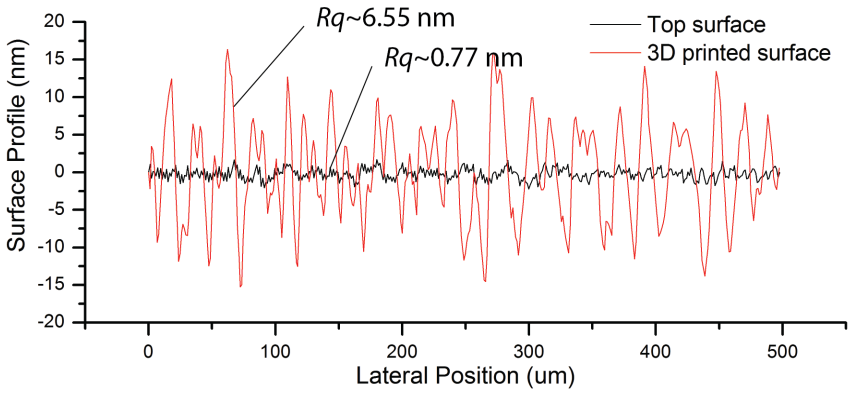

Figure 5.10 Surface profile of waveguide core/cladding interfaces.

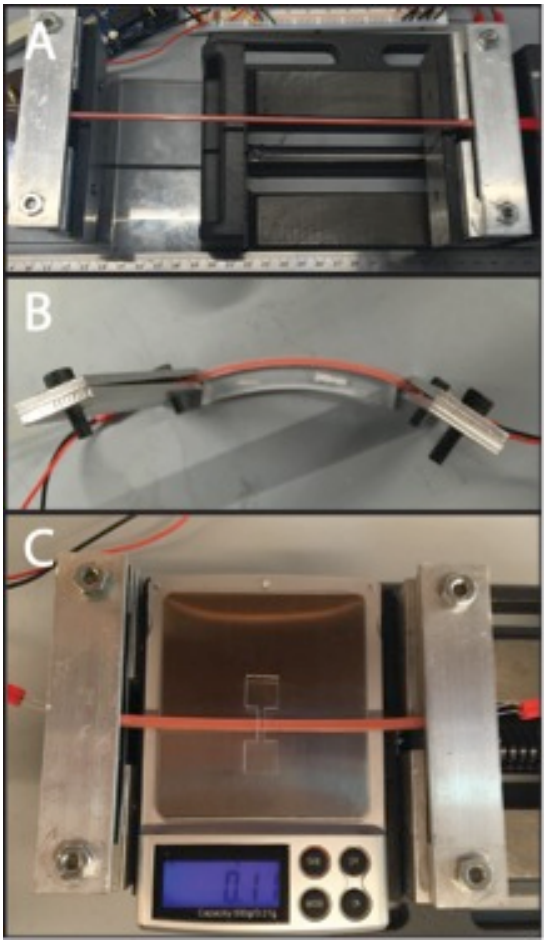

Figure 5.11 Characterization setups. (A) Elongation; (B) Bending; (C) Pressing.

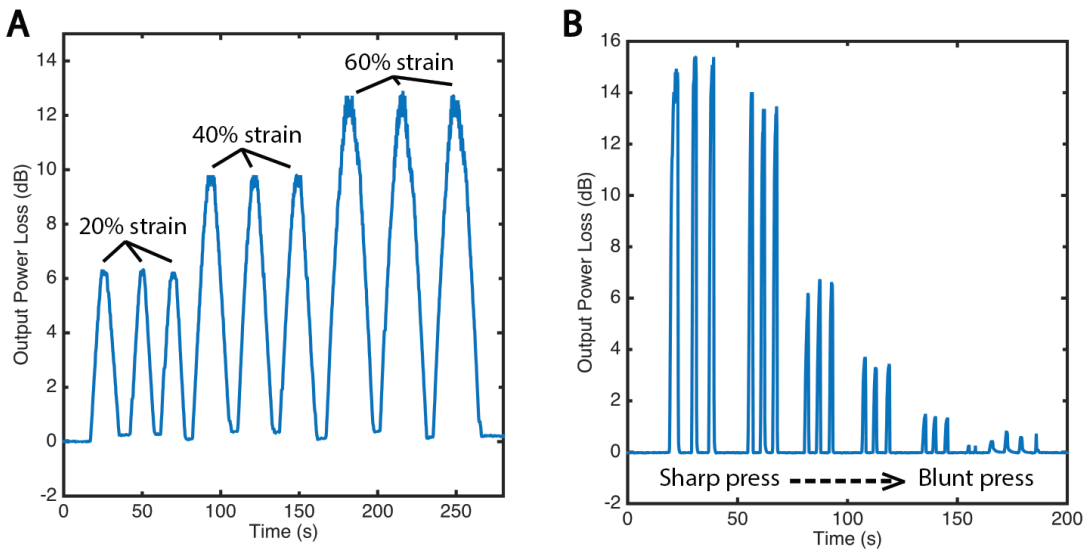

Figure 5.12 Repeatability tests. (A) Repeated elongation tests for a waveguide stretched to 20%, 40% and 60% of its original length; (B) Repeated pressing tests for a waveguide being pressed to 5 N through plates of different areas.

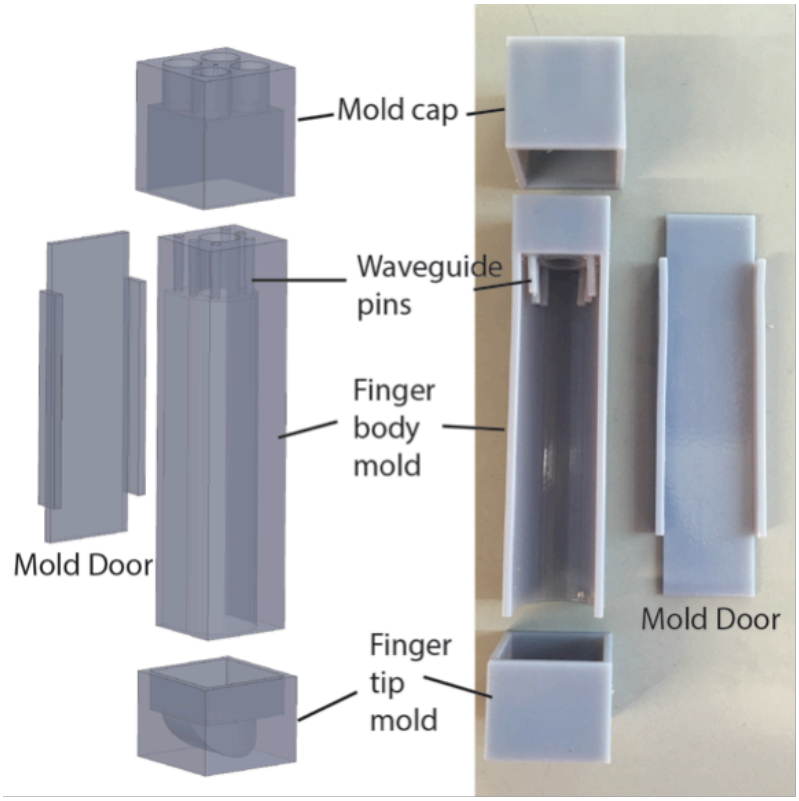

Figure 5.13 Mold design for the middle finger.

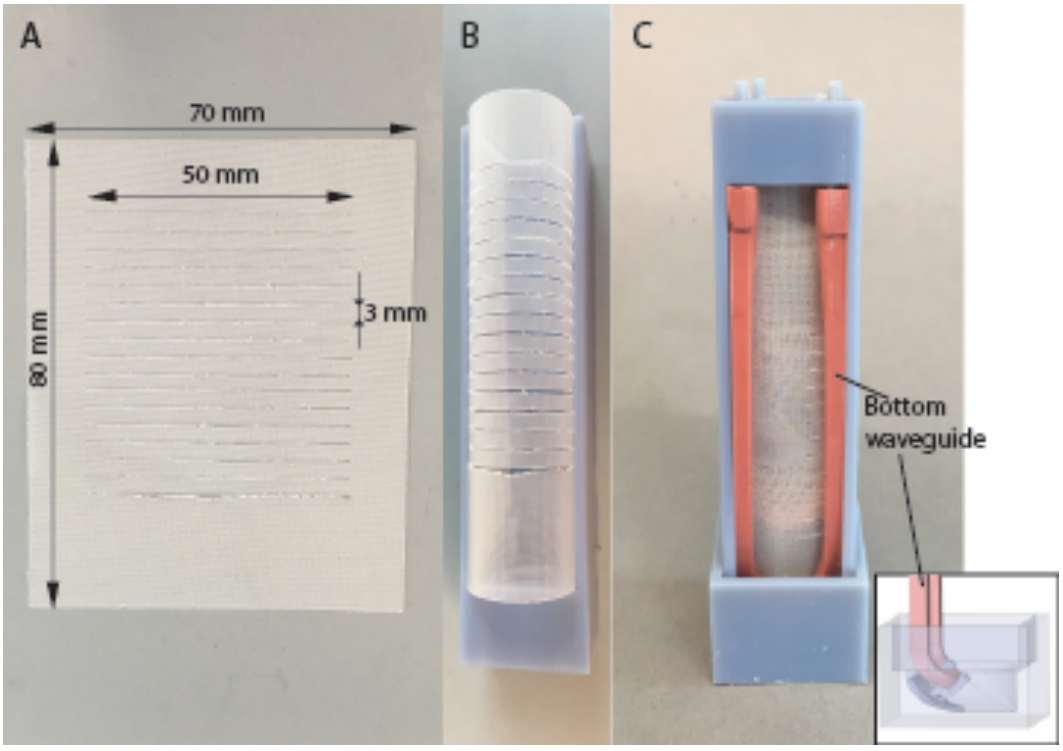

Figure 5.14 Nylon fabric and mold assembly. (A) Cut nylon fabric; (B) Rolled nylon fabric; (C) Waveguides and nylon fabric assembled into finger mold.

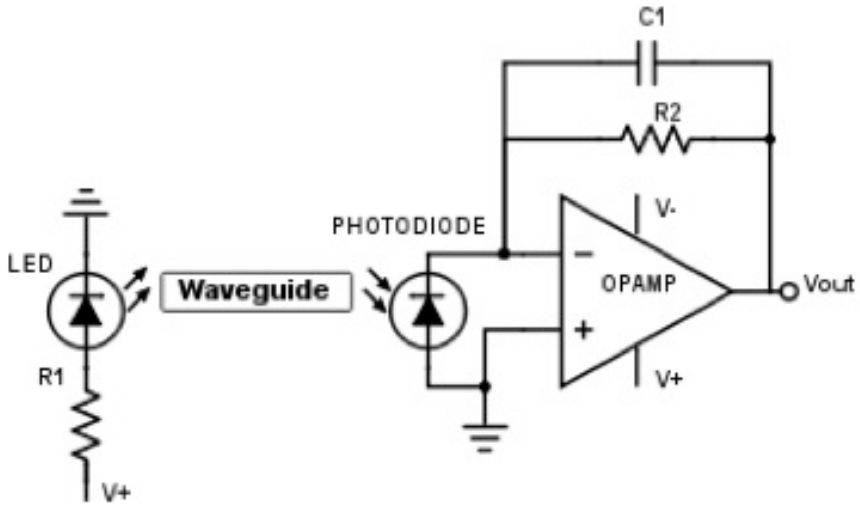

Figure 5.15 Circuit for powering LED and amplifying photodiode current.

Table 5.1 Resistors, capacitors used in LED-photodiode circuits for waveguide

Finger	Waveguide	$R_1(\Omega)$	$R_2(M\Omega)$	$C_1(pF)$
Index	Top waveguide	220	1	4700
	Middle waveguide	220	1	4700
	Bottom waveguide	220	2	4700
Middle	Top waveguide	100	2	4700
	Middle waveguide	100	2	4700
	Bottom waveguide	100	2	4700
Ring	Top waveguide	220	2	4700
	Middle waveguide	220	2	4700
	Bottom waveguide	47	2	4700
Pinky	Top waveguide	100	1	4700
	Middle waveguide	220	1	4700
	Bottom waveguide	100	1	4700
Thumb	Top waveguide	100	2	4700
	Middle waveguide	100	2	4700
	Bottom waveguide	100	1	4700

REFERENCES

[1] L. A. Jones, S. J. Lederman, Human Hand Function (Oxford Univ. Press, 2006).

[2] M. C. Carrozza, S. Micera, B. Massa, M. Zecca, R. Lazzarini, N. Canelli, P. Dario, The development of a novel prosthetic hand - Ongoing research and preliminary results. *IEEE/ASME Trans. Mechatronics*. **7**, 108–114 (2002).

[3] M. A. Lebedev, M. A. L. Nicolelis, Brain-machine interfaces: Past, present and future. *Trends Neurosci*. **29**, 536–546 (2006).

[4] P. M. Rossini, S. Micera, A. Benvenuto, J. Carpaneto, G. Cavallo, L. Citi, C. Cipriani, L. Denaro, V. Denaro, G. Di Pino, F. Ferreri, E. Guglielmelli, K. Hoffmann, S. Raspopovic, J. Rigosa, L. Rossini, M. Tombini, P. Dario, Double nerve intraneural interface implant on a human amputee for robotic hand control. *Clin. Neurophysiol.* **121**, 777–783 (2010).

[5] J. A. Berg, F. V Tenore, L. Jessica, R. J. Vogelstein, S. J. Bensmaia, Restoring the sense of touch with a prosthetic hand through a brain interface. *Proc. Natl. Acad. Sci. U. S. A.* **111**, 875–875 (2014).

[6] G. S. Dhillon, K. W. Horch, Direct neural sensory feedback and control of a prosthetic arm. *IEEE Trans. Neural Syst. Rehabil. Eng.* **13**, 468–472 (2005).

[7] S. Raspopovic, M. Capogrosso, F. M. Petrini, M. Bonizzato, J. Rigosa, G. Di Pino, M. Controzzi, T. Boretius, E. Fernandez, G. Granata, C. M. Oddo, A. L. Ciancio, C. Cipriani, M. C. Carrozza, W. Jensen, E. Guglielmelli, T. Stieglitz, P. M. Rossini, S. Micera, Restoring natural sensory feedback in realtime bidirectional hand prostheses. *Sci. Transl. Med.* **6**, 222 (2014).

[8] T. Mouri, H. Kawasaki, K. Yoshikawa, J. Takai, S. Ito, Antrhopomorphic robot hand: Gifu hand II, in *Proceedings of the 2002 International Conference on Control, Automation and Systems*, 16 to 19 October 2002, Jeonbuk, Korea, pp. 1288-1293.

[9] F. Röthling, R. Haschke, J. J. Steil, H. Ritter, Platform portable anthropomorphic grasping with the bielefeld 20-DOF shadow and 9-DOF TUM hand, in *Proceedings of the 2007 IEEE International Conference on Intelligent Robots and Systems*, 29 October to 2 November 2007, San Diego, CA, pp. 2951–2956.

[10] M. C. Carrozza, G. Cappiello, S. Micera, B. B. Edin, L. Beccai, C. Cipriani, Design of a cybernetic hand for perception and action. *Biol. Cybern.* **95**, 629–644 (2006).

[11] A. D. Deshpande, Z. Xu, M. J. Vande Weghe, B. H. Brown, J. Ko, L. Y. Chang, D. D. Wilkinson, S. M. Bidic, Y. Matsuoka, Mechanisms of the anatomically correct testbed hand. *IEEE/ASME Trans. Mechatronics.* **18**, 238-250 (2013).

[12] A. M. Dollar, R. D. Howe, The highly adaptive SDM hand: Design and performance evaluation. *Int. J. Robot. Res.* **29**, 585–597 (2010).

[13] M. G. Catalano, G. Grioli, E. Farnioli, A. Serio, C. Piazza, A. Bicchi, Adaptive synergies for the design and control of the Pisa/IIT SoftHand. *Int. J. Robot. Res.* **33**, 768–782 (2014).

[14] R. Deimel, O. Brock, A novel type of compliant and underactuated robotic hand for dexterous grasping. *Int. J. Robot. Res.* **35**, 161–185 (2016).

[15] P. Polygerinos, K. Galloway, S. Sanan, M. Herman, C. J. Walsh, EMG controlled soft robotic glove for assistance during activities of daily living. in *Proceedings of the 2015 IEEE International Conference on Rehabilitation Robotics,* 11 to 14 August 2015, Singapore, pp. 55–60.

[16] H. Zhao, J. Jalving, R. Huang, R. Knepper, A. Ruina, R. Shepherd, A helping hand: Soft orthosis with integrated optical strain sensors and EMG control. *IEEE Robot. Autom. Mag.* **23**, 55-64 (2016).

[17] A. Stilli, H. A. Wurdemann, K. Althoefer, Shrinkable, stiffness-controlled soft manipulator based on a bio-inspired antagonistic actuation principle. in *Proceedings of the 2014 IEEE/RSJ International Conference on Intelligent Robots and Systems,* 14 to 18 September 2014, Chicago, IL, pp. 2476–2481.

[18] R. F. Shepherd, F. Illievski, W. Choi, S. A. Morin, A. A. Stokes, A. D. Mazzeo, X. Chen, M. Wang, G. M. Whitesides, Multigait soft robot. *Proc. Natl. Acad. Sci. U. S. A.* **108**, 20400–20403 (2011).

[19] F. Ilievski, A. D. Mazzeo, R. F. Shepherd, X. Chen, G. M. Whitesides, Soft robotics for chemists. *Angew. Chemie - Int. Ed.* **50**, 1890–1895 (2011).

[20] H. Zhao, Y. Li, A. Elsamadisi, R. Shepherd, Scalable manufacturing of high force wearable soft actuators. *Extrem. Mech. Lett.* **3**, 89–104 (2015).

[21] A. D. Marchese, R. K. Katzschmann, D. Rus, A recipe for soft fluidic elastomer robots. *Soft Robot.* **2**, 7–25 (2015).

[22] B. N. Peele, T. J. Wallin, H. Zhao, R. F. Shepherd, 3D printing antagonistic systems of artificial muscle using projection stereolithography. *Bioinspir. Biomim.* **10**, 55003 (2015).

[23] S. S. Robinson, K. W. O'brien, H. Zhao, B. N. Peele, C. M. Larson, B. C. Mac Murray, I. M. Van Meerbeek, S. N. Dunham, R. F. Shepherd, Integrated soft sensors and elastomeric actuators for tactile machines with kinesthetic sense. *Extrem. Mech. Lett.* **5**, 47–53 (2015).

[24] C. Larson, B. Peele, S. Li, S. Robinson, M. Totaro, L. Beccai, B. Mazzolai, R. Shepherd, Highly stretchable electroluminescent skin for optical signaling and tactile sensing. *Science* **351**, 1071–1074 (2016).

[25] M. Amjadi, K.-U. Kyung, I. Park, M. Sitti, Stretchable, skin-mountable, and wearable strain sensors and their potential applications: A review. *Adv. Funct. Mater.* **26**, 1678–1698 (2016).

[26] C. To, T. L. Hellebrekers, Y.-L. Park, Highly stretchable optical sensors for pressure, strain, and curvature measurement. in *Proceedings of the 2015 IEEE International Conference on Intelligent Robots and Systems*, 28 September to 2 October 2015, Hamburg, Germany, pp. 5898–5903.

[27] F. L. Hammond, Y. Menguc, R. J. Wood, Toward a modular soft sensor-embedded glove for human hand motion and tactile pressure measurement. in *Proceedings of the 2014 IEEE/RSJ International Conference on Intelligent Robots and Systems*, 14 to 18 September 2014, Chicago, IL, pp. 4000–4007.

[28] L. P. Jentoft, A. M. Dollar, C. R. Wagner, R. D. Howe, Intrinsic embedded sensors for polymeric mechatronics: Flexure and force sensing. *Sensors* **14**, 3861–3870 (2014).

[29] H. A. Wurdemann, S. Sareh, A. Shafti, Y. Noh, A. Faragasso, D. S. Chathuranga, H. Liu, S. Hirai, Embedded electro-conductive yarn for shape sensing of soft robotic

manipulators. in Proceedings of the 2015 Annual International Conference of the IEEE Engineering in Medicine and Biology Society, 25 to 29 August 2015, Milan, Italy, pp. 8026–8029.

[30] J. Maher, "Waveguide optical modulator." U.S. Patent 4,128,299, issued December 5, 1978.

31] Y. Shibata, A. Nishimura, S. Niwa, Y. Osawa, T. Uemiya, "Optical sensors." U.S. Patent 4,750,796, issued June 14, 1988.

[32] S. Begej, Planar and finger-shaped optical tactile sensors for robotic applications. *IEEE J. Robot. Autom.* **4**, 472–484 (1988).

33] G. J. Kookootsedes, H. H. Reese, B. I. Gutek, G. H. Pretzer, "Touch position sensitive optical waveguides." U.S. Patent 4,701,017, issued October 20, 1987.

[34] N. Lagakos, E. U. Schnaus, J. H. Cole, J. Jarzynski, J. A. Bucaro, Optimizing fiber coatings for interferometric acoustic sensors. *IEEE Trans. Microw. Theory Tech.* **30**, 529–535 (1982).

[35] R. A. Lieberman, L. L. Blyler, L. G. Cohen, A distributed fiber optic sensor based on cladding fluorescence. *J. Light. Technol.* **8**, 212–220 (1990).

[36] O. J. A. Schueller, X. Zhao, G. M. Whitesides, S. P. Smith, M. Prentiss, Fabrication of liquid-core waveguides by soft lithography. *Adv. Mater.* **11**, 37–41 (1999).

[37] M. Ramuz, B. C. K. Tee, J. B. H. Tok, Z. Bao, Transparent, optical, pressure-sensitive artificial skin for large-area stretchable electronics. Adv. Mater. **24**, 3223–3227 (2012).

[38] J. Missinne, S. Kalathimekkad, B. Van Hoe, E. Bosman, J. Vanfleteren, G. Van Streenberge. Stretchable optical waveguides. *Opt. Express.* **22**, 4168–4179 (2014).

[39] G. M. Whitesides, S. K. Y. Tang, Fluidic optics. Proc. SPIE 6329, *Optofluidics* (San Diego, CA, 2006), pp. 1-13 (2006).

[40] D. Qin, Y. Xia, G. M. Whitesides, Soft lithography for micro- and nanoscale patterning. *Nat. Protoc.* **5**, 491–502 (2010).

[41] J. A. Jay, An overview of macrobending and microbending of optical fibers. http://www.corning.com/media/worldwide/coc/documents/Fiber/RC-%20White%20Papers/WP-General/WP1212_12-10.pdf (2010).

[42] D. Rus, M. T. Tolley, Design, fabrication and control of soft robots. *Nature* **521**, 467–475 (2015).

[43] H. Zhao, R. Huang, R. F. Shepherd, Curvature control of soft orthosis via low cost solid-state optics. in *Proceedings of the 2016 IEEE International Conference on Robotics and Automation*, 16 to 21 May 2016, Stockholm, Sweden, pp. 4008–4013.

[44] S. J. Lederman, R. L. Klatzky, Hand movements: A window into haptic object recognition. *Cogn. Psychol.* **19**, 342–368 (1987).

[45] L. Skedung, M. Arvidsson, J. Y. Chung, C. M. Stafford, B. Berglund, M. W. Rutland, Feeling small: Exploring the tactile perception limits. *Sci. Rep.* **3**, 2617 (2013).

[46] J. Gafford, F. Doshi-Velez, R. Wood, C. Walsh, Machine learning approaches to environmental disturbance rejection in multi-axis optoelectronic force sensors. *Sensors and Actuators A: Physical.* **248**, 78-87 (2016)

CHAPTER 6

CONCLUSIONS

6.1 Summary

This dissertation reports several advances in fabrication, sensation and control of fluidic elastomer actuators and their application towards hand orthotics and prosthetics. These advances are summarized below:

Fabrication. Rotational casting reported in *Chapter 2* provides an alternative method of fabricating monolithic soft actuators that can withstand high pressures and, therefore, become stiffer than previously reported *pneu-net* actuators. This fabrication method also is a standard method used in the mass production of plastic parts. Rotational casting, followed by an over-molding process reported in *Chapter 3* is an excellent method for incorporating sensors into sot actuators. The mechanical model reported in *Chapter 4* proves that the circumferential constraint is the key factor for FEAs to bend towards the neutral plane, and this model further verified the advantage of fiber-reinforced soft actuators as reported in *Chapter 5*. Both rotational casting and fiber reinforcement method are more efficient in terms of converting the input energy to useful force and generate more robust actuators compared with other fabrication techniques.

Sensation. *Chapter 3* and *4* report an over-molded, etched fiber-optic cable used to sense deflection; *Chapter 5* reports the first use of stretchable optical waveguides for strain sensing. Both kinds of sensors are easy to fabricate, chemically inert,

demonstrate low hysteresis and high precision in their output signals. The stretchable optical waveguides are under continued development as they are composed of chemically similar materials to the soft actuators and can be molded into them, providing higher density sensing networks.

Control. In *Chapter 3*, we used a gain-scheduled PID controller to achieve position control, however, this method suffered from slow responses and difficult manual tuning of parameters. In contrast, the discontinuous controller based on the state machine reported in *Chapter 4* performed accurately, rapidly and with little instability and was easy to implement.

Using a synthesis of our new fabrication techniques, sensors, and control methods, my dissertation reports two prototype devices: (i) a soft orthotic glove (*Chapter 4*) and (ii) a soft prosthetic hand (*Chapter 5*). *(i) The orthotic glove* is purely polymeric, highly compliant, and provides little resistance to natural motion when the actuators are not pressurized. When inflated, the fingers of the glove curve and stiffen augmenting the wearer's grasping force using position control via embedded fiberoptic curvature sensors. *(ii) The prosthetic hand* could not only perform dexterous manipulation, but also achieve various somesthetic functions through simple innervation and control. Using this prosthetic, we conducted various active sensation experiments inspired by the capabilities of a real hand: localizing the position of objects and feeling their stiffnesses. Both of these prototypes are of low cost and relatively high quality and we hope that they will benefit people with disabilities in the future.

The fabrication, sensation and control techniques developed in my dissertation can be expanded into other applications beyond hand prosthetics and orthotics. For example, rotational casting can be used in fabrication high-force, larger-sized exoskeletons for upper limbs and lower limbs. Stretchable waveguide sensors can be incorporated into soft robots targeting at search and rescue or assisting surgery process to increase their accuracy. Finite state machine based controller can adopted as the low-level controller for bio-inspired robots to increase their adaptivity to the environment.

6.2 Future work

There are numerous ways that my work can be expanded and further developed. Human hands have a high density of sensory organelles that can sense not only motions and contacts, but also temperature and pain [1]. Inspired by these abilities, the sensing density of the prosthetic hand will be improved by minimizing the dimensions of the waveguide sensors and adding more sensing parameters, e.g., temperature, pH.

More sophisticated controllers can be designed to consider the inherent compliance and nonlinear properties of FEAs [2]. Machine learning is a powerful tool in data analysis and could be used into the signal coupling of more sensing data [3]. In addition, dynamic models would be helpful in the mechanistic understanding of FEAs and give more design guidance. New fabrication techniques for multi-material [4], multi-stiffness [5], and multi-functional robots will be required for the synthesis of these fundamental advancements into new orthotics and prosthetics that better replicate the natural functions and even add new abilities. Experiments with patients using these prosthetics and orthotics will be required to understand what need to be

addressed and which are superfluous. Wouldn't it be interesting if those without the need for prosthetics became jealous of those using them?

REFERENCE

[1] L. A. Jones, S. J. Lederman, Human Hand Function (Oxford Univ. Press, 2006).

[2] D. Rus, M. T. Tolley, Design, fabrication and control of soft robots. *Nature* **521**, 467–475 (2015).

[3] J. Gafford, F. Doshi-Velez, R. Wood, C. Walsh, Machine learning approaches to environmental disturbance rejection in multi-axis optoelectronic force sensors. *Sensors and Actuators A: Physical.* **248**, 78-87 (2016).

[4] M. R. Cutkosky and S. Kim, Design and fabrication of multi-material structures for bioinspired robots, *Philos. Trans. A. Math. Phys. Eng. Sci.* **367**,1799-1813 (2009).

[5] N. W. Bartlett, M. T. Tolley, J. T. B. Overvelde, J. C. Weaver, B. Mosadegh, K. Bertoldi, G. M. Whitesides, and R. J. Wood, Robot Powered By Combustion, *Science* **349**, 161–165 (2015).